YANPING CHEN

From physics to application of filamentation in air

Thèse présentée
à la Faculté des études supérieures de l'Université Laval
dans le cadre du programme de doctorat en Physique
pour l'obtention du grade de Philosophiæ Doctor (Ph. D)

DÉPARTEMENT DE PHYSIQUE, GÉNIE PHYSIQUE ET D'OPTIQUE
FACULTÉ DES SCIENCES ET DE GÉNIE
UNIVERSITÉ LAVAL
QUÉBEC

2010

J'autorise le Professeur See Leang Chin à utiliser cette thèse en totalité ou en partie.

Résumé

La filamentation dans l'atmosphère est devenue un sujet de recherche des plus attrayants à cause de ses applications possibles à la télédétection de polluants, au contrôle de la foudre, à la génération d'impulsion laser de quelques cycles et à la génération de terahertz à distance. La filamentation d'une impulsion laser femtoseconde intense induit non seulement une transformation significative dans le profil spatio-temporel de l'impulsion laser, mais elle brise en plus la centro-symétrie du milieu de propagation. Le mécanisme physique derrière la filamentation est donc complexe. Plusieurs processus non linéaires intéressants se produisent simultanément au cœur du filament. L'objectif de cette thèse est d'étudier les effets principaux non linéaires qui surviennent pendant la filamentation d'une impulsion laser femtoseconde intense dans l'air. Les impulsions laser utilisées dans ces expériences proviennent d'une chaîne laser Ti : saphir commerciale.

L'évolution complète d'un filament dans l'air est systématiquement étudiée. L'émission de fluorescence du filament, son diamètre et son contenu spectral sont mesurés. Nous montrons qu'un filament peut être vu comme une colonne « auto-guidée » avec deux sections d'ionisation: une première où l'ionisation est efficace suivie par une seconde, faiblement ionisée. Le diamètre du cœur du filament demeure quant à lui presque constant. L' « auto-conversion » vers les basses fréquences est observée en fonction de la longueur du filament et elle est causée par la réponse Raman moléculaire.

Il est aussi démontré que l'intensité élevée au cœur du filament dans l'air induit une forte biréfringence instantanée due à la modulation de phase croisée d'origine électronique et une forte biréfringence retardée due à la réponse Raman. Cette dernière mène à la génération d'un séparateur de polarisation gazeux ultrarapide sans seuil de dommage ni limitation spectrale.

De plus, on observe expérimentalement que l'émission terahertz provenant soit d'un filament à une couleur dans l'air, soit d'un filament à deux couleurs, a une polarisation

elliptique. Ceci est attribué au bris de la symétrie de l'air dans le filament. Finalement, nous étudions la polarisation de la radiation terahertz provenant d'un filament soumis à un champ électrique DC. On montre qu'une nouvelle source de terahertz, différente de l'émission terahertz provenant d'un filament à une couleur sans champ externe, est générée en appliquant un champ électrique externe. La polarisation linéaire de cette source de terahertz est parallèle au champ DC.

Abstract

Filamentation in the atmosphere has become one of the most attractive research topics due to its promising potential applications, such as remote atmospheric pollutants detection, lightning control, few-cycle laser pulse generation and remote terahertz generation, etc. The filamentation process of an intense femtosecond laser pulse not only induces significant transformations in the spatio-temporal profile of the laser pulse but also breaks the centro-symmetry of the propagation medium. Thus, the physical mechanism of the filamentation process is quite complex. Many interesting nonlinear processes take place simultaneously inside the filament core. The aim of this thesis is to investigate key nonlinear processes occurring during the filamentation of intense femtosecond laser pulses in air. The laser pulses used in the experiments are delivered by a commercial Ti-Sapphire femtosecond laser system.

A full evolution of a femtosecond laser filament in air is systematically investigated, including the emitted fluorescence signal, the diameter of the filament core and the spectrum of the filament. It is found that a filament could be regarded as a self-guided column with two ionizing sections: one with efficient ionization followed by the other weakly ionized. The diameter of the filament core stays almost constant, and continuous self-frequency down shift in the spectrum is observed as a function of the filament length, which is due to molecular Raman response.

It is also demonstrated that the high intensity within the core of an air-filament induced an instantaneous strong birefringence thanks to electronic cross phase modulation and a delayed strong birefringence due to rotational Raman response, the latter leading to the generation of an ultrafast gaseous polarization separator that is free from damage threshold and spectral bandwidth limitation.

Moreover, it is experimentally observed that terahertz emission from either a one-color air-filament or a two-color air-filament is elliptically polarized due to symmetry-breaking of air in the filament zone. Finally, we investigated the polarization

of the terahertz radiation from a DC-biased filament. It is demonstrated that a new terahertz source, apart from the terahertz emission from a one-color filament without DC-bias, is generated by applying a DC bias to a one-color filament. The linear polarization of this terahertz source is parallel to the DC field.

Résumé court

Dans cette thèse, nous présentons quelques effets non linéaires qui surviennent lors de la filamentation d'une impulsion laser intense dans l'air. Nous montrons expérimentalement l'évolution complète d'un filament unique, l'auto-conversion vers les basses fréquences dans un filament dans l'air, la biréfringence induite par un filament dans l'air et les caractéristiques de l'émission terahertz d'un filament à une couleur, à deux couleurs où avec un champ électrique externe appliqué.

Acknowledgements

The work presented in this thesis is realized in the ultra-short intense laser laboratory led by Prof. Chin in Laval University. I appreciate very much that Prof. Chin has provided me the great opportunity to join this group, which is always working at the forefront of the field in laser science. He has taught me so much about the physics and led me to an exciting scientific world. I want to express to him my sincere thankfulness for his direction, his encouragement and his support during my study as a Ph. D student. His insight and his passion for Science will be a model for me throughout my career.

I would like to gratefully acknowledge my co-director, Dr. Francis Théberge, who gave me lots of training in the laboratory. I appreciate very much the time during which I had opportunity to work together with him. Through him, I made my first step on the field of laser filamentation.

I would like to express my deep gratitude to Mr. Mario Martin for his technical support in the lab. His kind assistance helped me a lot in performing the experiments. I would next thank Mr. Claude Marceau for many kind helps during the experiments, especially in computer programming. I would also thank Dr. Tiejun Wang, Dr. Zhendong Sun and Dr. Weiwei Liu for their suggestions and fruitful discussions. It is my greatest pleasure to get to know them and work with them closely. I express my sincere gratitude to all the staffs in the physics department and COPL. I would like to acknowledge those whom I have been fortunate to know and work in proximity with in the laboratory.

Moreover, during my study I have received generous helps from Dr. Olga Kosareva, Prof. Valerii P. Kandidov and Dr. Neset Aközbek. They are excellent scientists in computation physics. The collaboration with them helps me get insight into many interesting physical phenomena.

Finally, I gratefully appreciate the financial support I received from Prof. Chin.

To my parents

Table of Contents

List of Figures

Chapter 1: Introduction

1.1 The beginning of filamentation nonlinear optics

Filamentation was first observed with a Q-switched laser beam focused into a solid by Hercher in 1964 [1]. Due to technical limitations when producing high peak power laser system, the filamentation in atmosphere was not obtained until the development of the chirped pulse amplification (CPA) technique that permitted the generation of femtosecond laser pulses with peak power higher than GW [2]. In 1995, Braun *et al.* observed self-channeling of a GW laser in air for more than 20 m [3]. The laser beam remained focused over several meters along the propagation axis. This type of propagation was called filamentation. Here, the term "filamentation" denotes an extended light string whereas the beam contracts and maintains a narrow diameter in the transverse diffraction plane over extended distances much longer than the Rayleigh length without the help of any external guiding mechanism. This propagation regime was identified as a balance between Kerr self-focusing effect and laser-induced plasma defocusing effect. The onset of the filamentation process can be manipulated by controlling the initial beam diameter and pulse duration [4, 5].

In the filamentation process, several effects (Kerr-induced self-phase modulation [6], plasma defocusing [5, 7] and group velocity dispersion) compete in a rich dynamics of many nonlinear processes. During the propagation, the laser pulse reorganizes itself in space and in time and splits into several sharp peaks [8-10]. One of the important consequences of the self-transformation of the laser pulse through filamentation is the generation of few-cycle pulses with high quality beam profile ($M^2 < 1.07$) [11-13]. Besides, strong spectral broadening (supercontinuum) is generated (more details in chapter 2) which covers the entire visible part of the spectrum when propagating in air [5]. A nice application of the unique properties of the filament is illustrated by the possibility of designing optical parametric amplifiers where a filament acts as a pump source. Théberge *et al.* have shown that a few-cycle signal beam tunable over the entire

visible spectrum is obtained with a self-improved beam quality [14]. It was found that the transverse pattern of the signal beam was circularly symmetrical around the propagation axis, while the initial beam profile was distorted. It is very close to a diffraction-limited Gaussian beam ($M^2 < 1.01$). This self-improvement of the beam quality translates the self-spatial mode filtering of a filament [15-17]. When compared to an OPA output operating with the same laser as a pump (but not in a filament form), the signal beam from the filament features a shorter pulse duration. This interprets the self-compression effect of a filament [10, 11, 18]. Energy fluctuations of the generated signal beam were also stabilized [14] during the nonlinear propagation, translating the intensity clamping effect inside a filament [5]. Such nice self-actions were also reported in the case of conical emission [15, 19]. These improvements of the laser pulses are contrary to the normal wisdom that any non-resonant, nonlinear interaction will result in a large fluctuation of the signal as compared to linear interaction. We call these new phenomena 'filamentation nonlinear optics' [16].

Filamentation nonlinear processes are nonlinear interactions within the filament core, essentially isolated from the inhomogeneous background reservoir [16]. The filament core has two important advantages. One is its stable intensity due to intensity clamping through the interplay between Kerr self-focusing and plasma induced defocusing [20], and another is the self-improvement of the beam spatial profile through self-spatial mode filtering [15-17]. Therefore, any nonlinear process sampling only the filament core features high conversion efficiency (owing to high intensity inside the filament core), high stability (due to intensity clamping inside the filament core) and high spatial quality (thanks to self-spatial mode filtering of the pulse during filamentation) [14, 16]. Several interesting experimental observations on nonlinear interaction during filamentation in air, such as self-phase modulation (continuum generation) [15], few-cycle pulse generation through four-wave mixing [14, 21], third-harmonic generation [22, 23] and singe-cycle terahertz pulses generation [24, 25], have already been reported in the past several years.

Recently, it was demonstrated that a laser filament can polarize the propagating gas medium (both atomic gases and molecular gases) and break its symmetry [26-28]. Thus, the dynamics of many nonlinear interactions involved in the filamentation processes become more and more complex. This interesting observation will surely open a new page in filamentation nonlinear optics.

1.2 Potential applications

Self-phase modulation and self-steepening during filamentation process leads to a supercontinuum spanning from the UV (250 nm) [23, 29-33] to the IR (experimental observation of a broadening up to 13 μm) [5, 34, 35]. Due to its coherent property, this supercontinuum could be used for optical pulse compression to produce shorter and shorter pulses in gases (typically in Argon or Neon) down to the single cycle regime (2.66 fs at 800 nm) [11, 12, 21, 36-44]. Besides, through optical parametric amplifications with the filament as a pump, it is possible to obtain a tunable few-cycle signal pulse covering a very wide spectrum with very nice beam quality and high energy stability [14, 45]. Moreover, the applications for the detection and identification of pollutants present in the atmosphere using a LIDAR (LIght Detection And Ranging) have sparked great interest [46-49].

Self-guided filaments can induce substantial birefringence in gases. In atomic gases such as argon, due to the electronic cross-Kerr process, a filament can work as a half-wave plate for a co-propagating beam by controlling the gas pressure [26]. This allows the realization of a Kerr-gate with ultrafast switching time which is limited by the pulse duration of the filamenting beam. In molecular gases such as nitrogen and oxygen, apart from the electronic effect, delayed modification in refractive indices is obtained, which is contributed by laser induced rotational molecular wave packet [27, 28]. The molecules can be partially aligned in the presence of the filament. As a consequence, there is a positive change in the refractive index along the molecule's aligned direction and a negative change along its orthogonal direction. Thus, for a co-propagating probe, one probe component is guided inside the filament zone due to

the focusing effect of the positive change in the index of refraction while its orthogonal component is diffracted out due to defocusing effect. Therefore, a filament can work as a gaseous polarization separator which is free from damage threshold and spectral bandwidth limitation.

The onset of a filament can be manipulated by the beam diameter and pulse duration of an initial pulse [4, 5]. Therefore, a filament can be used as a carrier for other light sources which are not suitable for long-distance propagation in the atmosphere. For instance, long-range propagation of terahertz (THz) wave in air is highly limited by the strong absorption of THz by water vapor in air. THz radiation from a filament seems to be one solution to this propagation problem since the THz pulses can be generated close to the remote target by the filament [24, 25, 50, 51].

1.3 About this thesis

When femtosecond laser pulses propagate in air, they collapse into a filament which features a clamped intensity and a constant diameter over a propagation distance much longer than the Rayleigh range. All these interesting features are expected to play an important role in nonlinear processes inside the filament. Aiming to contribute to the understanding of the nonlinear processes during filamentation, this thesis identifies the characteristics of some nonlinear processes involved during the nonlinear propagation of femtosecond laser pulses in air. The thesis is organized as follows:

Chapter 2 (Physics of filamentation) outlines the physics of filamentation based on a moving focus model.

Chapter 3 (Laser chain) illustrates the laser system used for the experiments presented in this thesis.

Chapter 4 (Evolution of a single filament in air) characterizes the full evolution of a single filament by measuring the diameter of the filament core and the fluorescence signal from the side of the filament.

Chapter 5 (Filamentation-induced continuous self-frequency down shift in air) demonstrates continuous self-frequency down shift inside the filament zone during the propagation of a femtosecond laser pulse in air.

Chapter 6 (Polarization separator created by a filament in air) demonstrates that a femtosecond laser filament acts as a polarization separator for a co-propagating probe pulse in molecular gases.

Chapter 7 (THz emission from one-color filament) presents that elliptically polarized THz emission is observed from a single filament.

Chapter 8 (THz emission from two-color filament) diagnoses the polarization characteristics of THz emission from a two-color femtosecond laser filament when the polarizations of ω and 2ω beams are orthogonal.

Chapter 9 (THz emission from DC-biased filament) demonstrates that the THz emission from a DC-biased filament can be regarded as a sum of an elliptically polarized THz source (generated by a filament without external electric field) and a linearly polarized THz source induced by the external electric field applied to the filament.

Chapter 10 (Conclusion)

Chapter 2: Physics of filamentation

2.1 Kerr self-focusing of a CW beam

The phenomenon of Kerr self-focusing was observed in 1960s [1, 52]. The refractive index of air n in the presence of an intense laser beam does not only depend on its frequency, but also on the spatial distribution of the laser intensity $I(r)$ according to the relation:

$$n = n_0 + \Delta n_{kr} = n_0 + n_2 I(r), \tag{2-1}$$

where n_0 is the linear index of refraction; n_2, termed as the coefficient of the Kerr nonlinear index of refraction, relates to third-order nonlinear susceptibility $\chi^{(3)}$ by [5]

$$\chi^{(3)} = 4\varepsilon_0 c n_2 n_0^2/3. \tag{2-2}$$

In Eq. (2-2), ε_0 is the permittivity of vacuum and c is the velocity of light in vacuum. In most optical medium, the coefficient n_2 is positive. If we consider a laser beam with a transverse Gaussian distribution in intensity propagating in an optical medium, the resulting index of refraction at the center of the laser beam is higher than that at the outer zone. Thus, the velocity at the center of the beam is lowest, and it increases radially from the center to the outer edges. As a result, a curvature of the wavefront is induced, which is similar to that of a lens [5, 53]. Thus, this type of phenomenon is called self-focusing. In principle, the laser beam starts to self-focus provided that (1) there is a non-uniform transverse spatial distribution in intensity of the laser beam across the wavefront and (2) the power of the laser beam is higher than the critical power P_{cr} for self-focusing, which is suggested by numerical simulations beyond the paraxial approximation as [54]

$$P_{\mathrm{cr}} = \frac{3.77\lambda^2}{8\pi n_0 n_2}, \tag{2-3}$$

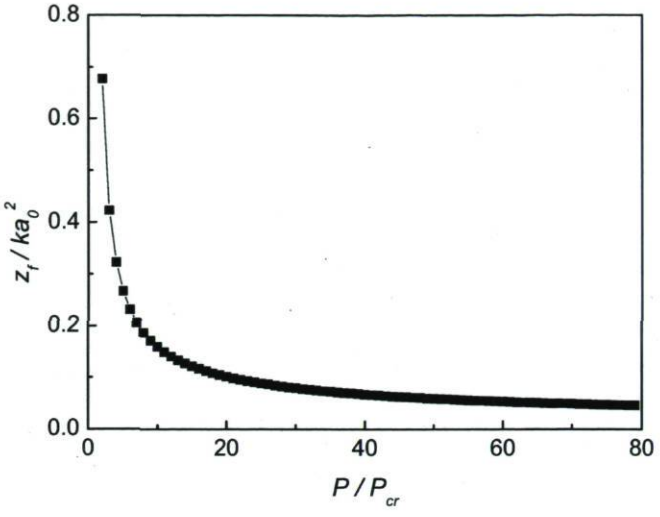

Figure 2-1: Self-focusing distance as a function of the initial power of the laser pulse according to Eq. (2-4).

where λ is the central wavelength of the laser beam. The critical power is around a few GWs for the gas media. When the initial power of the laser beam is lower than the critical power P_{cr}, linear diffraction of the laser beam dominates the propagation process. Thus, the intensity of the laser beam quickly decreases and becomes negligible. When the initial power of the laser beam equals to the critical P_{cr}, the linear diffraction of the laser beam is balanced by the self-focusing effect. When the initial power of the laser beam is higher than the critical power P_{cr}, the laser self-focusing effect overcomes the laser linear diffraction effect, i.e., the laser beam collapses. The focusing effect will get stronger and stronger during the propagation if there is no saturation mechanism. The self-focusing distance is determined by [54]:

$$z_f = \frac{0.367ka_0^2}{\left\{\left[\left(\frac{P_{in}}{P_c}\right)^{1/2} - 0.852\right]^2 - 0.0219\right\}^{1/2}}, \tag{2-4}$$

where a_0 is the beam radius defined at $1/e$ level of intensity, P_{in} is the initial power of the laser beam and k is wave number of the laser beam. According to Eq. (2-4), Fig. 2-1 shows the energy dependence of the self-focusing distance z_f as a function of the initial power of the laser beam. The self-focusing distance decreases by one order of magnitude with the increase in the initial power of the laser beam from $P = 1.1\ P_{cr}$ to $P = 50\ P_{cr}$.

In many experiments, an external lens is often used to force the beam to self-focus earlier due to the limited length of the propagation medium. The new self-focusing distance z_f' is predicted by the lens transformation equation:

$$\frac{1}{z_f'} = \frac{1}{z_f} + \frac{1}{f}, \tag{2-5}$$

where f is the geometrical focal length of the external lens.

2.2 Moving focus model

In the case of a pulsed laser, the steady-state regime discussed in the last section is not sufficient to explain the features. The self-focusing process of a laser pulse can be interpreted by the moving focus model [19, 55, 56], in which the laser pulse is considered as a stack of successive thin slices in time (or in space along the propagation axis) that are independent from each other. Each slice contains a specific power and its thickness is at least $c\tau$ (τ is an optical cycle of the electromagnetic wave) [57]. This is because the intensity of an electromagnetic wave is represented by the Poynting vector averaged over at least one optical cycle. All the slices inside the pulse envelope with peak power higher than the critical power P_{cr} self-focus at distances predicted by Eq. (2-4), as shown in Fig. 2-2. Thus, a series of self-foci, coming from the self-focusing of different slices of the pulse (with peak power above the critical power P_{cr}), is produced on the propagation axis. This constitutes what we call a filament. The slices with peak power below the critical power P_{cr} diffract out linearly.

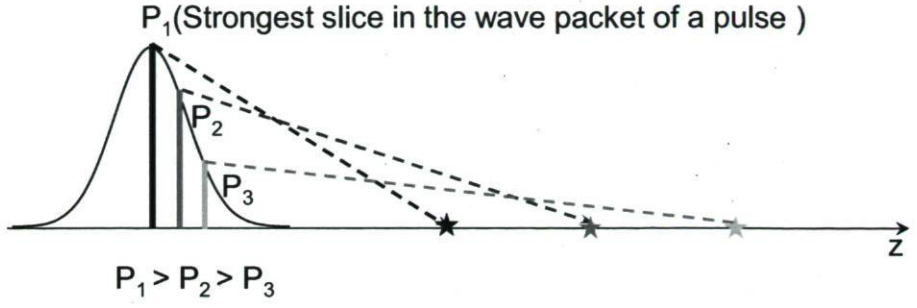

Figure 2-2: Moving focus model: the central slice (P_1) has highest peak power, so it will self-focus at a shortest distance; the slices with weaker peak power (P_2 and P_3) self-focus at a further distance.

Figure 2-3 shows a more detailed dynamic picture of the moving focus model [5]. Slice t_A and slice t_D in Fig. 2-3 are defined for the slices possessing a peak power P_{cr} on the ascending and descending slope of the pulse envelope, respectively. Fig. 2-3(a) presents the predicted locations of the moving focus as a function of time in the laboratory coordinate by applying $P_{in} = P(\tau = t - z/\upsilon_g)$ to Eq. (2-4) for obtaining self-focusing distance for each slice in the pulse. The first slice reaching its self-focus is slice t_B which is at the ascending slope of the pulse envelope (or at the front of the laser pulse). The corresponding self-focus locates at point B in Fig. 2-3(a). The central slice, slice t_C, is the most powerful one of the pulse envelope. Thus, it self-focuses at the shortest distance [point C in Fig. 2-3(a)]. As a consequence, the self-focus moves backwards in time [point B → point C in Fig. 2-3(a)]. Thus two branches appear after the point B: the upper branch moving forward towards point A describes the forward motion of the focus responsible for the slices at the front part of the pulse where $t_A < t \le t_B$; the lower branch BCD describes the backward motion of the focus from point B to point C ($t_B < t \le t_C$), followed by the forward motion of the focus from point

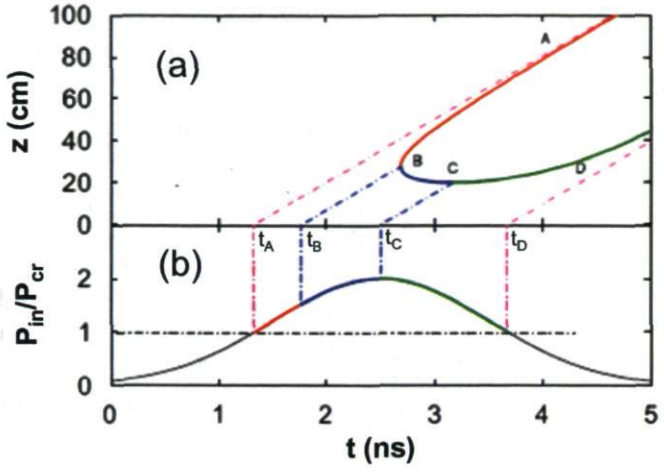

Figure 2-3: (a) Moving focus location as a function of time and (b) input pulse power. The slice with maximum peak power collapses at the shortest distance from the laser pulse. The slices with lower peak power self-focus at a farther distance on the propagation axis.

C to point D corresponding to the slices in the trailing part of the pulse ($t_C < t \le t_D$).

2.3 Intensity clamping

Now we know when an intense laser pulse propagates in air, it will self-focus at a certain distance following the moving focus model. During this process, the intensity of this laser pulse becomes higher and higher. As a result, it induces a weak plasma on the propagation axis through tunnel/multiphoton ionization (TI/MPI) of the air molecules [5, 53], as Fig. 2-4.

The ionization potential U_{ip} is 12.063 eV for oxygen and 15.576 eV for nitrogen [58]. In the case of an 800 nm laser beam, the energy of the laser photons ($\hbar\omega_0 = 1.5\ eV$) is far lower than the ionization potential U_{ip} in both oxygen and nitrogen. For instance,

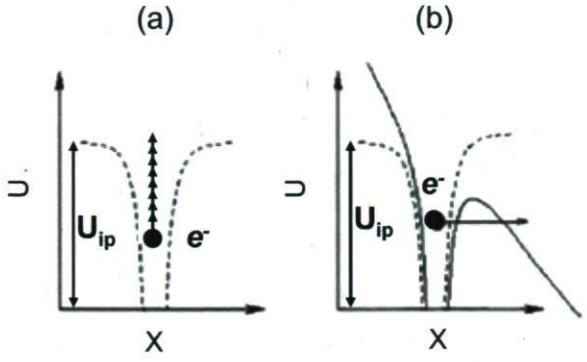

Figure 2-4: Schematics of (a) multiphoton ionization and (b) tunnel ionization.

ionization of oxygen requires the simultaneous absorption of 8 photons. This process is possible at a very high laser intensity, i.e., at the collapse of the laser beam where the pulse intensity increases significantly.

The emergence of the plasma results in a change in the index of refraction on the propagation axis in air by [53]

$$n_0 + \Delta n_p = \left[1 - \frac{\omega_p^2}{\omega_0^2}\right]^{1/2} \cong 1 - \frac{\omega_p^2}{2\omega_0^2}, \tag{2-6}$$

where the subscript p denotes plasma, ω_0 is the central frequency of the laser pulse and ω_p is the plasma frequency ($\omega_p \cong \sqrt{\frac{4\pi e^2}{m_e} N_e}$ where N_e is the electron density, e and m_e are the charge and mass of the electron in cgs units, respectively). In air, $n_0 \cong 1$. The electron density in a filament in air generated by a 50 fs / 800 nm laser pulse has been measured to be around 10^{16} cm^{-3} [59]. This gives $\upsilon_p = \omega_p / 2\pi \cong 9 \times 10^{11} Hz$ which is much smaller than the optical frequency (~10^{14} Hz), i.e., $\omega_p << \omega_0$. Hence [53]

$$\Delta n_p \cong -\frac{\omega_p^2}{2\omega_0^2} = -\frac{4\pi e^2 N_e(t)}{2m_e\omega_0^2}. \tag{2-7}$$

Therefore, in the presence of the plasma, the total index of refraction on the propagation axis is contributed by two nonlinear components:

$$n = n_0 + \Delta n_{kr} + \Delta n_p. \tag{2-8}$$

Introduce Eq. (2-1) and Eq. (2-7) into Eq. (2-8), the total index of refraction can be noted as:

$$n = n_0 + n_2 I - \frac{4\pi e^2 N_e(t)}{2m_e\omega_0^2}. \tag{2-9}$$

The effect of the plasma saturates self-focusing locally. The shrinking of the laser beam stops when

$$n_2 I = \frac{4\pi e^2 N_e(t)}{2m_e\omega_0^2}. \tag{2-10}$$

In this case, the Kerr self-focusing effect balances the plasma induced defocusing effect. This balance leads to a confined minimum beam diameter and a limited peak intensity at the self-focal zone. This phenomenon now is known as intensity clamping [60, 61]. In air, an intensity of 4×10^{13} W/cm^2 was obtained by using the Eq. (2-10) for a laser pulse with 100 fs pulse duration [60].

2.4 Spectral broadening and conical emission

Filamentation process is always accompanied by a strong spectral broadening which is contributed by self-phase modulation and the ionization of the propagation medium [5, 53]. Figure 2-5 shows a typical transverse pattern of a Ti-sapphire filamenting laser pulse.

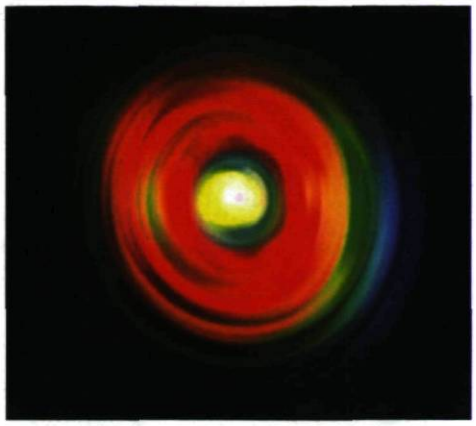

Figure 2-5: Beam pattern of a 7 mJ, 800 nm, 45 fs free propagating laser beam at far field (after filamentation).

During filamentation, the temporal shape of the laser pulse is strongly reorganized [5, 53]. The temporal variation of the laser intensity induces a temporal variation in the index of refraction as

$$n = n_0 + n_2 I(t). \tag{2-11}$$

This in turn involves the appearance of new frequencies in the laser spectrum by modulation of the phase of the wave. The frequency shift can be noted as [62]

$$\begin{aligned} \Delta\omega &= \frac{\partial \phi_{NL}}{\partial t} \\ &= \frac{\partial}{\partial t}\left(-\frac{\omega_0 \Delta n(t)}{c} z\right) \\ &= -\frac{\omega_0 z}{c}\frac{\partial[\Delta n(t)]}{\partial t}. \end{aligned} \tag{2-12}$$

This effect is termed as self-phase modulation (SPM). The generated new frequencies depend on the slope of the pulse, the propagation distance z in the Kerr medium and its nonlinear index coefficient n_2.

The front part of the laser pulse always sees a neutral gas, i. e., no contribution from plasma. By introducing Eq. (2-1) into Eq. (2-12), the frequency shift in the front part of the pulse can be noted as [7]

$$\Delta\omega = -\frac{\omega_0 z}{c} n_2 \frac{\partial I(front\ part)}{\partial t}. \tag{2-13}$$

Thus the self-phase modulation at the front part of the laser pulse generates redder frequencies because the front part of the pulse has a positive temporal slope, i. e., $\frac{\partial I(front\ part)}{\partial t} > 0$.

The back part of the laser pulse will see both the neutral gas and the laser induced plasma since the medium is only partially ionized. So the nonlinear refractive index consists of two factors: Kerr effect and the laser induced plasma effect. By introducing Eq. (2-1), Eq. (2-6) and Eq. (2-7) into Eq. (2-12), the frequency shift in the back part of the pulse can be noted as [7]

$$\Delta\omega = -\frac{\omega_0 z}{c} n_2 \frac{\partial I(back\ part)}{\partial t} + \frac{2\pi z e^2}{c m_e \omega_0} \frac{\partial N_e}{\partial t}. \tag{2-14}$$

Generally, the free electron generation through MPI/TI could be approximated by [61]:

$$N_e \cong N_0 w \int_{-\infty}^{t} I^m(t) dt, \tag{2-15}$$

where N_0 is the density of the neutral air, w is the effective empirical tunnel ionization rate of nitrogen (and oxygen), I^m is the empirical power law of the ionization and m is the empirical slope of the experimental ion yield versus intensity curve in the log-log scale [63]. Substituting Eq. (2-15) into Eq. (2-14), one obtains [7]

$$\Delta\omega = -\frac{\omega_0 z}{c} n_2 \frac{\partial I(back\ part)}{\partial t} + \frac{2\pi z e^2 N_0 w}{c m_e \omega_0} I^m(t). \tag{2-16}$$

The first term in Eq. (2-16) gives the self-phase modulation induced frequency shift in the neutral, which indicates the generation of bluer frequencies due to the negative temporal slope at the back part of the laser pulse, i. e., $\frac{\partial I(back\ part)}{\partial t} < 0$. In the real case, the presence of the plasma generated by the front part of the laser pulse will reshape the temporal profile in the back part of the laser pulse [5, 53]. So the intensity distribution at the back part of the pulse becomes very steep, which gives rise to a large blue shift of the frequency. The second term corresponds to the plasma contribution which also predicts a positive blue shift. Thus, self-phase modulation at the back part of the laser pulse provides large broadening towards the blue side of the pump frequency.

The rainbow-like conical emission in Fig. 2-5 is due to self-phase modulation in the radial direction of the laser pulse [53]. The discussion on spectral broadening above is based on the assumption that the laser pulse has a plane wave. So we only considered the wave vector k_z which is along the propagation axis z. For a laser pulse with a curved wave front, the general wave vector $\vec{k}$ contains a transverse part of the wave vector k_r as well [7]:

$$\vec{k} = k_z\vec{z} + k_r\vec{r} = k_{z0}\vec{z} + \Delta k_z\vec{z} + k_{r0}\vec{r} + \Delta k_r\vec{r}, \tag{2-17}$$

where $\vec{z}$ and $\vec{r}$ are unit vectors parallel and orthogonal to the propagation direction z; k_{z0} and k_{r0} are the initial wave vectors along $\vec{z}$ and $\vec{r}$, respectively. In the $\vec{r}$ direction, the electron density gradient will give rise to the blue shift of the laser spectrum by [64]

$$\Delta k_r = \left|\frac{\partial \phi_{NL}}{\partial r}\right| \sim \left|\frac{\partial N_e}{\partial r}\right|. \tag{2-18}$$

This radial electron density gradient varies continuously from zero to a maximum. The divergence of the general wave vector $\vec{k}$ will be larger when the electron density gradient is larger. Also, the larger the frequency shift is, the larger the divergence will be.

2.5 Self-spatial mode filtering

In any experimental cases, the transverse intensity and fluence distribution of a real laser pulse will never be perfect even though great efforts are made to favor the production of a fundamental mode. Essentially, any real pulse we are using nowadays is the superposition of a fundamental mode (with higher peak power and intensity) and other high order spatial modes (with much lower peak power and intensity). Since the peak intensity of the fundamental mode is higher than those of the other spatial modes, the fundamental mode will self-focus towards the propagation axis first and produces a fundamental mode profile at the self-focal zone; i.e. the filament core has high quality beam profile. Also, it will reach the clamped intensity earlier. This high intensity is high enough to tunnel/multiphoton ionize the air molecules and create a weak plasma at the self-focal zone. However the filament core will preserve the beam high quality because of the low plasma density (about 10^{16} cm^{-3} [65, 66]), three orders of magnitude lower than the density of air. In fact, there is very little energy consumption for ionization [56] and the resulting homogeneous electron distribution would not disrupt the homogeneous intensity and fluence distribution of the fundamental mode at the self-focal zone. At the position where intensity clamping of the fundamental mode occurs, the higher order modes have diameters much larger than that of the fundamental mode and their self-focusing would be interrupted by plasma defocusing induced by the fundamental mode. Therefore, the intensity of the high order modes would be much lower. They would constitute part of the background reservoir and would not destroy the high quality of the filament core. Figure 2-6 shows the numerically simulated normalized intensity distribution across the diameter of an assumed CW beam propagating in air at two distances [16, 17]. The model used to describe the propagation is based on the

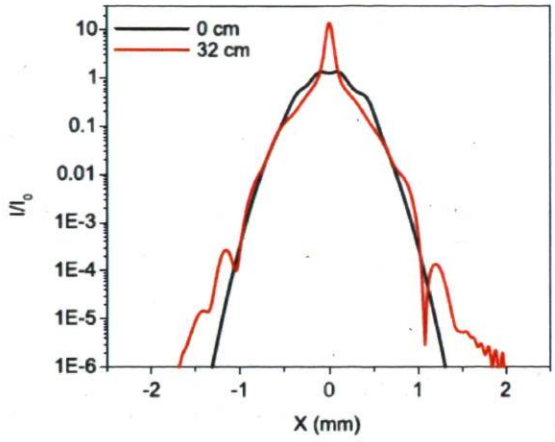

Figure 2-6: Simulated intensity distribution of an initially distorted pulse profile at two propagation distances in air. The initial laser beam is Gaussian and has a diameter of 1 mm at $1/e^2$ level. Its power is three times the critical power for self-focusing.

two-dimensional (2D) nonlinear Schrödinger equation (NLSE), which is written as [16, 17]:

$$2ik_0\frac{\partial A}{\partial z}+(\frac{\partial^2}{\partial x^2}+\frac{\partial^2}{\partial y^2})A+2k_0^2\Delta nA=0\,, \tag{2-19}$$

where A represents the amplitude of the light field, k_0 denotes the wave number of the beam whose central wavelength is 800 nm. Δn corresponds to the intensity dependent refractive index which includes the optical Kerr effect induced nonlinear refractive index [Eq. (2-1)]. Ten randomly distributed perturbations, with 200 μm in diameter and peak intensity of 10% of the initial local intensity, are introduced (black line in Fig. 2-6). After propagation of 32 cm, the intensity distribution reveals a very smooth center (filament core) and a several orders of magnitude lower pedestal (diverged high order modes), as red line in Fig. 2-6.

In the filamentation process, only the fundamental mode of the pulse will self-focus to a smaller diameter than all the other high order modes and contribute to the high quality filament core, similar to the linear geometrical focusing of a laser beam with high order modes. But it is not possible to filter out the fundamental mode by using a pinhole at the focal point as in the case of linear geometrical focusing. Each self-focus in the filament comes from the self-focusing of a slice of the laser pulse. A pinhole placed at the focal position will block further propagation of the background reservoir, stopping further self-focusing [67]. Therefore, the only way to "filter out" the fundamental mode in the case of self-focusing of an intense laser pulse is to sample the filament core through a nonlinear process [14].

Chapter 3: Laser chain

The laser facility in our lab is a commercial Ti:sapphire laser system (Spectra Physics) based on chirped pulse amplification (CPA) technique. The CPA technique, invented by Gérard Mourou and Donna Strickland in 1980s [2], can amplify an ultrashort laser pulse by spectrally chirping the laser pulse which means temporally lengthening the laser pulse. Our laser system can simultaneously emit three intense femtosecond laser beams.

Layout

The schematic layout of the laser system is presented in Fig. 3-1. The system consists of a mode-locked Ti-sapphire oscillator (Tsunami, 40 fs at 74 MHz, 400 mW) which is pumped by a 532 nm laser (Millenia, continuous-wave, 4.2 W), followed by a stretcher and a regenerative amplifier which is pumped by a fraction (8 W) of output from a 527nm laser (Evolution 30, ~150 ns at 1 kHz, 16 W) and works at 1 kHz repetition rate.

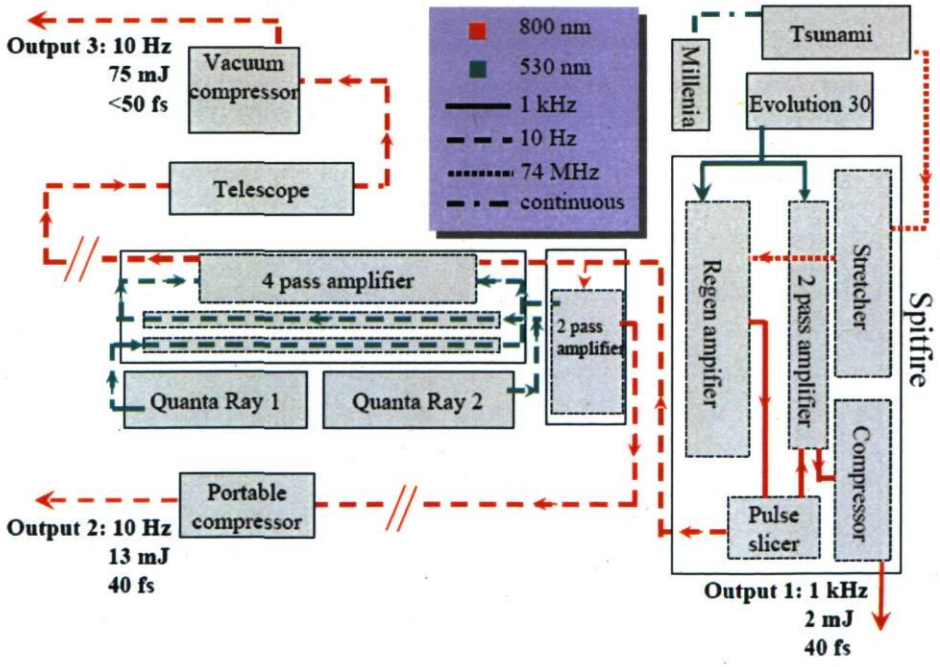

Figure 3-1: Schematic layout of the laser chain.

A two-pass amplifier pumped by the remaining energy from Evolution 30 enhances the output from the regenerative amplifier. The amplified beam is compressed to 40 fs and gives a maximum energy of 2 mJ/pulse at 1 kHz (Output 1). In the meanwhile, a pulse slicer after the regenerative amplifier picks up one pulse every 100 ms. This 10 Hz laser beam is evenly split into two beams which serve as the seed beams for a 10 Hz two-pass amplifier and a four-pass amplifier, respectively. A 532 nm laser (Quanta-Ray 1, 15 ns at 10 Hz, 1200 mJ/pulse) is split into 2 beams. One beam (500 mJ/pulse) is used as pump for the 10 Hz two-pass amplifier. The other beam (700 mJ/pulse), together with another 532 nm laser (Quanta-Ray 2, 15 ns at 10 Hz, 910 mJ/pulse), pumps the four-pass amplifier. The output pulses from the 10 Hz two-pass amplifier are compressed to 40 fs by a portable compressor, with energy of 13 mJ/pulse (Output 2). The output beam from the four-pass amplifier, after compression by a vacuum compressor, has a maximum energy of 75 mJ/pulse with pulse duration of 50 fs (Output 3). The typical spectrum of all three beams is centered around 800 nm with a spectral width of 32 nm (FWHM: full width at half maximum).

Spitfire (Spectra Physics)

The spitfire is a typical Ti:sapphire-based chirped-pulse amplifier which is composed by a Faraday isolator, a grating-based stretcher, a regenerative amplifier (regen), a two-pass amplifier and a grating-based compressor, as shown in Fig. 3-1. Before the invention of the CPA technique, the peak power of laser pulses was limited because laser pulses with high intensities damage the gain medium and the laser components inside the amplifier through Kerr self-focusing effect.

In the Spitfire, the seed from the oscillator first passes through the Faraday isolator to prevent back-reflected light from the amplifier system to return into the oscillator. Prior to introducing the seed into the regenerative amplifier, it is stretched out to about 200 ps (positively chirped) in time through chromatic dispersion by the grating in the stretcher.

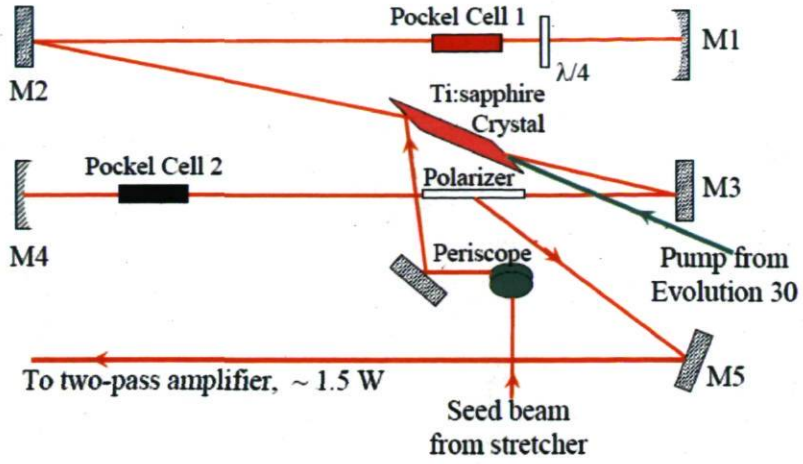

Figure 3-2: Schematics of the regenerative amplifier.

The regenerative amplifier is the core of the Spitfire, as detailed in Fig. 3-2. One of the stretched seed pulses is trapped inside the regen cavity by activating Pockel cell 1 (PC1) which works as a quarter waveplate after activation and changes the polarization of the seed from vertical to horizontal. This seed pulse is amplified each time when it passes through the gain medium (Ti:sapphire). After travelling about 16 round trips inside the regen cavity, the seed pulse reaches its maximum energy due to gain saturation of the Ti:sapphire crystal. The amplified seed pulse is extracted by activating Pockel Cell 2 (PC2) which works as a quarter waveplate and changes the polarization of the seed from horizontal to vertical. This vertically polarized seed is reflected out of the regen cavity by the polarizer. The power of this output beam is ~1.5 W. Then this extracted pulse is further amplified by a two-pass amplifier. After being compressed by the grating-based compressor, the pulse reaches a maximum energy of 2 mJ with pulse duration of 40 fs. This output has a repetition rate of 1 kHz.

10 Hz high power amplifiers

To achieve high pulse energy, 10 Hz high power amplifiers were built, as shown in Fig. 3-1. A pulse slicer is used just after the regenerative amplifier for extraction of a 10 Hz

seed beam. Half of the seed is sent to a 10 Hz two-pass high power amplifier which amplifies this seed and delivers 13 mJ/pulse after compression. Another half of the seed works as the seed pulse for the 10 Hz four-pass high power amplifier which delivers the energy as high as 75 mJ/pulse after the vacuum compressor.

In these two high power amplifiers, the output energy is controlled by changing the energy of the input seed, realized by a combination of a half waveplate and a polarizer mounted in the input pathway of the seed.

Chapter 4: Evolution of a single filament in air*

4.1 Introduction

Filamentation has sparked considerable interest owing to its novel properties such as intensity clamping [68], self-spatial filtering [14, 16], self-stabilization [14, 16, 33] and self-steepening [8]. Efficient third harmonic generation and four-wave mixing due to self-group-phase locking inside a filament were observed [14, 16, 68]; the generation of high quality few-cycle pulses tunable from the UV [21] to the microwave becomes a possibility. Potential applications include remote pollutant detection [46], single-cycle pulse generation [39], lightning control [68], etc. These and other unforeseen possibilities constitute an emerging frontier called "filamentation nonlinear optics" [16]. The definition of a filament, however, is still puzzling. Liu *et al.* [69] found that multiple filamentation terminates prematurely due to diffraction by the plasma inside the filaments. Méchain *et al.* observed stable nonionizing channels extending over the distance of kilometers in air [70]. Ruiz *et al.* proposed the spontaneous generation of a filament without ionization in air due to soliton propagation for laser power lower than the collapse threshold [71]. The confusion is evident. What constitutes a filament?

In this chapter, we study the full evolution of a single filament in air both experimentally and numerically. It shows that filamentation consists of two ionizing sections, one with "efficient ionization" and the other, "weakly ionized" followed by the linear diffraction of a single fundamental mode pulse.

4.2 Experimental setup

Figure 4-1 shows the schematic experimental setup. A 10 Hz, 45 fs, 3.2 mJ, 800 nm Ti-sapphire laser beam was collimated by a telescope formed by a convex and a concave lens. The elliptical beam cross section at the exit plane of the telescope was 2.6 mm

---

* The results presented in this chapter are based on the following article: Y. Chen, F. Théberge, O. Kosareva, N. Panov, V.P. Kandidov, S.L. Chin, "Evolution and termination of a femtosecond laser filament in air", *Opt. Lett.* **32**, 3477 (2007).

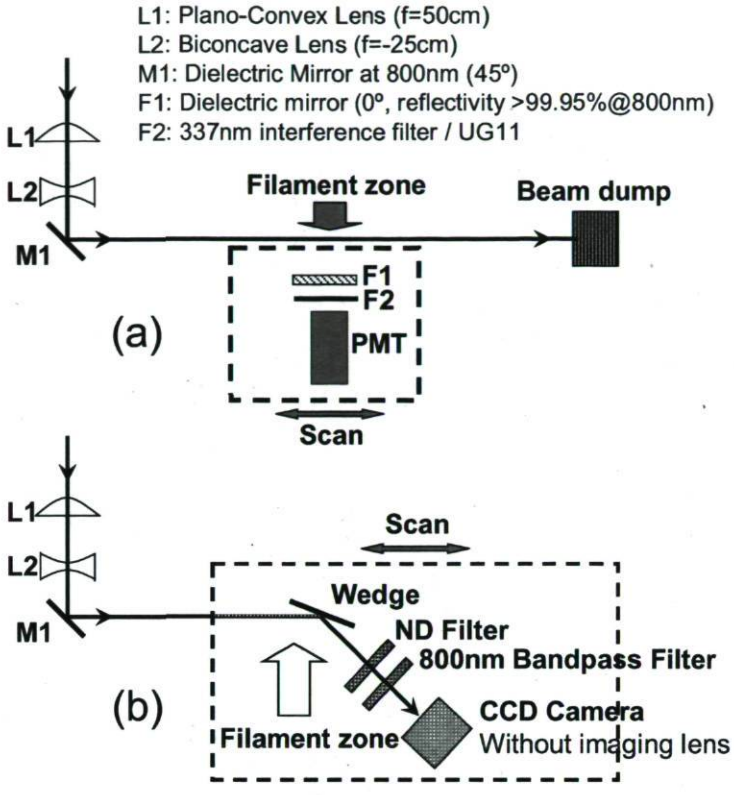

Figure 4-1: Schematic experimental setup.

(horizontal) × 2.7 mm (vertical) at FWHM. This plane was defined as the origin of the propagation z axis. We determined the plasma zone induced by filamentation by detecting the nitrogen fluorescence which is directly related to multiphoton/tunnel ionization [68] with a photomultiplier tube (PMT) from the side along the filament [69], as Fig. 4-1(a). A high reflectivity mirror at 800 nm and an interference filter at 337 nm were put in front of the PMT for measurement from z = 150 to 350 cm. Thereafter, the fluorescence signal became very weak; a bandpass filter (UG11, 2 mm thick, bandwidth of 200–400 nm) replaced the 337 nm filter. The UG11 filter transmits all the nitrogen fluorescence. The white light contamination is negligible because the spectral blue broadening in this experiment stops at 650 nm [inset of Fig. 4-2(a)]. We measured the background signal at z = 970 cm where there was no plasma. This value was subtracted from the weak

fluorescence signal using the UG11 filter and then normalized to the 337 nm data.

Later, a wedge was set inside the filament at a near grazing angle (~15°) to avoid damage, and a CCD camera measured the diameter of the reflected beam [Fig. 4-1(b)]. A bandpass filter centered at 800 ± 20 nm and neutral density (ND) filters were used in front of the CCD camera. The whole detection setup was installed on a breadboard, which could be translated parallel to the z axis.

4.3 Results and discussions

In the simulations, the system of Eqs. (6)–(13) of [72] corresponding to single filamentation is used.[+] It includes diffraction, group-velocity dispersion, instantaneous and delayed response of the Kerr nonlinearity, and plasma generation via multiphoton/tunnel ionization. The spatiotemporal integration domain consisted of 8192 grid points in time and 4096 grid points in the radial domain. The initial beam diameter was smaller (1.7 mm FWHM instead of 2.6 mm) so as to fit the earlier filament formation in the experiment caused mainly by the slightly convergent wavefront and imperfect beam shape, which are enhanced during the transmission of the laser pulse inside the glass telescope.

Figure 4-2(a) shows the fluorescence signal (log scale) and the energy evolution of the central hot spot at the fundamental wavelength as a function of z. The energy of the central hot spots taken by the calibrated CCD camera (Fig. 4-3) was obtained by integrating the fluence over the transverse area defined by $1/e^2$ level of the signal maximum. The integration area is either the whole beam profile [Figs. 4-3(a) and 3(b)] before the collapse at $z \approx 200$ cm, or just the central hot spot as soon as the filament is formed [from 210 to 280 cm, Figs. 4-3(c) and 3(d)]. At further distances, several diffraction rings around the central hot spot appeared [Figs. 4-3(f)-3(i)]; however the energy integration area still includes the hot spot only. Sharp decrease in the energy [Fig. 4-2(a)] from 100 to 190 cm is associated with the beam's self-contraction and filament

[+] The simulation in this chapter was done by Olga Kosareva and Nikolay Panov in M. V. Lomonosov Moscow State University.

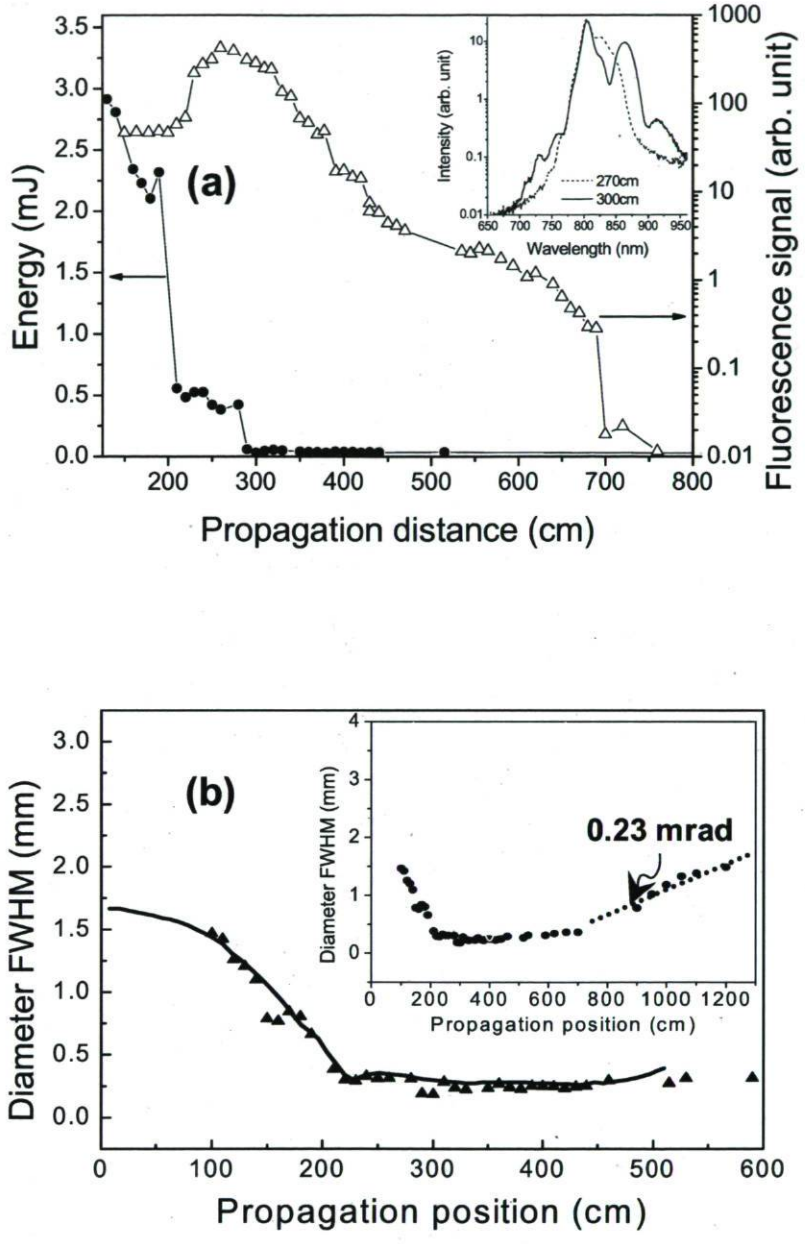

Figure 4-2: (a) Measured nitrogen fluorescence signal (open triangle) and energy evolution of the central hot spot at the fundamental wavelength (solid circle) as a function of the propagation distance. Inset: Spectrum at position 270 cm and 300 cm. (b) Measured beam diameters (FWHM, averaged for horizontal and vertical dimension) as a function of the propagation distance (solid triangle) and the numerical simulations (solid line). Inset: Divergence of a nonlinear propagated beam (with filament,

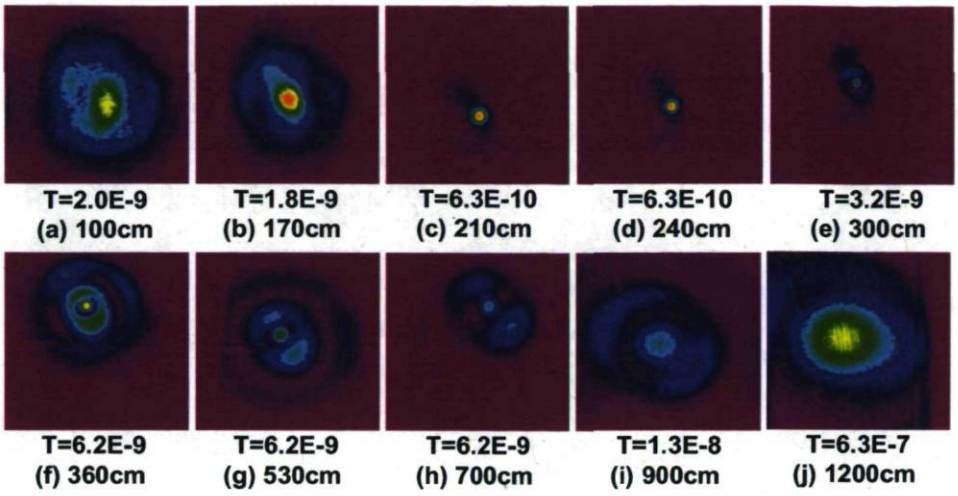

Figure 4-3: Some typical pictures taken by CCD camera along the propagation axis. T is the transmission of the beam before reaching the CCD.

formation. The latter is confirmed by a steep rise of the fluorescence signal within the region of 190-210 cm. From 280 to 300 cm in Fig. 4-2(a), there is a sudden drop in energy because it corresponds to the beginning of the significant spectral broadening [inset of Fig. 4-2(a)]. This white light is blocked by the 800 nm bandpass filter. The fluctuation of some data points [filled circles in Fig. 4-2(a)] in the energy could be due to the laser energy fluctuation. Between 210 to 280 cm, the energy of the collapsed central hot spot was ~475 μJ showing little tendency to decrease. Its peak power is ~10.6 GW assuming 45 fs pulse duration, while in reality, it should be higher, considering self-compression of the pulse. This peak power is still above the measured critical power for self-focusing of 8-10 GW in air [73]. The fluorescence signal underwent a strong decrease by 2 orders of magnitude from 250 to 450 cm, followed by a decrease by 1 order of magnitude from 450 to 690 cm. From 690 to 700 cm, the signal dropped sharply and fluctuated at noise level thereafter.

The evolution of the beam diameter (FWHM of the fluence distribution) is shown in Fig. 4-2(b). A sharp decrease until ~190 cm is followed by the slower one. The minimum of

0.18 mm is reached at ~300 cm. The beam diverges very slowly from a diameter of 0.25 to 0.37 mm at 450 cm< z < 700 cm. This is the zone where the fluorescence (ionization) is weak [Fig. 4-2(a)].

In the simulations, the calculated diameter of the filament [Fig. 4-2(b), solid curve] is in good agreement with the experimental data. To compare with the fluorescence signal which is roughly proportional to the electron density, we first follow the peak power of the whole pulse regardless of pulse splitting [Fig. 4-4(a)]. The peak power is compared with the critical power P_{cr} for self-focusing for a Gaussian beam given by $P_{cr} = \frac{3.77\lambda^2}{8\pi n_0 n_{2eff}}$ in SI units [54]. As suggested in [74], we use the effective value n_{2eff} of the nonlinear Kerr coefficient to fit the experimentally measured critical power of ~10 GW [73].

At 200 cm< z <300 cm, the leading subpulse (peak power $\cong 3P_{cr}$) dominates [Fig. 4-4(b), z = 252 cm] and the core energy is ~520 μJ, close to the experimental value of 475 μJ. For z>300 cm the leading subpulse depletes, the trailing subpulse sustains the core energy, and the intermediate part diverges strongly due to the plasma left behind by the leading subpulse [Fig. 4-4(b), z = 308 cm and z = 510 cm]. As a result, the core energy decreases, while the peak power still exceeds the P_{cr}. The calculated peak intensity in the region of 200-450 cm is clamped to ~5×10^{13} W/cm^2 [68], and the peak electron density is ~0.3×10^{-4} of the atmospheric density. The filament is represented by the "efficiently ionized" zone untill $z \approx$ 450 cm [Fig. 4-4(a)]. The region 450 cm< z <620 cm is characterized by the preservation of the peak power above P_{cr} but dominated by the trailing subpulse. The leading subpulse would no longer produce a plasma. In this case, the integrated electron density falls down an order of magnitude within 20 cm (440-460 cm). This decrease in electron density is similar to the decrease in fluorescence in Fig. 4-2(a). We call the filament in this region "weakly ionized". It is important to note that the defocusing effect by plasma in this zone, the dispersion and the diffraction are still able to dynamically interplay with the self-focusing effect to sustain a self-guided column [75]. Later on, by

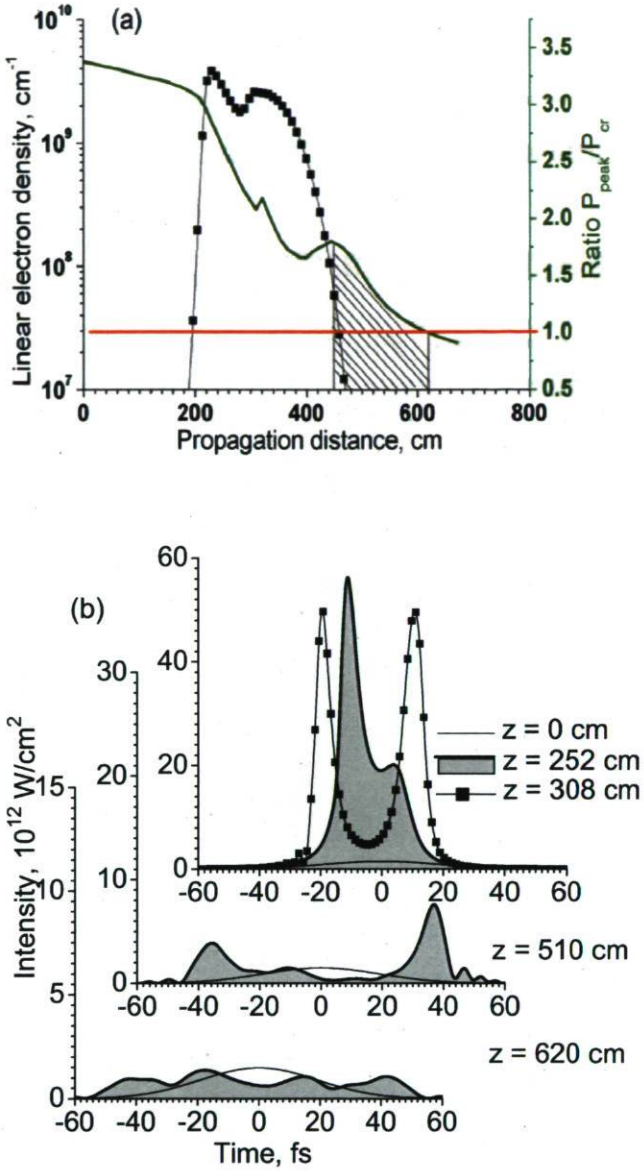

Figure 4-4: (a) Linear electron density (filled squares) and power in the most intense slice (solid curve) as a function of the propagation distance. Horizontal line shows P_{peak}/P_{cr} = 1. Dashed zone represents the weakly-ionized filament. Note non-monotonic power behavior at pulse splitting position $z \approx 300$ cm. (b) Curves with filled pattern are on-axis temporal intensity profiles at z = 252 cm, z = 510 cm, z = 620 cm, solid curve in each plot (not filled) indicates initial distribution of a Gaussian pulse. Curve, marked by squares, shows pulse splitting at z=308 cm. Note change in the intensity scale for the plots at each propagation distance.

$z \approx 700$ cm, material dispersion and diffraction overcome self-focusing [Fig. 4-4(b), z=620 cm] and ionization becomes negligible.

During filamentation, the initial pulse undergoes self-spatial filtering [14, 33] [Fig. 4-3(c)-3(h)]. The central part of the beam stays round throughout the filament zone (200-700 cm) and is always surrounded by the reservoir. After the filament zone, the laser pulse propagates linearly with a divergence of 0.23 mrad (FWHM) between 900 and 1200 cm [inset of Fig. 4-2(b)]. Our simulation yields 0.26 mrad.

We can now understand the observation of Méchain *et al.* [70]. The so-called "nonionizing channels" at long distances might very well be the local self-spatially filtered fundamental modes of various hot zones that diverge out slowly after the end of the plasma filament.

4.4 Conclusion

In conclusion, the evolution of the so-called single filamentation can be defined as follows: pulse contraction in the quasi-stationary regime (and self-spatial filtering) → efficiently ionized filament dominated by the leading subpulse → weakly ionized filament dominated by the trailing subpulse → linear diffraction of the self-filtered fundamental mode.

Chapter 5: Filamentation-induced continuous self-frequency down shift in air*

5.1 Introduction

Now it is known that a filament is a long ionization column with clamped intensity (around 5×10^{13} W/cm^2 in air) and a diameter of ~100 μm over a propagation distance much longer than the Rayleigh range. Therefore, any interaction by sampling this filament core results in high conversion efficiency (owing to high intensity inside the filament core), high stability (due to intensity clamping inside the filament core) and high spatial quality (thanks to spatial self-filtering of the pulse during filamentation) [14, 16, 68]. Several interesting experimental observations on third-order nonlinear interactions during filamentation in air, such as self-phase modulation (continuum generation), four-wave mixing [14, 21] and third-harmonic generation [22, 23], have already been reported. All these nonlinear processes during filamentation in bulk media such as air are very similar to those that occur in optical waveguides/fibers, since both of them provide a self-guided intense light column that is important for inducing efficient nonlinear interactions.

Continuous Raman self-frequency shift after the propagation of an intense pulse in an optical waveguide/fiber has already been extensively studied during the past several decades [76-78]. Physically, this can be understood by a combined action of self-phase modulation due to the optical Kerr effect and stimulated Raman scattering during the propagation of an intense ultra-short laser pulse inside a waveguide/fiber [79]. In the case of filamentation in air, spectral broadening towards infrared (IR) components has also been studied in the past several years [34, 80-82]. For example, Nibbering *et al.* observed red shift in spectra after filamentation in air, which is a consequence of molecular response to impulsive excitation of rotational coherences [80]. Bernstein *et al.*

---

* The results presented in this chapter are based on the following article: Y. Chen, F. Théberge, C. Marceau, H. Xu, N. Aközbek, O. Kosareva, S.L. Chin, "Observation of filamentation-induced continuous self-frequency down shift in air", *Appl. Phys. B* **91**, 219 (2008).

also observed spectral red-shift and its continuous red shift when increasing the input pulse energy [81]. However, all of the previous works investigated the spectral characteristics at a certain distance after the filamentation has terminated. To our knowledge, there is no paper reporting the spectral characteristics of the pulse propagating inside the filament zone. In this paper, we studied the spectral evolution inside the filament zone of a near IR femtosecond laser propagating in air. We observed that red-shifted spectral components will continuously self-frequency down shift with respect to the propagation distance when the pulse propagated in the filament zone, with its spectral envelope almost untouched. This will provide a new and cost-effective way in the generation of tunable IR pulses with good spatial beam quality.

5.2 Experimental setup

In our experiment, a 10 Hz, 800 nm, 50 fs Ti-sapphire laser beam was focused by a plano-convex lens. The beam diameter at the input plane of the convex lens was 4 mm (FWHM). This plane was defined as the origin of the propagation z axis. The schematic experimental setup is shown in Fig. 5-1. A wedge was set inside the filament core at a near grazing angle (roughly 15°) to avoid damage and directed the laser beam into an

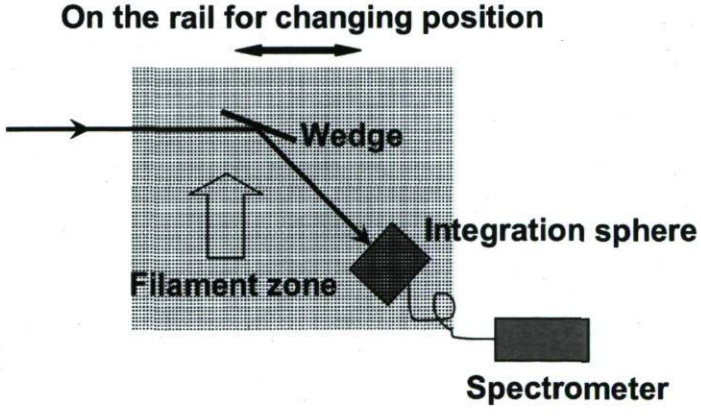

Figure 5-1: Schematic experimental setup.

integration sphere which was coupled with a liquid nitrogen-cooled spectrometer by a bundle of multimode optical fibers. The whole detection setup was installed on a breadboard which could be translated at different positions parallel to the z axis to measure the spectral evolution of the laser pulse. Three convex lenses with different focal lengths (1.5 m, 3 m and 4 m) were used for comparison. Due to the finite size of the lab, two plane gold coated mirrors were used to fold the beam for propagation distance above 600 cm. As this distance was longer than the focal length, the mirrors were not damaged.

5.3 Results and discussions

Figure 5-2(a) shows the spectral evolution of the laser pulse propagating in air, focused by a 3 m focal length lens, for input energy ranging from 0.35 mJ to 3.8 mJ.

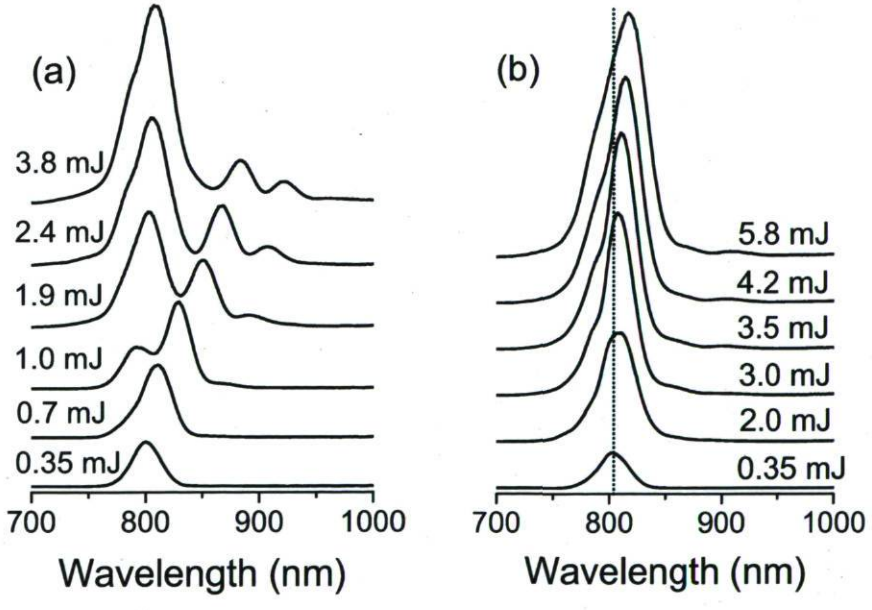

Figure 5-2: (a) Spectral evolution as a function of laser energy, focused by 3 m lens, measured at distance of 370 cm; (b) Spectral evolution as a function of laser energy, focused by 1.5 m lens, measured at distance of 320 cm. The dotted line is centered at 800nm.

The measurement was carried out at the propagation distance of 370 cm, around the end of the filament (2 mJ). Compared with the spectrum obtained at 0.35 mJ (whose power is smaller than the critical power, 10 GW, for self-focusing in air [73]), the spectrum of the pulse red-shifts a little at the energy of 0.7 mJ, splits into two peaks at the energy of 1.0 mJ and into three peaks at higher energies. Figure 5-2(b) shows the spectral evolution with a shorter 1.5 m focal length lens for input energy ranging from 0.35 mJ to 5.8 mJ. The spectra were taken at the propagation distance of 320 cm, beyond the filament. No obvious spectral splitting of the pulse can be observed except for a slight red-shift of the central wavelength with the increase of the input pulse energy.

Figure 5-3(a) displays the spectral evolution when measuring the spectrum along z, with pulse energy of 2.4 mJ focused by the 3 m lens. Two new IR peaks started to appear inside the filament zone (around z=300 cm). They continuously shifted to longer wavelength when z increased. We now follow the continuous wavelength shift of the dominant new IR peak. The wavelength shift as a function of z is shown in Figure 5-3(b) (squares). A strong red-shift (roughly from 800 nm to 865 nm) occurred during propagation inside the filament zone and saturated around 865 nm for propagation beyond the filament zone. The conversion efficiency, defined as the ratio of the resolved dominant new IR peak over the whole spectrum through integration in frequency scale, is about 22%. Figure 5-3(b) also shows the wavelength shift with input pulse energies of 1.0 mJ (circles) and 3.6 mJ (triangles). The wavelength shift for 1.0 mJ is about 35 nm, and 100 nm for 3.6 mJ. By comparing the three curves in Fig. 5-3(b), we can conclude that, at higher pulse energies (3.6 mJ), the self-frequency down shift starts earlier (around 260 cm) because filamentation begins at shorter z, which results in a longer self-guided column. In this case, the wavelength shift is more pronounced (about 100 nm). Figure 5-3(c) shows the spectral evolution when the laser pulses were focused by 4 m lens with pulse energy of 2.4 mJ. And the corresponding wavelength shifts are displayed in Fig. 5-3(d). Compared to the situation with 3 m lens, the red-shift is stronger (about 100 nm for 2.1 mJ and 130 nm for 3.6 mJ). This is due to a longer filament (self-guided column) generated in the case of 4 m lens. It is important to note

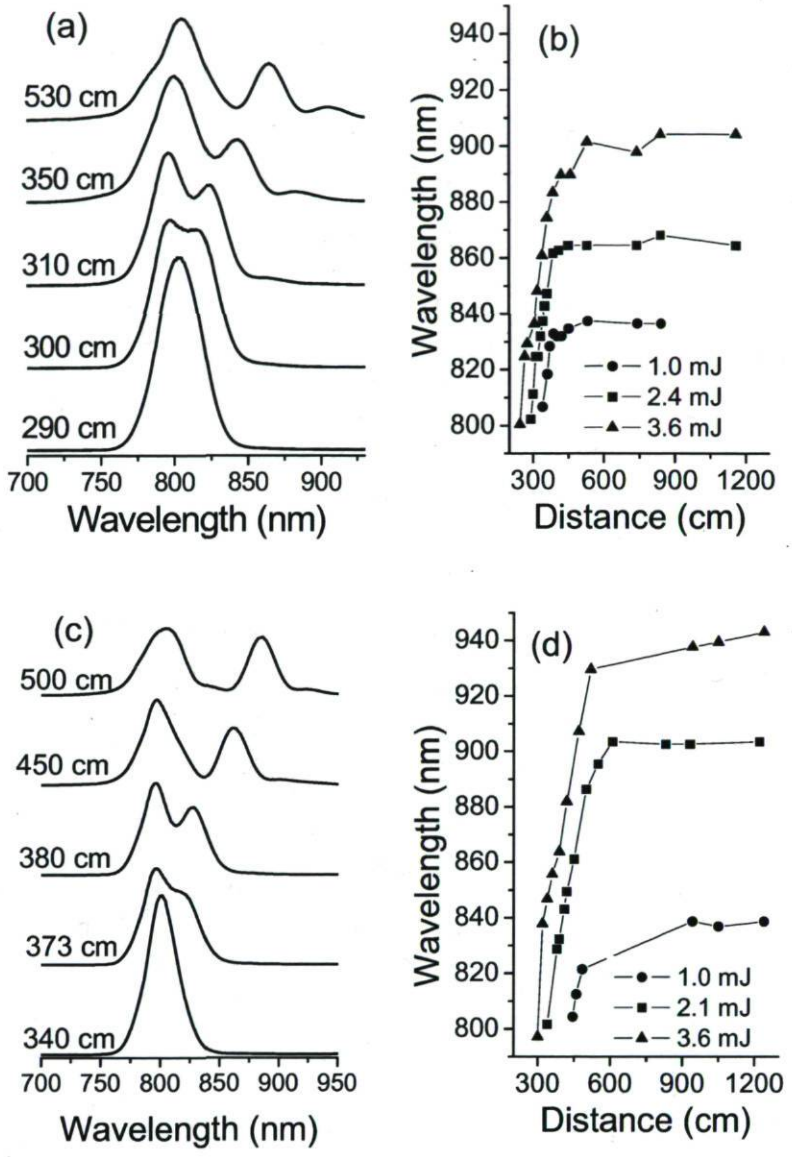

Figure 5-3: Spectral evolution as a function of propagation distance (a) at the pulse energy of 2.4 mJ focused by 3 m lens and (c) at the pulse energy of 2.1 mJ focused by 4 m lens; Wavelength shift as a function of propagation distance (b) with 3 m lens at the pulse energy of 1.0 mJ (circles), 2.4 mJ (squares) and 3.6 mJ (triangles); (d) with 4 m lens at the pulse energy of 1.0 mJ (circles), 2.1 mJ (squares) and 3.6 mJ (triangles).

that the transmission of the laser pulse through the lens did not affect the current observations since by using reflective concave mirror we observed similar IR spectral shift.

In order to further investigate the underlying physical mechanism of the generation of the red-shifted new IR peaks, experiments were carried out in a 4.5 m chamber filled with either air (Raman active) or Argon (non Raman). Figure 5-4 shows the schematic experimental setup. The 4.5 m chamber was put in the pathway of the filament zone which was formed by a 2.75 mm (FWHM) collimated beam with pulse energy of 3.2 mJ. To avoid the generation of white light in the windows of the chamber, a small hole was made on both the input and the output window. In Figure 5-5, we present the measured spectrum of the pulse at the output of a gas chamber first filled with air (Raman-active medium, solid line) and then with Argon (non-Raman-active medium, purity ~90%, dashed line). It is important to note that, in intensity clamping of filaments in air, the ionization of O_2 contributes more to the overall ionization of air [60]. Therefore, the clamped intensity reached in air is lower than in Argon since the ionization potential of

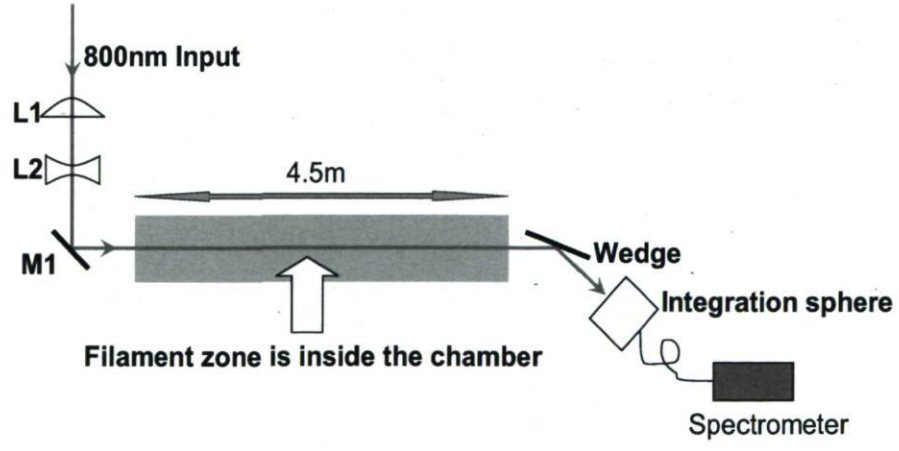

Figure 5-4: Schematic experimental setup with a 4.5-m-long chamber filled with air or Argon.

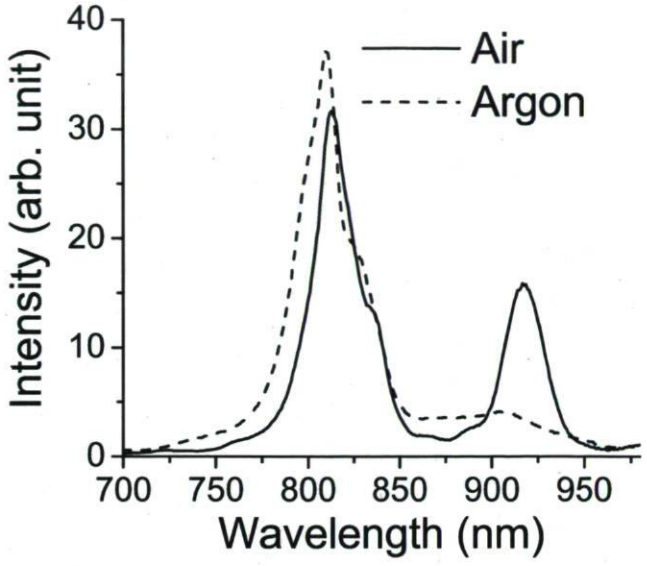

Figure 5-5: Comparison of spectra formed by filamentation in air (solid line) and in Argon (dash line).

O_2 (12.1 eV) is lower than that of Argon (15.6 eV). Thus, we expect more pronounced spectral broadening during the filamentation in Argon if the Raman response were not a reason. However, a pronounced new IR peak as shown in Figure 5-5 was observed during the filamentation in air and no IR peak was observed when the chamber was filled with Argon gas. Therefore, the generation of the separated new IR peaks is due to the contribution of the Raman effect. The red-enhanced spectral shift similar to those measured here has been attributed to a purely rotational Raman process [80, 83]. The first Stokes shift due to rotational effect from N_2 (12 cm^{-1}) and O_2 (8.4 cm^{-1}) corresponds approximately to a wavelength shift of 1.5 nm and 1.1 nm, respectively. These Stokes shifts are much smaller than the initial spectral bandwidth of the laser pulse, and thus, we cannot resolve them. During filamentation, cascaded Stokes shift [79] occurred and the generated IR pulse continuously shifted towards longer wavelength. Because the spectral bandwidth of the newly generated IR pulse is much wider than the first Stokes shift due to rotational effects from N_2 and O_2, the

low-frequency spectral components of the pulse, acting as a seed, can be amplified by Raman gain while the high-frequency spectral components of the same pulse work as a pump. This is similar to continuous Raman self-frequency shift by intra-pulse Raman scattering in optical waveguide/fiber [79]. This results in continuous self-frequency down shift along the propagation of the pulse inside the filament zone. In the case of a fiber, all pulses are confined inside the fiber core. In the present case of filamentation, we suspect that the Raman pulse, once created inside the filament, is phase-locked to the pump pulse (self-group-phase locking [14, 33, 84]). Thus, the Raman pulse stays inside the filament (i.e. propagates together with the pump pulse inside the filament core) while undergoing cascaded Stokes shift. Once outside the filament core, linear diffraction would make the pulse intensity too weak to undergo further cascaded Stokes shift.

Figure 5-6 shows the beam profile at the central wavelength of (a) 800 nm and (b) 900 nm by using appropriate band-pass filters at z = 600 cm (the end of the filament) with pulse energy of 2.1 mJ focused by 4 m lens. Clearly, the spectral component of 900 nm (new IR peak) has an excellent spatial quality [Fig. 5-6(b)] when compared to the input

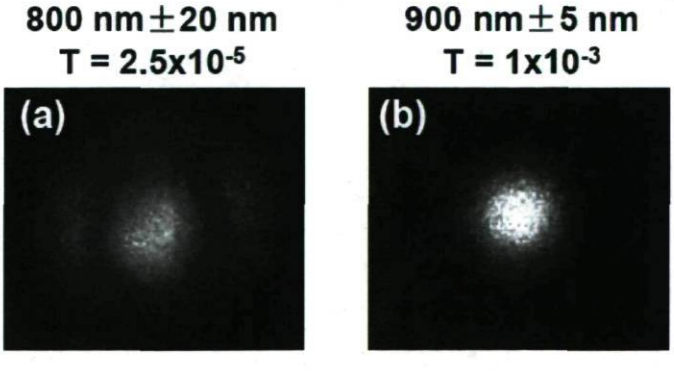

Figure 5-6: Beam profile of the laser beam at propagation distance of 6 m away from 4 m focal length lens with filter centered at wavelength (a) 800 nm and (b) 900 nm before the CCD camera. T is the transmission of the beam before reaching the CCD camera.

spatial mode for the spectral component of 800 nm [Fig. 5-6(a)]. This nice profile of the isolated IR peak is due to the nonlinear interactions sampling the self-cleaned high-intensity filament core [14, 17].

From the above experimental observations, one important condition for filamentation-induced continuous self-frequency down shift is that the self-guided column (filament) generated by filamentation should be long enough. It is also important to note that the wavelength shift as a function of the propagation distance in the filament zone generated in air is almost linear for all the cases shown in Fig. 5-3(b), (d). Thus the length of the filament formed by the 1.5 m lens is too short and the red-shifted new IR peaks have no chance to separate from the main peak [see Fig. 5-2(b)] since the wavelength shift evolves progressively along the propagation distance in air. Figure 5-5 pointed out that the generation of the new IR peaks occurs during the filamentation over a long enough distance in a Raman active medium.

5.4 Conclusion

In conclusion, filamentation-induced continuous self-frequency down shift in air, a new filamentation nonlinear optical process, has been experimentally studied. We have shown that the self-conversion behavior during the propagation in a filament is similar to the propagation in an optical waveguide. The measured continuous self-frequency down shift during filamentation in air has a strong dependence on the length of a filament. By further optimization, this technique could be used for an efficient and high beam quality IR laser source. Furthermore this technique could be scaled to much higher pump energies as compared to fibers or wave-guides techniques.

Chapter 6: Polarization separator created by a filament in air*

6.1 Introduction

The high intensity in the filament zone not only launches some interesting nonlinear effects, but also induces symmetry-breaking in the propagation medium. It was demonstrated by P. Béjot *et al.* that remarkable birefringence is induced by filaments of ultrashort laser pulses in Argon [26]. As a result, the filament can work as a waveplate in Argon. This phenomenon results from the difference between the nonlinear refractive indices induced by the filament on the axes parallel and orthogonal to its polarization in the atomic Argon gas.

In this chapter, we demonstrate that a filament induced by a femtosecond laser pulse in air can act as a "polarization separator" for a co-propagating femtosecond probe pulse: it guides the probe component with polarization parallel to that of the pump along the propagation axis through molecular alignment, and diffracts the probe component with orthogonal polarization to an outer ring.

6.2 Experimental setup

In our experiment, an 800 nm, 75 fs (slightly negatively chirped) Ti-sapphire laser beam was split into two. The first beam (1.1 mJ/pulse) was used as a pump to generate a single filament in air at ambient pressure. The second beam was frequency-doubled to 400 nm by a BBO crystal and was used as a probe (3 μJ/pulse). Figure 6-1 schematically illustrates the experimental setup. The two beams were combined together by an unpolarized dichroic mirror (DM, with high reflective coating at 400 nm on one side and anti-reflective coating at 800 nm on the other side). Both of them were initially linearly polarized and were focused by a plano-convex lens with a focal length

* The results presented in this chapter are based on the following article: Y. Chen, C. Marceau, F. Théberge, M. Châteauneuf, J. Dubois, S.L. Chin, "Polarization separator created by a filament in air", *Opt. Lett.* 33, 2731 (2008).

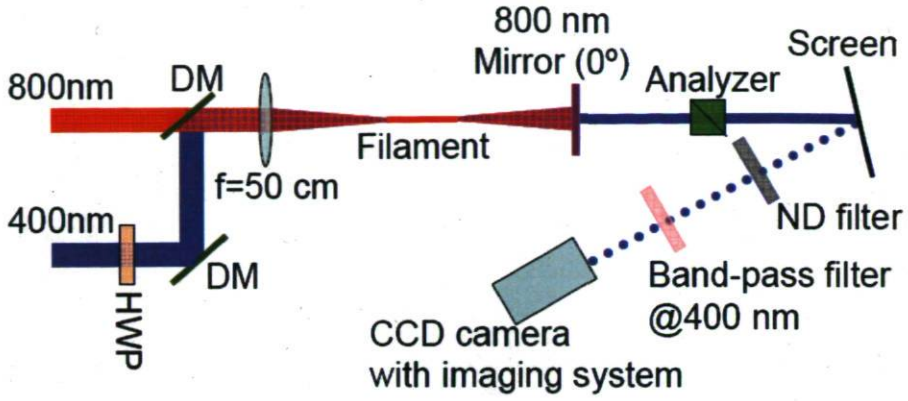

Figure 6-1: Schematic illustration of the experimental setup. Time delay of the probe beam (400 nm) can be varied by a delay line which is not shown.

of 50 cm. The length of the filament is around 3 cm. The polarization of the pump was maintained horizontal throughout the whole experiment while that of the probe was controlled by a half-wave plate (HWP). An 800 nm mirror (0°) was put after the filament to block the pump beam while transmitting the probe beam. A paper screen was set around 1 meter after the filament and a CCD camera recorded the fluence distribution of the probe scattered by the screen. A band-pass filter centered at 400 nm (bandwidth=40 nm or bandwidth=10 nm) and neutral density (ND) filters were used in front of the CCD camera. The polarization of the probe beam was analyzed by a cube polarizer which was placed just after the 800 nm mirror (0°).

6.3 Results and discussions

To verify the time delay between the pump and the probe, we inspected the transmission of the central part of the probe (initially forming a 45° angle with the pump) through a crossed analyzer. This analyzer blocked the probe transmission in the absence of the pump. When the pump was turned on, it breaks the isotropy of the gaseous medium which results in a nonzero transmission of the probe, as shown in Fig. 6-2(a) and (b). In

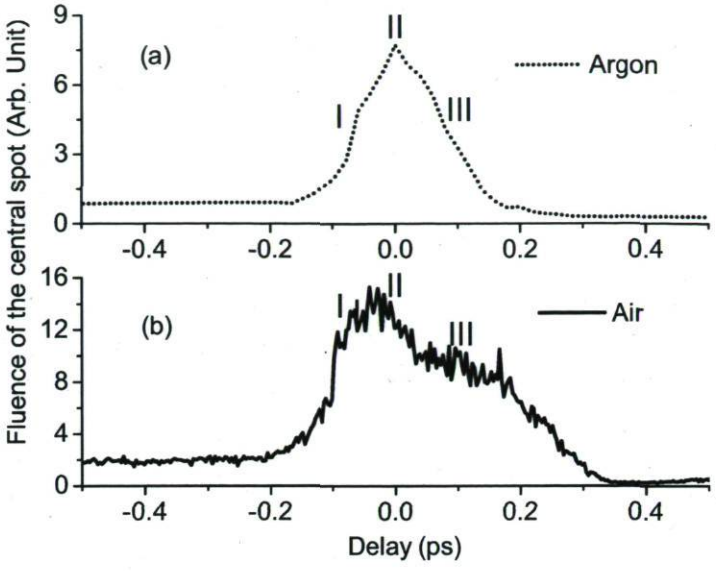

Figure 6-2: Integrated fluence of the central spot in the probe beam as a function of the time delay between the pump and the probe in (a) argon and (b) air.

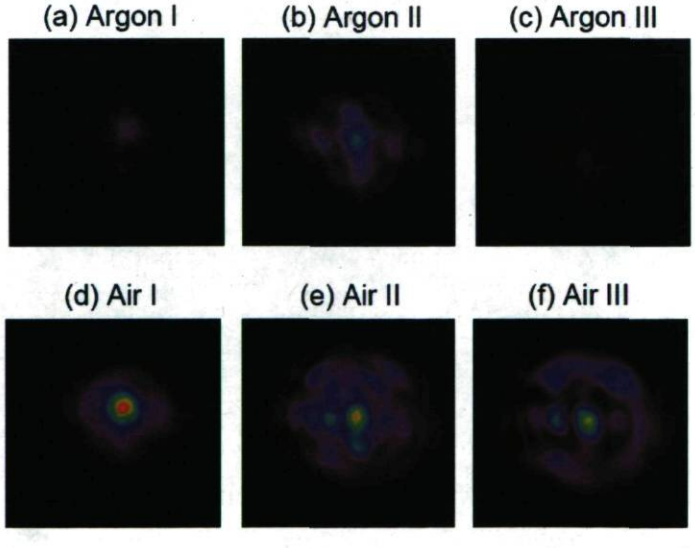

Figure 6-3: Typical probe profiles after interaction with the pump in Argon at time delay (a) I, (b) II, (c) III and in air at time delay (d) I, (e) II, (f) III. The analyzer is crossed with respect to the input probe polarization. The color scale is the same for all images.

Argon, this phenomenon is attributed to the instantaneous electric cross phase modulation [26]. So the origin (0 ps) of the time axis was defined where maximum probe transmission was observed through the crossed analyzer in Argon [as Fig. 6-2(a)] since cross phase modulation was optimized with optimal temporal overlap between the pump and the probe. The probe beam patterns obtained at Delay I, II and III (as Fig. 6-2) are shown in Fig. 6-3(a)-(c) for Argon and Fig. 6-3(d)-(f) for air. Compared with the results obtained in Argon, a delayed birefringence effect was observed in air [as Delay III in Fig. 2(b) and Fig. 6-3(f)]. For further experiment in this chapter, we fixed the time delay at Delay III.

Figure 6-4 illustrates an evolution of the probe beam profile in air as a function of the orientation of the analyzer, with an initial probe polarization forming a 45° angle with respect to the pump polarization. Each picture [Fig. 6-4(b)-(g)] (averaged over 23 shots) was obtained at a specified analyzer angle. The color scales in all the pictures are the

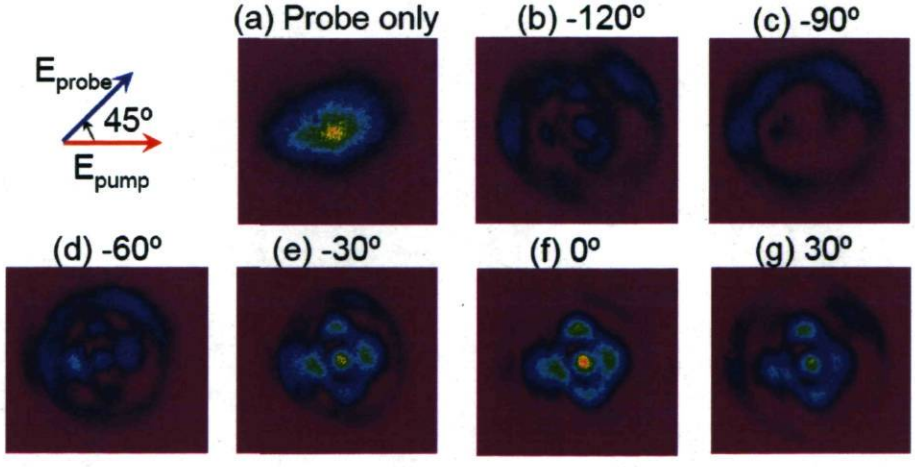

Figure 6-4: (a) Typical beam profile of the probe in air. Typical beam profiles of the probe after interaction with the pump taken at polarizer orientation of (b) -120°, (c) -90°, (d) -60°, (e) -30°, (f) 0° and (g) 30° when initial probe polarization is 45° with respect to the pump polarization.

same. The analyzer transmits horizontally polarized light (parallel to the pump polarization) when its orientation is set to 0° and it transmits vertically polarized light (orthogonal to the pump polarization) at -90°. We observe an interesting beam pattern when the analyzer is oriented at 0° [Fig. 6-4(f)]: a central spot is surrounded by four hot spots that are linked together by a weak ring (defined as Flower Pattern in the rest of the text). When the polarizer is turned away from 0°, the Flower Pattern gets weaker, accompanied by a gradually emerging outer ring [as shown in Fig. 6-4(b), Fig. 6-4(d), Fig. 6-4(e) and Fig. 6-4(g)]. Eventually, the Flower Pattern disappears completely and one strong outer ring takes over when the analyzer is oriented at -90° [Fig. 6-4(c)]. Obviously, the Flower Pattern is composed of the probe components with parallel-to-pump polarizations while the outer ring comes from the probe components with orthogonal polarization. As a consequence, the laser-induced filament acts as a "polarization separator". It spatially separates the two orthogonal polarizations of the probe.

Figure 6-5 shows a quantitative polarization analysis of each part of the probe beam pattern in air. The initial linear probe polarization forms a 45° angle with the pump polarization. Each experimental point (symbol) was obtained by integrating the fluence distribution over selected area of the pictures at an angle of the analyzer ranging from -140° to 60°. Each experimental curve was normalized to 1. The curves in solid line are fittings by using Jones's matrix formalism [85]. For both the central spot and the ring in the Flower Pattern [Fig. 6-4(f)], the filament was modeled as an ideal polarizer whose transmission axis is parallel to the pump polarization [solid line in Fig. 6-5(a) and Fig. 6-5(b)]. For the outer ring [Fig. 6-4(c)], the filament is modeled as a polarizer whose transmission is perpendicular to the pump polarization [solid line in Fig. 6-5(c)]. The experimental results show that the central spot [solid squares in Fig. 6-5(a)] and the ring in the Flower Pattern [solid circles in Fig. 6-5(b)] remain highly linear and their polarizations are parallel to the pump, which fits well with the simulations [solid line in Fig. 6-5(a) and Fig. 6-5(b)]. The polarization of the outer ring [solid triangles in Fig. 6-5(c)] is perpendicular to the central spot and to the ring in the Flower Pattern, hence,

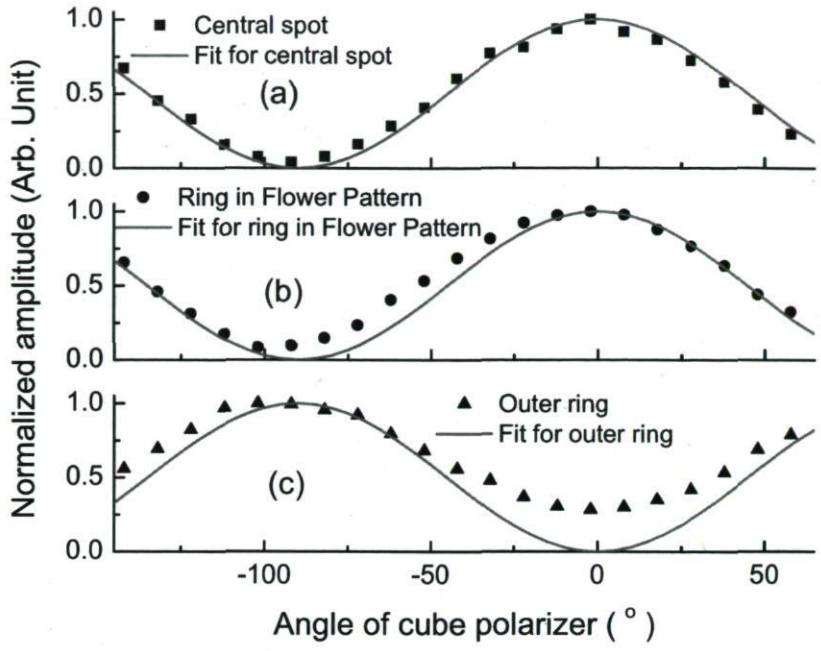

Figure 6-5: Polarization analysis of (a) central spot (solid squares), (b) ring in Flower Pattern (solid circles) and (c) outer ring (solid triangles) of the probe when it co-propagates with an initial 45° polarization angle with respect to the pump. Solid lines in (a), (b) and (c) are the fittings. The polarizer transmits horizontally polarized pulse when it is oriented at 0°.

orthogonal to the pump. The extinction ratio ($I_{\min}^{probe} / I_{\max}^{probe}$) of the outer ring (~1:4) is somewhat higher than that of the central spot (~ 1:20). It proves that some parallel-to-pump-polarization probe components are diffracted out into the outer ring, but that almost no perpendicular-to-pump-polarization probe components transmits through the core of the filament.

For further verification, we analyzed the probe central spot polarization in air using different initial polarizations (Fig. 6-6). The experimental and simulated curves are obtained in the same way as described above for Fig. 6-5. This figure confirms that,

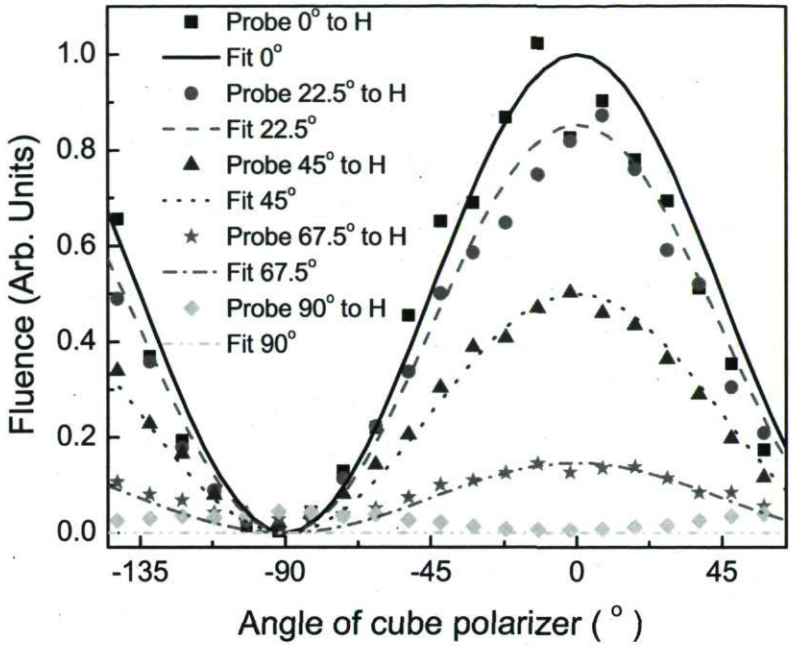

Figure 6-6: Polarization analysis of the central spot of the probe after interaction with the pump when initial probe polarization is 0° (solid squares, solid line), 22.5° (solid circles, dash line), 45° (solid triangles, dot line), 67.5° (solid pentagons, dash-dot line) and 90° (solid diamonds, dash-dot-dot line) with respect to the pump (horizontal). Experimental measurements are in scattered symbols and fittings in line. "H" refers to the horizontal polarization of the pump.

after the interaction with the filament core, the polarization of the probe central spot is always parallel to the pump (solid squares, solid circles, solid triangles and solid pentagons in Fig. 6-6), regardless of the initial probe polarization. The experimental curve obtained with the initial probe polarization orthogonal to the pump (solid diamonds in Fig. 6-6) highlights the good property of the filament-induced polarization separator in the central region, showing less than 5% transmission for the perpendicular polarization, i.e., extinction ratio $\leq$ 1:20. Good quantitative agreement between the

experimental results and the simple theoretical model proves that a filament is able to act as a polarization separator for co-propagating pulses at any input polarization. This polarization separator effect recurs when changing the probe-pump delay by $1/4T$ interval (T = 8.3 ps for N_2 and T = 11.6 ps for O_2), where T is the rotational period.

The mechanism of the observed filament-induced polarization-separating effect can be explained by the difference in the refractive indices along two orthogonal directions which is attributed by molecular alignment of the rotational excited molecules in a filament wake. In the case of air, both N_2 and O_2 are prolate spheroid molecules. Thus, the polarizability α_3 (parallel to its symmetry axis) experienced by the laser field is larger than the polarizability α_1 (perpendibular to its symmetry axis), i.e., $\alpha_3 > \alpha_1$. In the wake of an intense laser field, a torque will twist the molecules into alignment with the laser field [86]. The sum of the rotational modes, phase-locked by the laser pulse, produces periodic molecular alignment recurrences. As a consequence, the change in the refractive indices parallel and perpendicular to the laser field (pump) can be noted as:

$$\Delta n(r,t)_{// pump} = 2\pi \cdot N \cdot n_0^{-1} \cdot \Delta\alpha \cdot (\langle \cos^2\theta \rangle_t - 1/3), \tag{6-1}$$

$$\Delta n(r,t)_{\perp pump} = \pi \cdot N \cdot n_0^{-1} \cdot \Delta\alpha \cdot (1/3 - \langle \cos^2\theta \rangle_t), \tag{6-2}$$

respectively, where N is molecular density, n_0 is isotropic refractive index, θ is the angle between the laser polarization and molecular axis, $\Delta\alpha = \alpha_3 - \alpha_1$, and $\langle \cos^2\theta \rangle_t$ is the expectation value of $\cos^2\theta$ (or alignment factor). Hence,

$$\Delta n(r,t)_{\perp pump} = -\frac{1}{2}\Delta n(r,t)_{// pump}. \tag{6-3}$$

Figure 6-7 shows the measured alignment of 1 atm of N_2 and O_2 at room temperature (295 K) by a 110 fs, 800 nm, 4.1 x 10^{13} W/cm^2 laser pulse [87]. The effective alignment of air is synthesized from the N_2 and O_2 plots. Periodic and sharp molecular alignment recurs at $1/4T$ intervals where T = 8.3 ps for N_2 and T = 11.6 ps for O_2. Delay

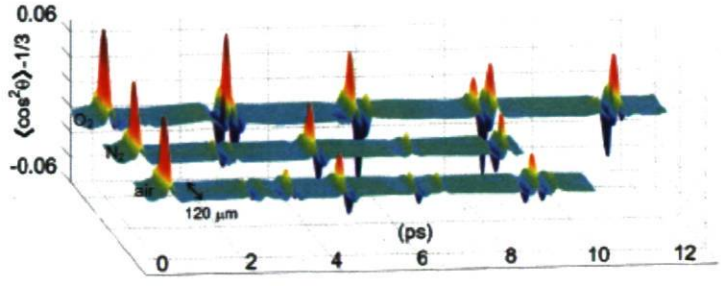

Figure 6-7: Measured alignment of 1 atm of N_2 and O_2 at room temperature (295 K) by a 110 fs, 800 nm, 4.1 x 10^{13} W/cm^2 laser pulse. The effective alignment of air is synthesized from the N_2 and O_2 plots.

III specified in Fig. 6-2 and Fig. 6-3 corresponds to the first peak (~100 fs) in Fig. 6-7 where the transient alignment, represented as $\langle\cos^2\theta\rangle_t - 1/3$, reaches its maximum. Thus, on the one hand, the probe component having a parallel-to-pump polarization sees a positive change in refractive index ($\Delta n(r,t)_{//\,pump} > 0$) induced by molecular alignment. This convex refractive index profile, overcoming the pump-induced plasma defocusing effect, guides the probe component with parallel-to-pump polarization inside the filament wake [see Fig. 6-4(f)]. The four hot spots on the weak ring in the Flower Pattern are probably due to the elliptical input beam profile in our experiment [88]. They are located symmetrically along the major and minor axis of the initial beam profile. On the other hand, regarding the probe component with an orthogonal-to-pump polarization, the molecular alignment induced nonlinear contributions to the refractive index is negative ($\Delta n(r,t)_{\perp pump} < 0$), i.e., reaching its minimum at Delay III. This, together with the laser induced plasma defocusing effect, results in an anti-guiding profile of the probe, hence, forming an outer ring [see Fig. 6-4(c)].

6.4 Conclusion

In conclusion, we demonstrated that a femtosecond pulse-induced filament in air can act

as a "polarization separator" for a co-propagating probe pulse. After interaction with the pump, the probe is separated spatially into two parts: one part (having polarization parallel to the pump) is guided by the pump and remained on the propagation axis [see Fig. 6-4(f)]; the other part (with orthogonal-to-pump polarization) is diffracted out to an outer ring [see Fig. 6-4(c)]. The polarization of the probe can be easily manipulated by simply changing the polarization of the pump. This technique provides a totally new broadband polarization separator which acts on a femtosecond timescale window, opening new possibilities for ultrafast information processing and telecommunications.

Chapter 7: THz emission from one-color filament*

7.1 Introduction

Filament-induced symmetry-breaking in air is expected to play an important role in some nonlinear processes inside the air-filament, one of which is THz radiation from a one-color filament. More and more attention is paid to Terahertz (THz) radiations due to their promising applications such as in high resolution imaging, chemical spectroscopy, biomedical diagnostics and threat detection [89-91]. So far, the most established technique for generation of THz radiation has been optical rectification, which achieves frequency down conversion of laser pulses via the second order polarizability $P_i(\omega) = \chi^{(2)}_{ijk}(\Omega, \omega+\Omega, -\omega)E_j(\omega+\Omega)E^*_k(-\omega)$ in non centro-symmetric crystals, where Ω and ω are the THz and optical frequencies, respectively [92, 93]. However, THz radiation by this technique is not suitable for long distance propagation due to significant attenuation by water vapor during propagation in air. THz waves emitted from a filament have attracted special interests because they can be created remotely by manipulating the location of a filament, minimizing the strong absorption by water vapor in the atmosphere between the source and target [4, 24]. It has been demonstrated by D'Amico *et al.* that the strong THz emission from a femtosecond laser filament in air is radially polarized and confined to a forward cone [24]. Their conclusion was based on the measurement obtained with heterodyne detection (sensitive to 0.1 THz). This was interpreted as a transition-Cherenkov radiation from the plasma space charge moving at light velocity in the wake of a femtosecond laser filament. Recently, the generation of elliptically polarized THz pulses from a filament was observed by Zhang *et al.* The polarization was determined by qualitative observations [94].

This chapter presents the results of the polarization characterization of THz waves

---

* The results presented in this chapter are based on the following article: Y. Chen, C. Marceau, W. Liu, Z.-D. Sun, Y. Zhang, F. Théberge, M. Châteauneuf, J. Dubois, S.L. Chin, "Elliptically polarized Terahertz emission in the forward direction of a femtosecond laser filament in air", *Appl. Phys. Lett.* **93**, 231116 (2008).

emitted from a femtosecond laser filament in air in the forward direction by using a wire grid polarizer and electro-optic sampling technique (sensitive to frequency below 4 THz). We directly observed that the electric field vector of the THz pulse emitted from a filament obeys an ellipse confirming elliptically polarized THz radiation.

7.2 Experimental setup

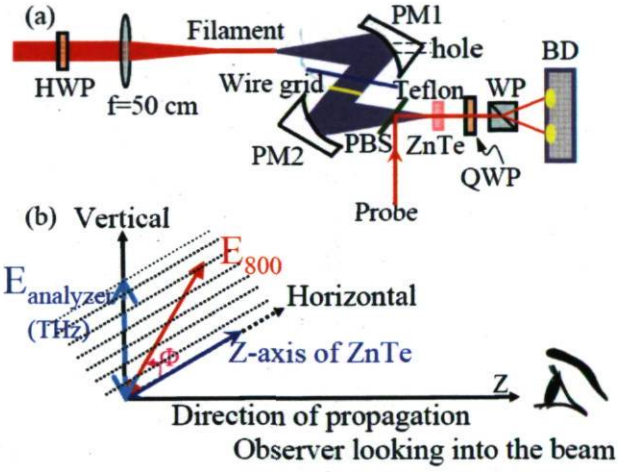

Figure 7-1: Schematic illustration of (a) the experimental setup and (b) orientation of maximum transmission of the wire grid, *Z* axis [0,0,1] of the ZnTe crystal and pump polarization. "WP" and "BD" are wollaston prism and balanced detector, respectively.

A 1 kHz, 800 nm, 45 fs Ti-sapphire laser beam was split into two beams, one as the pump (1.15 mJ/pulse) for THz generation via a filament in air, the other as the weak probe for the electro-optic sampling (EOS) detection of the THz pulse [Fig. 7-1(a)]. The EOS technique is detailed in Appendix. A filament 2 cm in length was generated. A half-wave-plate (HWP) was inserted before the lens for controlling the polarization of the pump. The THz radiations emitted from the filament were collected and collimated by a parabolic mirror (PM1) having 4-mm-diameter hole in its center. The collimated THz pulses were focused by a second parabolic mirror (PM2) and detected by the standard time-resolved EOS method with a 1 mm thick <110> oriented ZnTe crystal

[95]. The diameter and focal length of both parabolic mirrors were 5 cm and 10 cm, respectively. A 5-mm-thick Teflon plate was inserted between the two parabolic mirrors to block residual fundamental pulses and white light from the filament. The polarization of the THz pulse was analyzed by a wire grid (THz polarizer) located just after the Teflon plate. Figure 7-1(b) shows the orientation of maximum transmission of the wire grid (vertical) and Z axis [0,0,1] of the ZnTe crystal (horizontal). We characterized the THz polarization by rotating the polarization of the pump, which was equivalent to rotate the polarization of the THz pulse. The polarization of the probe was kept constant. ϕ is the angle between the linearly polarized pump and the Z axis of the ZnTe crystal. The origin (0°) is set when the pump is horizontally polarized [Fig. 7-1(b)]. For obtaining spatial overlap between the THz pulse and the probe in the ZnTe crystal, the Teflon plate was removed and the ZnTe crystal was replaced by an iris. Then alignment of the pump and the probe was performed to make sure both the probe and the residual fundamental pulse (or white light) from the filament passed through the same iris.

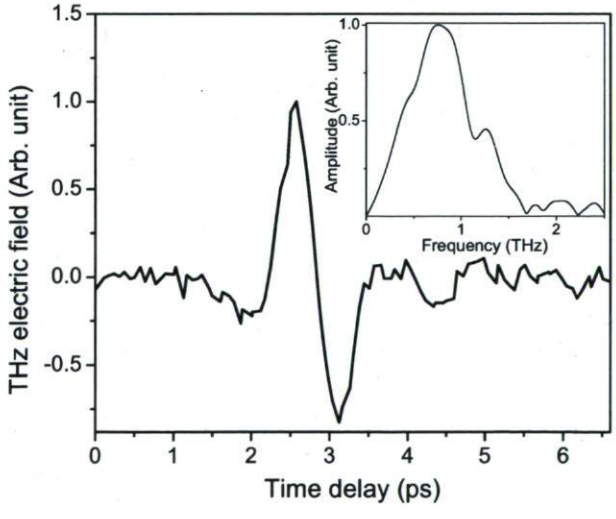

Figure 7-2: Typical experimental THz electric field waveform and the corresponding amplitude spectrum (solid curve) in the inset.

7.3 Results and discussions

Figure 7-2 shows typical experimental THz electric field obtained by time-resolved EOS technique. The corresponding amplitude spectrum and phase are given in the inset of Fig. 7-2, which are obtained from Fourier transform of the THz electric field.

Figure 7-3 illustrates the evolution of the THz electric field intensity (solid squares) as a

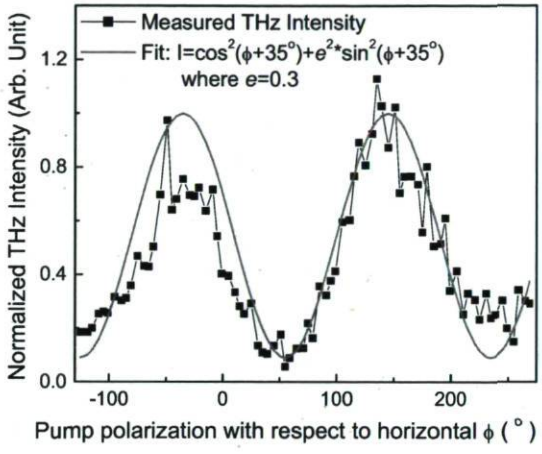

Figure 7-3: Measured (solid squares) and fitted (solid curve) intensity evolution of the THz electric field as a function of the polarization orientation of the pump ϕ.

function of ϕ. Each point was obtained by squaring the peak-to-peak amplitude of the THz electric field measured at the given ϕ. It is clear that the polarization of the THz pulse is not purely linear as the curve of measured intensity in Fig. 7-3 does not reach zero as Malus's law for a linearly polarized light passing through an analyzer predicts: $I = I_0 \cos^2\theta$. The intensity curve is well fitted (solid curve, Fig. 7-3) by using the following equation:

$$I = \cos^2(\phi + \phi_0) + e^2 \sin^2(\phi + \phi_0), \qquad (7\text{-}1)$$

where $e = 0.3$ and ϕ_0=35°. Analytically, Eq. (7-1) is a combination of two orthogonal

components. The THz pulse polarization can therefore be considered as the superposition of two decomposed linearly polarized components with orthogonal polarizations. As a consequence, the polarization of the measured THz pulses can be either partially polarized or elliptically polarized with ellipticity ($e = E_{THz,MinorAxis}/E_{THz,MajorAxis}$) of 0.3.

An elliptically polarized wave can be resolved into an arbitrary set of mutually orthogonal component waves with their polarization planes perpendicular to each other and with a fixed phase difference. By recomposing the THz electric fields obtained at two orthogonal directions (i.e., ϕ and ϕ+90°), it is feasible to derive the elliptical trajectory if the THz pulse is elliptically polarized. Two typical THz electric fields experimentally measured at two orthogonal directions are shown in the inset of Fig. 7-4. We define the THz electric field obtained at ϕ=15° as *X* and the electric field at ϕ=105° as *Y*. When they are plotted in an *X*-*Y* graph, a closed polarization trajectory is observed

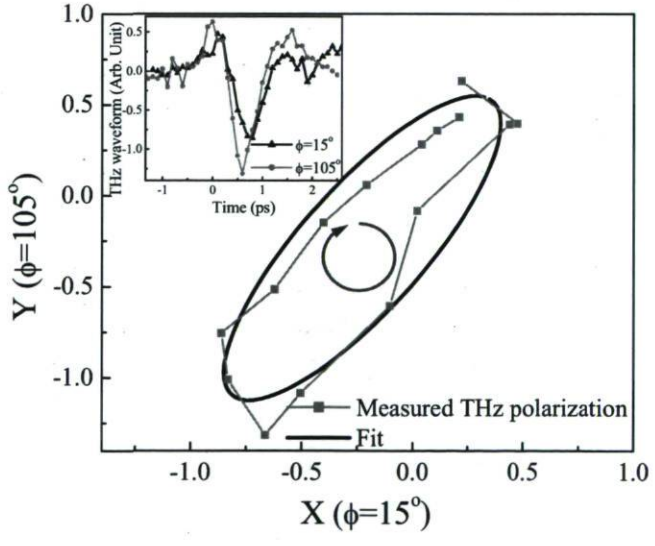

Figure 7-4: Measured (solid squares) and fitted (solid curve) THz polarization. The arrow indicates the rotating direction of the THz electric field vector. Inset: Typical experimental THz electric field waveforms obtained at two orthogonal directions (solid triangles: ϕ=15° and solid circles: ϕ=105°).

(solid squares, Fig. 7-4). Each solid square corresponds to the measured THz amplitudes in two orthogonal directions at one specified time delay; two successive solid squares are separated by 100 fs. The resulting THz electric field vector ends up rotating clockwise as time advances, as indicated by the arrow in Fig. 7-4 when looking into the beam as Fig. 7-1(b). This trajectory is well fitted by an ellipse (solid curve, Fig. 7-4) with ellipticity = 0.3. This value corroborates the ellipticity derived from the THz intensity evolution in Fig. 7-3. This direct observation of an elliptical polarization trajectory indicates that the THz radiation from a filament is not partially polarized. The latter would have no repetition in the relative phase difference between two perpendicular components as the wave propagates. The fact that the experimental polarization trajectory is not a perfect ellipse might be due to the broad bandwidth of near single-cycle THz pulse and energy fluctuation of the laser.

Figure 7-5 shows the polarization evolution of the THz pulses from a filament when the pump polarization is oriented at different angles (ϕ). As ϕ is rotated counter-clockwise when looking into the beam [Fig. 7-5(b)], the azimuth of the major axes of the THz ellipse rotates in the same direction (counter-clockwise) by the same angle [Fig. 7-5(a)-(d)]. When ϕ is changed by 180°, the azimuth of the major axes of the THz ellipse rotates by 180° accordingly [Fig. 7-5(b) and Fig. 7-5(e)].

These results indicate that there is another generation mechanism for THz emission from a laser filament besides transition-Cherenkov radiation in a conic direction with radial polarization which has no preference along any radial direction. The origin of elliptically polarized THz pulses could be through four-wave optical rectification or second-order optical rectification inside the filament zone where inversion symmetry is broken by the filamenting pulses [26, 27]. In the case of four-wave optical rectification, the THz wave could be generated in air through

$$\Omega_{THz} = \omega_1 + \omega_2 - \omega_3, \tag{7-2}$$

where $\omega_1 + \omega_2 \cong \omega_3$. This relation can be satisfied because the laser spectrum could be

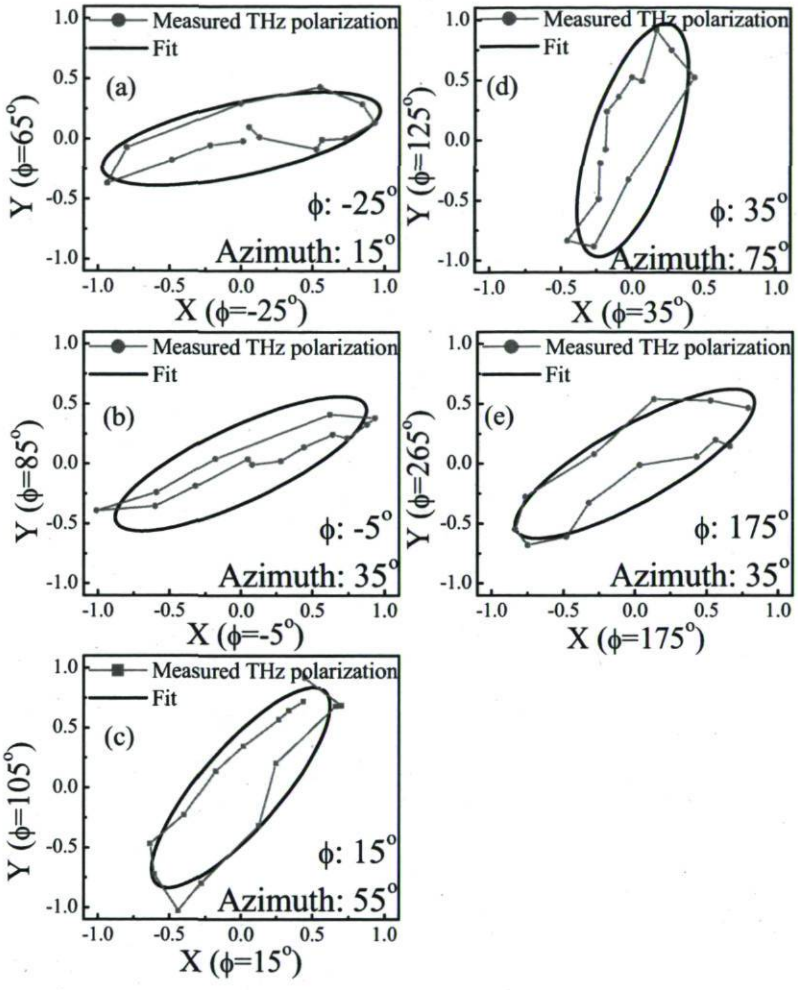

Figure 7-5: Polarization of the THz pulses measured at pump orientation ϕ at (a) -25°, (b) -5°, (c) 15°, (d) 35° and (e) 175°.

octave-spanned from ultraviolet to infrared in the course of filamentation. Hence, the THz waves with parallel-to-pump (defined as x direction) and orthogonal-to-pump (defined as y direction) polarizations can be obtain in air via

$$E_{THz,x} \propto \chi^{(3)}_{xxxx} E_{\omega_3} E^*_{\omega_1} E^*_{\omega_2} e^{i\Delta kL}, \tag{7-3}$$

$$E_{THz,y} \propto \chi^{(3)}_{yxxx} E_{\omega_3} E^*_{\omega_1} E^*_{\omega_2} e^{i\Delta kL}, \tag{7-4}$$

where $\Delta k = k_1 + k_2 - k_3$ describes the phase matching condition and L is the effective interaction length. As a result of symmetry-breaking in air, $\chi^{(3)}_{yxxx} \neq 0$ and the pump-induced nonlinear contributions to the refractive indices on two orthogonal polarization axes are different. Thus, the two THz components would travel at different phase velocities. This hypothesis could explain why the THz pulses generated inside the filament could be elliptically polarized.

We have known that due to spatial self-cleaning, the filament core features high quality spatial mode [5, 14, 16, 35, 96]. Therefore, the generated THz inside filament would in principle inherit this high spatial homogeneity just like other frequency conversion processes realized inside filament [14]. Compared to radially polarized THz pulses observed in Ref. [24], the discrepancy might be explained by the different spectral ranges that were studied. Besides, radially polarized THz pulses cannot be detected by our present setup because the amplitude of the electric field on the top of the THz conical emission is in opposite phase with the bottom of the THz conical emission, resulting in a zero signal at the focus located inside ZnTe crystal in our EOS technique.

7.4 Conclusion

In conclusion, elliptically polarized THz emission from a femtosecond laser filament was directly measured. The mechanism could be through four-wave optical rectification or second-order optical rectification inside the filament zone where inversion symmetry is broken by the filamenting pulses [26, 27]. This hypothesis is consistent with the experimental results but is not proven otherwise. The group velocity of the pump pulse

should play an important role in this nonlinear process as it is its envelope that determines the overlap of different frequencies. This work enhances the knowledge of THz radiations produced by a laser filament in air. It is of importance for application requiring standoff generation of THz pulses.

Chapter 8: THz emission from two-color filament*

8.1 Introduction

Similar to THz emission from one-color filament, filament-induced symmetry-breaking also affects the generation and polarization of THz emission from a two-color filament in air. Since the first demonstration by Cook and Hochstrasser [97], Terahertz (THz) generation in air by superposition of an intense fundamental (ω) pulse and its second-harmonic (2ω) pulse inside a plasma filament induced by the fundamental pulses has attracted great interest [98-105]. Compared with photo-excitation of semiconductors [106] or optical rectification in second-order nonlinear crystal [107], this technique can be performed at higher laser intensity. The attainable peak THz electric field is enhanced by more than one order than that emitted from a one-color filament [100]. A THz pulse with high-energy (>5 μJ) and super-broadband spectrum (~75 THz) has been reported with this technique [105].

The polarization of the THz pulse from a two-color (ω and 2ω) filament is still puzzling. Kress *et al.* [98] claimed that only the tensor component $\chi^{(3)}_{xxxx}$ of the nonlinear optical susceptibility was responsible for THz radiation, i.e., there is no THz radiation when the polarizations of ω and 2ω are orthogonal ($\chi^{(3)}_{yyxx}=0$). However, based on the same experimental configuration and detection technique, Bartel *et al.* [99] observed strong THz radiation polarized perpendicular to ω when the polarization of ω is perpendicular to 2ω, i.e., the $\chi^{(3)}_{yyxx}$ term dominates. There is an obvious discrepancy on THz generation between Ref. [98] and Ref. [99] when the polarizations of ω and 2ω are orthogonal. By separating the two beams (ω and 2ω) and independently controlling the polarization directions of ω and 2ω, Xie *et al.* [100] and Houard *et al.* [104] proved that THz radiation can be generated in both x and y planes ($\chi^{(3)}_{xyxx}$ and $\chi^{(3)}_{yyxx}$) when the

* The results presented in this chapter are based on the following article: Y. Chen, C. Marceau, F. Théberge, M. Châteauneuf, J. Dubois, and S. L. Chin, "Elliptically Polarized Terahertz Emission through Four-wave Mixing in a Two-color Filament in Air", *Opt. Commun.* **282**, 4283 (2009).

polarizations of ω and 2ω are orthogonal. Compared with $\chi^{(3)}_{xxxx}$, THz conversion efficiency from $\chi^{(3)}_{xyxx}$ and $\chi^{(3)}_{yyxx}$ is much lower, but not negligible. However, the coherence of the THz signals polarized at two orthogonal directions has not been proven yet.

In this chapter, we use the experimental configuration reported in Refs. [98, 99], sending a ω beam through a BBO crystal and then creating a two-color filament after the BBO crystal. We analyze the polarization of the THz emission from the two-color laser filament when ω and 2ω beams have orthogonal polarizations. We confirm that THz waves can indeed be obtained either parallel or orthogonal to the polarization of ω. Furthermore, we prove that the two polarization components of the THz wave are coherent and the combined electric field vector obeys an ellipse; i.e., the THz pulse is elliptically polarized.

8.2 Experimental setup

A 1 kHz, 800 nm, 1.15 mJ, 50 fs Ti-sapphire laser beam was focused by a lens with 50 cm focal length, creating a 2-cm-length filament in air. The diameter of the input beam before the focusing lens is 6 mm (FWHM). The filament diameter and the plasma density in the filament zone were measured experimentally to be 90 μm and 10^{16} cm^{-3}, respectively [59]. Due to a balance between Kerr focusing and plasma defocusing, the intensity is clamped around 4×10^{13} W/cm^2 in the filament zone [60]. The experimental setup was described in chapter 6 [50]. Here, we introduced a 100 μm-thick β-barium borate (BBO) crystal cut for type I second-harmonic generation between the focusing lens and the filament [Fig. 8-1(a)]. The orientation of the BBO crystal was set where the second-harmonic (2ω) was optimized and perpendicular to the ω beam. The polarization of the THz pulse emitting from the two-color filament was analyzed by a wire grid (THz analyzer, $E_{analyzer}$) which was located just after the Teflon plate. Meanwhile, the Z axis of the ZnTe crystal and the polarization of the probe were rotated in accordance with the rotation of the THz analyzer to minimize the orientation

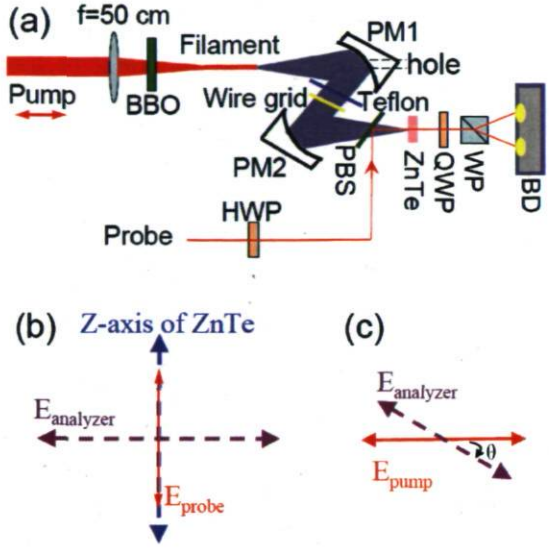

Figure 8-1: Schematic illustration of (a) the experimental setup, (b) orientation of maximum transmission of the THz analyzer ($E_{analyzer}$), *Z* axis [0,0,1] of the ZnTe crystal and probe polarization in the detection system and (c) definition of the angle θ. "WP" and "BD" are wollaston prism and balanced detector, respectively.

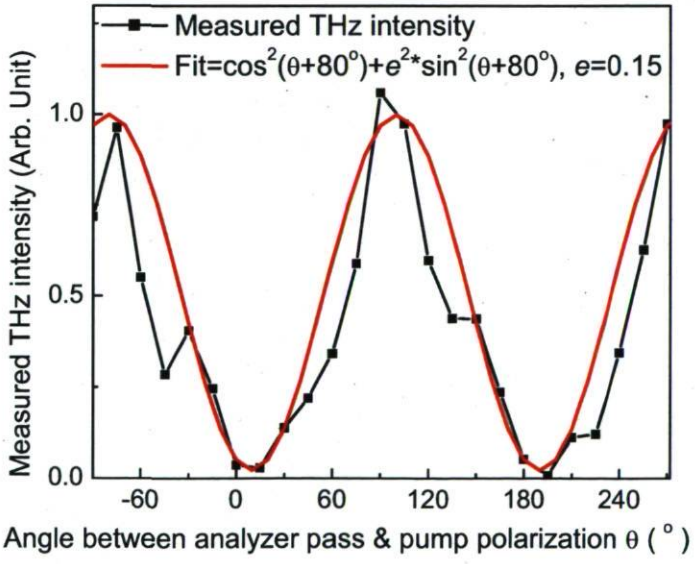

Figure 8-2: Measured (solid squares) and fitted (solid curve) intensity evolution of the THz electric field as a function of the angle θ.

dependence of THz pulse detection in ZnTe [Eq. A1-12 in Appendix 1][108], hence, the relative orientations of these three parts were always kept the same [as shown in Fig. 8-1(b)] to ensure a constant response in ZnTe crystal for THz components with any polarization. We refer to θ as the angle between the maximum transmission of the THz analyzer and the linearly polarized pump [as shown in Fig. 8-1(c)]. The origin (0°) was set when these two are parallel.

8.3 Experimental results

Figure 8-2 illustrates the intensity evolution of the THz electric field (solid squares) as a function of the angle θ. The pump energy is 1.15 mJ. Each point was obtained by squaring the peak-to-peak amplitude of the THz electric field measured at the given θ. The observed THz intensity varies periodically by more than one order of magnitude, but never reached zero. Typical THz electric fields measured around the minimum intensity (solid triangles: $\theta = 0°$) and the maximum intensity (solid circles: $\theta = 90°$) are shown in Fig. 8-3(a). This observation does not obey the prediction of Malus's law ($I = I_0 \cos^2\theta$) for a linearly polarized light passing through an analyzer, hence, indicating that the polarization of the THz pulse is not purely linear. The intensity curve is well fitted (solid curve) by using the following equation:

$$I = \cos^2(\theta + \theta_0) + e^2 \sin^2(\theta + \theta_0), \tag{8-1}$$

where $e = 0.15$ and $\theta_0 = 80°$.

Analytically, Eq. (8-1) is a combination of two orthogonal components. The THz pulse polarization can therefore be considered as the superposition of two decomposed linearly polarized components with orthogonal polarizations.

To confirm the polarization of the THz pulse, it is necessary to verify whether there is a repetition in the relative phase difference between two decomposed orthogonal components. This can be demonstrated by checking the electric field vector through

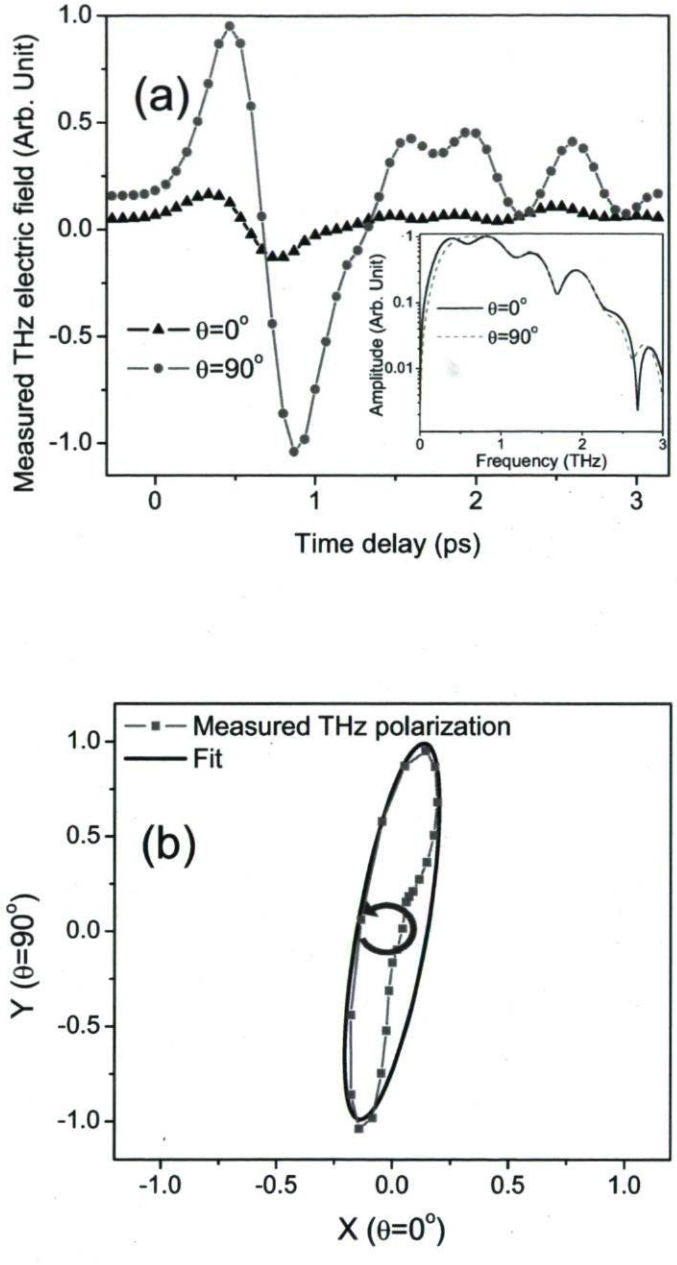

Figure 8-3: (a) Typical experimental THz electric fields obtained at two orthogonal directions (solid triangles: $\theta = 0°$ and solid circles: $\theta = 90°$) and the corresponding THz amplitude spectra (solid: $\theta = 0°$ and dash: $\theta = 90°$) in the inset. The pump energy is 1.15 mJ. (b) Measured (solid squares) and fitted (solid curve) THz polarization. The arrow indicates the rotating direction of the THz electric field vector.

recomposing the THz electric fields obtained at two orthogonal directions (i.e., $\theta = 0°$ and $\theta = 90°$). The THz electric field obtained at $\theta = 0°$ [solid triangles in Fig. 8-3(a)] was defined as X and the electric field at $\theta = 90°$ [solid circles in Fig. 8-3(a)] as Y. When they are plotted in an X-Y graph, a closed polarization trajectory is observed [solid squares in Fig. 8-3(b)]. Each solid square corresponds to the measured THz amplitudes of two orthogonal directions at one specified time delay and two successive solid squares are separated by 67 fs. The resulting THz electric field vector ends up rotating counter-clockwise as time advances, as indicated by the arrow in Fig. 8-3(b) when looking into the beam. This polarization trajectory is well fitted by an ellipse [solid curve in Fig. 8-3(b)] with an ellipticity ($e = E_{THz,MinorAxis} / E_{THz,MajorAxis}$) equal to 0.15. This value corroborates the ellipticity derived from the THz intensity evolution in Fig. 8-2. This direct observation of an elliptical polarization trajectory indicates that the THz radiation from a two-color filament is elliptically polarized, i.e., two decomposed linearly polarized components with orthogonal polarizations are coherent and propagate together with a fixed phase difference. The fact that the experimental polarization trajectory is not a perfect ellipse might be due to the broad bandwidth of near single-cycle THz pulse and energy fluctuation of the laser.

Since an elliptically polarized wave can be decomposed into an arbitrary set of mutually orthogonal component waves with their polarization planes perpendicular to each other and with a fixed phase difference, we expect to see a revival of an elliptical polarization trajectory by recomposing the THz electric field obtained at any set of two orthogonal directions (i.e., θ and $\theta + 90°$). Figure 8-4 shows the polarization evolution of the THz pulses from a two-color filament characterized by the THz analyzer oriented at different angles (θ). As the THz analyzer is rotated clockwise when looking into the beam, which is equivalent to rotating counter-clockwise the coordinate of the THz source, the azimuth of the major axes of the observed THz ellipse rotates counter-clockwise by the same angle [as shown in Fig. 8-4(a)-(f)].

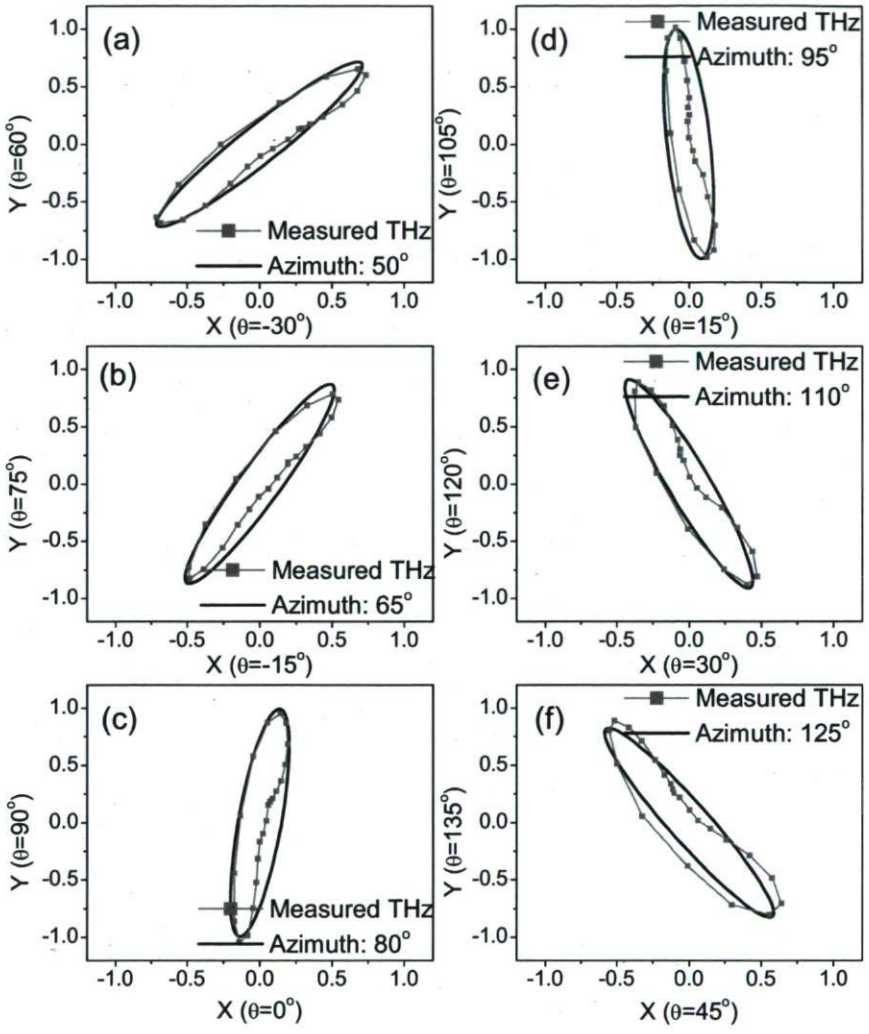

Figure 8-4: Polarization of the THz pulses measured at θ of (a) -30°, (b) -15°, (c) 0°, (d) 15°, (e) 30 ° and (f) 45°. The pump energy is 1.15 mJ.

8.4 Four-wave mixing model

There are currently two interpretations proposed to explain the THz generation from a two-color filament. The first interpretation is by a four-wave mixing model [97-100, 104]. The THz wave can be generated through $\chi^{(3)}E_{2\omega}\cdot E_{\omega}^{*}\cdot E_{\omega}^{*}\cdot e^{i\Delta kL}$, as Eq. (7-3) and Eq. (7-4). Optimum THz can be obtained when Δk is 0. The second interpretation is based on a transient photocurrent model [102]. A free electron drifting current can be generated by an asymmetric total laser field, thus emitting THz pulses. In order to clarify this confusion, Yizhu Zhang, Shengqi Xu, Lian Hui, Mingwei Wang, Weiwei Liu and Guoguang Mu from Nankai University, Tianjin, China, together with our lab, studied the THz emission from a two-color filament by rotating the BBO crystal through an angle α with respect to the propagation axis [109]. The experimental setup is almost the same as detailed in Fig. 8-1(a) except that the focusing lens was changed for one with 17.5 cm focal length. Two coordinates are used in the following discussion, which are defined in Fig. 8-5. In the lab coordinate (*X, Y*), the measured peak-to-peak

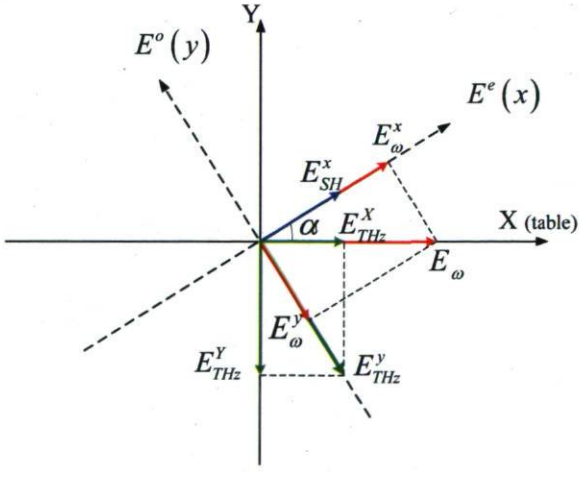

Figure 8-5: Coordinate Systems defined in this work. The observer looks into the laser beam. The *X* axis and *Y* axis are parallel and perpendicular to the pump beam polarization, respectively. The *x* axis and *y* axis are the extraordinary and ordinary refractive index axis of the BBO crystal, respectively. The polarization of the THz field is mainly parallel to the *y* axis.

amplitudes of E_X^{THz} (THz X component) and E_Y^{THz} (THz Y component) as a function of the BBO angle α are shown in Fig. 8-6(a) (open circles) and Fig. 8-6(b) (open triangles), respectively. The THz polarization, after being retrieved by recomposing two

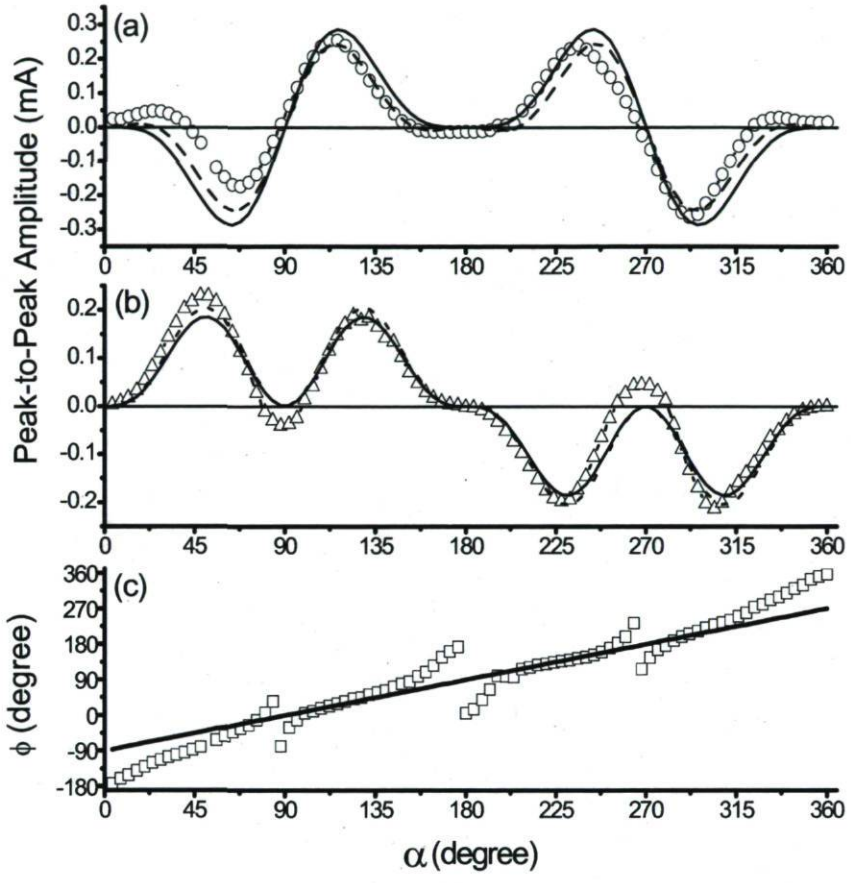

Figure 8-6: (a) Variation of E_{THz}^X (open circles) as a function of α. The solid line and the dashed line are calculated according to Eq. (5) and Eq. (6), respective. (b) The same as (a) for E_{THz}^Y. (c) The relationship between ϕ and α. Open squares: experimental data; Black line: linear fitting of $\phi = \alpha - 90°$.

orthogonal THz components, is found to be approximately linear (i.e. small ellipticity: ~0.05). One example is given in Fig. 8-7 for α = 140° [109]. α was defined as

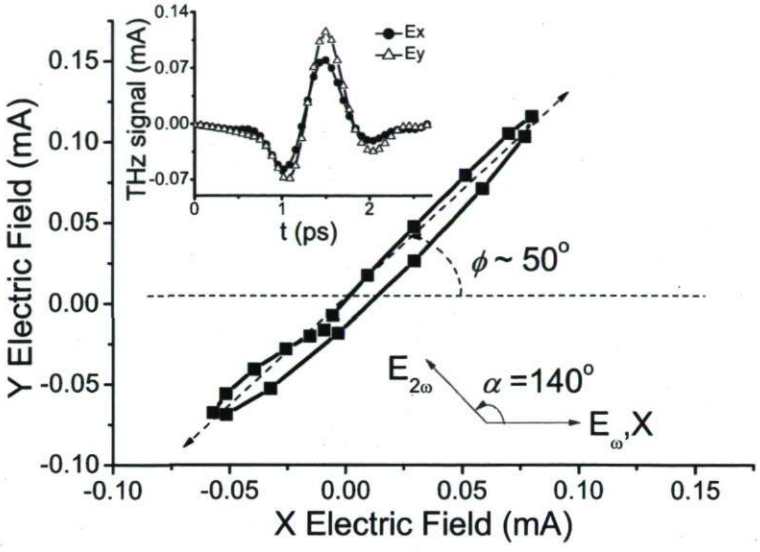

Figure 8-7: THz polarization trajectory obtained when α = 140° (solid squares). ϕ is the difference between the major axis of the THz polarization trajectory and X axis. Inset: electric field waveforms of E_{THz}^{X} (solid circles) and E_{THz}^{Y} (open triangles) for α = 140°, respectively.

the angle between the X axis and the extraordinary refractive index axis (e axis) of the BBO crystal in Fig. 8-5, i.e., α represents the polarization direction of the second harmonic. ϕ was defined as the difference between the major axis of the THz polarization trajectory and X axis in Fig. 8-7, i.e., ϕ represents the orientation of the major axis of the THz polarization trajectory with respect to the 800 nm pulse's (linear) polarization. From Fig. 8-7, one can obtain $\phi = \alpha - 90°$, hence, it can be deduced that the major axis of the THz polarization trajectory is perpendicular to the linear polarization of the second harmonic. Thus, in the following analysis, we assume that the THz polarization is linear. In the crystal coordinate (x, y), assuming 2ω polarized along the x axis, the four-wave mixing model can be denoted as:

$$E_{THz}^{y} \propto \sum_{kl} \chi_{yxkl}^{(3)} E_{SH}^{x} E_{\omega}^{k} E_{\omega}^{l} \quad (k, l = x, y), \tag{8-2}$$

where $\chi_{ijkl}^{(3)} = \chi_{ijkl}^{(3)}(\Omega_{THz}; 2\omega + \Omega_{THz}, -\omega, -\omega)$ is the third-order susceptibility, E_{ω} and E_{SH} are electric fields of ω and 2ω, respectively. In a centrosymmetric optical medium such as air, $\chi_{yxyy}^{(3)} = \chi_{yxxx}^{(3)} = 0$ and $\chi_{yxyx}^{(3)} = \chi_{yxxy}^{(3)}$, we finally get:

$$E_{THz}^{y} \propto \chi_{yxyx}^{(3)} E_{SH}^{x} E_{\omega}^{y} E_{\omega}^{x}. \tag{8-3}$$

According to the vectorial diagram described in Fig. 8-5, we substitute $E_{\omega}^{x} \propto E_{\omega} \cos\alpha$, $E_{\omega}^{y} \propto -E_{\omega} \sin\alpha$ and $E_{SH}^{x} \propto (E_{\omega} \sin\alpha)^2$ into Eq. (8-3), giving rise to:

$$E_{THz}^{y} = -aE_{\omega}^{4} \sin^3\alpha \cos\alpha, \tag{8-4}$$

where a is a proportionality factor which already takes into account $\chi_{yxyx}^{(3)}$. Further projection of E_{THz}^{y} onto X, Y axis leads to [109]:

$$\begin{aligned} E_{THz}^{X} &= E_{THz}^{y} \cos(\alpha - 90°) = -aE_{\omega}^{4} \sin^3\alpha \cos\alpha \cos(\alpha - 90°) \\ E_{THz}^{Y} &= E_{THz}^{y} \sin(\alpha - 90°) = -aE_{\omega}^{4} \sin^3\alpha \cos\alpha \sin(\alpha - 90°) \end{aligned} \tag{8-5}$$

Using Eq. (8-5), the measured THz X/Y amplitudes can be well fitted [solid lines in Fig. 8-6(a) and (b)]. Thus, it can be concluded that the THz emission from a two-color filament can be well interpreted by the four-wave mixing model. And the term $\chi_{yxyx}^{(3)}$ (equivalently, $\chi_{yxxy}^{(3)}$), plays a dominant role in this process. The slightly imperfect match between the experimental and simulated curves might be due to some other third-order terms, such as $\chi_{xxxx}^{(3)}$ and $\chi_{xxyy}^{(3)}$ etc., which could also contribute to the THz generation with relatively less efficiency. Compared with $\chi_{yxyx}^{(3)} / \chi_{yxxy}^{(3)}$, the contributions from these terms are minor. However, they become important when there is less or no

contribution from $\chi^{(3)}_{yxyx}$ / $\chi^{(3)}_{yxxy}$. Figure 8-6(c) shows the relationship between THz polarization direction ϕ and α (open squares). The overall tendency of the curve can be fitted by a solid line defined as $\phi = \alpha - 90^{\circ}$ which indicates the polarization of the THz is perpendicular to that of the second harmonic. But non-negligible discrepancy is observed when α approaches 0°, 90°, 180° and 270° from below or above. From Fig. 8-6(a) and (b), we learn that the THz signals obtained in these four regions are relatively low, however, still significantly higher than the detection background level. The discrepancy might be explained in the following. When α approaches 90° and 270° from below or above, the polarizations of the fundamental beam and the second harmonic beam become more and more orthogonal; i.e. $\alpha \rightarrow \pi/2$ or $E^x_\omega \propto E_\omega \cos\alpha \rightarrow 0$. The four-wave mixing associated with $\chi^{(3)}_{yxyx}$ become less important. Other terms, such as $\chi^{(3)}_{xxyy}$, start to play a role in the generation of THz pulses whose polarization is parallel to 2ω's polarization. On the other hand, when α approaches 0° and 180° from above or below, $E^y_\omega \propto -E_\omega \sin\alpha \rightarrow 0$. It means that the term associated with $\chi^{(3)}_{yxyx}$ becomes less important while $\chi^{(3)}_{xxxx}$ becomes more important to generate a THz field with polarization parallel to the 2ω field.

8.5 Discussion

The work by Zhang *et al.* from Nankai University in Ref. [109] with contribution from our lab, has proven that the four-wave mixing model can well interpret the THz results from a two-color filament. The $\chi^{(3)}_{xyxy}$ (or equivalently $\chi^{(3)}_{xyyx}$) term is shown to have played a dominant role in this process. The experimental results presented in Fig. 8-2, Fig. 8-3 and Fig. 8-4 were obtained when second harmonic was optimized with a type-I BBO crystal, i.e., the polarization directions of fundamental (ω) and second harmonic (2ω) are perpendicular to each other. This corresponds to $\alpha = 90^{\circ}/270^{\circ}$ in Fig. 8-6 where there is no contribution from the dominant term $\chi^{(3)}_{yxyx}$. In this particular case, the THz wave polarized along x axis and y axis respectively can be noted as:

$$E_{THz}^{x} = \chi_{xxyy}^{(3)} E_{SH}^{x} E_{\omega}^{y} E_{\omega}^{y} \cos(\varphi), \tag{8-6}$$

$$E_{THz}^{y} = \chi_{yxyy}^{(3)} E_{SH}^{x} E_{\omega}^{y} E_{\omega}^{y} \cos(\varphi), \tag{8-7}$$

where φ is the relative phase difference between ω and 2ω beams, i.e., $2\phi_{\omega} - \phi_{2\omega}$. $\chi_{yxyy}^{(3)}$ should be zero in a centrosymmetric medium. However, the medium of air is polarized by the intense pump pulses (ω) in the filament zone, hence, its inversion symmetry is broken [26, 27], and the $\chi_{yxyy}^{(3)}$ would contribute to the THz generation. Experimentally, this term ($\chi_{yxyy}^{(3)}$) has been proven to be non-vanishing by Xie *et al.* [100] and Houard *et al.* [104] by controlling independently the polarizations of ω and 2ω. In addition, filament-induced birefringence leads to phase delay between E_{THz}^{x} and E_{THz}^{y} [105]. As a consequence, an elliptically polarized THz pulse is obtained at the output of a two-color filament.

Figure 8-8 shows the evolution of the THz polarizations by changing the pump energy when the pump and the second harmonic are orthogonally polarized. With the increase of the pump energy, the intensity of the second harmonic gets higher, but that of the fundamental stays almost constant due to intensity clamping in the filament [60, 61]. As a result, a longer filament is obtained at an increased pump energy, i.e., the symmetry-broken area getting longer. Figure 8-8 indicates that the reconstructed THz polarization trajectories always stay elliptical with pump energy increased up to 1.6 mJ. The ellipticity and orientation of the THz polarization ellipse change at each pump energy, which is due to the combined effects from intensity change of the second harmonic, change of accumulated phase delay between E_{THz}^{x} and E_{THz}^{y} (derived from variation in the filament length), and change of the relative phase difference (φ) between ω and 2ω (derived from heat problem in the BBO crystal).

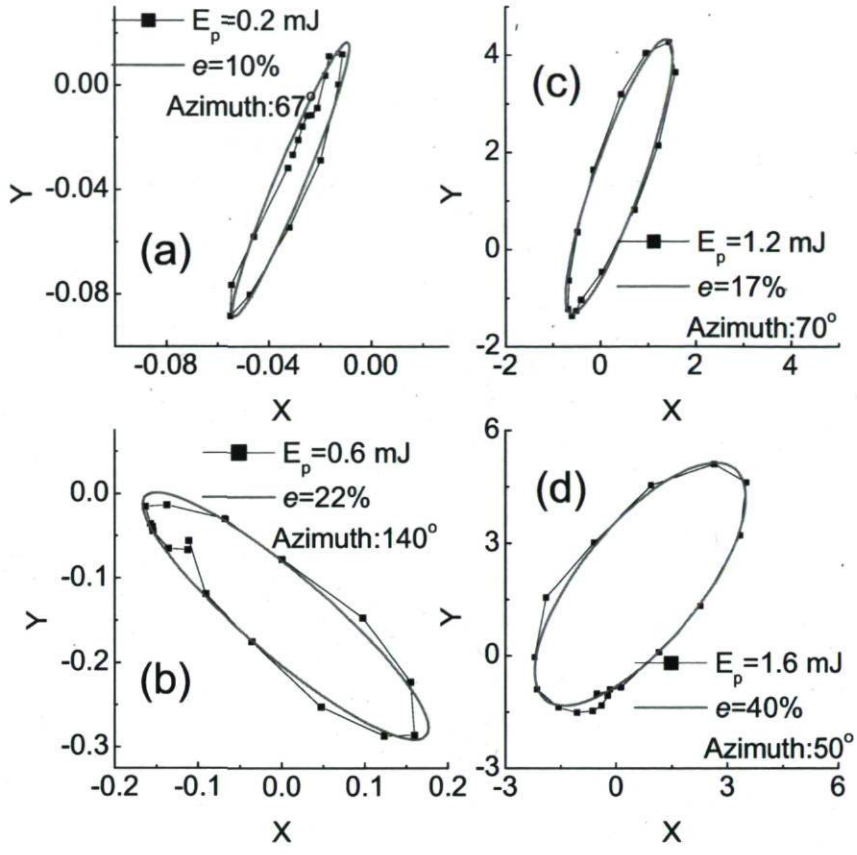

Figure 8-8: Polarization of the THz pulses with pump energy of (a) 0.2 mJ, (b) 0.6 mJ, (c) 1.2 mJ, (d) 1.6 mJ. The pump and the second harmonic are orthogonally polarized.

8.6 Conclusion

Through systemic study by Zhang *et al.* from Nankai University in Ref. [109], it is well proven that the dominant process in generating THz emission from a two-color filament can be interpreted by the four-wave mixing model. The cross terms of the third-order susceptibility tensor $\chi^{(3)}_{xyxy}$ (or equivalently $\chi^{(3)}_{xyyx}$) term are shown to have played a

dominant role in this process. In the first part of this chapter, we studied a specific case (experimental results presented in Fig. 8-2, Fig. 8-3, Fig. 8-4 and Fig. 8-8) where there is no contribution from $\chi^{(3)}_{xyxy}$ or $\chi^{(3)}_{xyyx}$ term, i. e., $\alpha = 90^{o}/270^{o}$ in Fig. 8-6. In this case, we demonstrated elliptically polarized THz emission from a two-color femtosecond laser filament by directly measuring the polarization trajectory of the THz electric field vector. $\chi^{(3)}_{yxyy}$ and $\chi^{(3)}_{xxyy}$ terms are responsible for THz generation on two orthogonal directions. However, the transient photocurrent model could not be safely ruled out so far. Further study has to be carried out to clarify this point.

Chapter 9: THz emission from DC-biased filament*

9.1 Introduction

Compared with THz emission from two-color filament, THz radiation from one-color filament seems more attractive not because it is free from phase sensitive adjustment or precise alignment, but it can be generated close to the remote sample, overcoming the limitation of the strong absorption of THz by water vapor in air [4, 5, 24, 50, 94]. The drawback of THz emission from one-color filament is that the conversion efficiency is relatively low (about 10^{-9}) [110, 111]. It has been proven that the THz energy radiated from a filament can be enhanced by several orders of magnitude by applying a transverse external electric field to the filament in air [25, 112, 113]. The polarization of this enhanced THz signal was found to be collinear relatively to the external electric field [25].

In this chapter, by analyzing the polarization of THz emission from a DC-biased filament with EOS method, we found that the original elliptically polarized THz source from a single filament is not affected by applying an external electric field to the filament. Therefore, the THz radiation from a DC-biased filament can be regarded as a sum of elliptically polarized THz emission (from a single filament) and linearly polarized THz emission (induced by applying an external electric field to the filament), where only the second one can be amplified by the increase of the external electric field.

9.2 Experimental setup

In our experiment, a 1 kHz, 800 nm, 50 fs (slightly negatively chirped) Ti-sapphire laser beam was focused by a convex lens with 50 cm focal length, creating a 4-cm-length filament in air. The THz radiation from the filament was collected by a parabolic mirror

---

* The results presented in this chapter are based on the following article: Y. Chen, T. Wang, C. Marceau, F. Théberge, M. Châteauneuf, J. Dubois, O. Kosareva, and S. L. Chin, "Characterization of THz emission from a DC-biased filament in air", *Appl. Phys. Lett.* **95**, 101101 (2009).

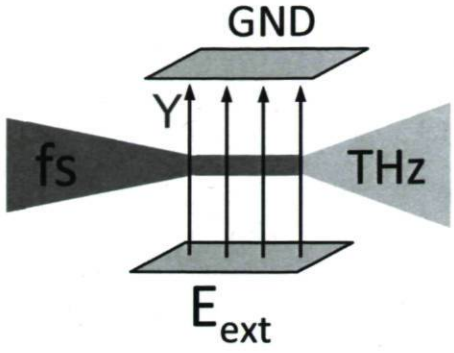

Figure 9-1: Schematic experimental setup.

in the forward direction of the filament and measured by the EOS method, which was detailed in Fig. 7-1. The thickness of the ZnTe crystal is 0.5 mm. The filament was sandwiched by two parallel copper plates separated by a 1 cm gap, as shown in Fig. 9-1. The size of each copper plate was 8 cm × 8 cm and the filament direction was along the central part parallel to one side of the plates. The voltage applied to the plates could be varied from 0 kV to 5 kV. The external electric field was vertically oriented, defined as *Y* axis in the lab coordinate.

9.3 Results and discussions

Figure 9-2 shows the polarizations of THz emission from a filament with an external electric field varying from 0 to 5 kV/cm. The pump energy was 1.6 mJ, vertically polarized. The THz polarizations were obtained by composing the THz electric fields measured in two orthogonal directions by EOS [50]. Without external electric field, an elliptical THz polarization trajectory was observed in Fig. 9-2(a). It could originate from the nonlinear birefringence of neutral molecules induced in the filament [50, 94]. In the presence of the external electric field, the THz emission changed its polarization trajectory with the increase of the applied electric field [Fig. 9-2(b)-(d)]. When the THz electric fields obtained with external electric field were subtracted by the corresponding ones obtained without external electric field [Fig. 9-2(a)], the recomposed THz

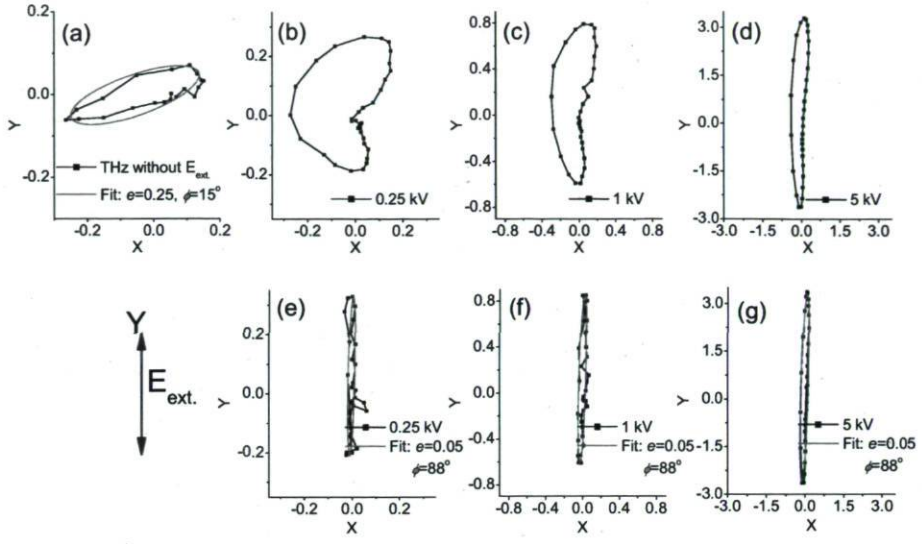

Figure 9-2: Polarization of THz emission from a filament with a DC field of (a) 0 kV/cm, (b) 0.25 kV/cm, (c) 1 kV/cm and (d) 5 kV/cm. THz polarizations in (e), (f), (g) were obtained at 0.25 kV/cm, 1 kV/cm and 5 kV/cm by subtracting the waveforms without DC field, respectively.

polarization trajectories were surprisingly uniform: linearly polarized along the orientation of the external electric field, as shown in Fig. 9-2(e)-(g). Note that the ratio of the intensity corresponding to the width and length of the THz ellipses $\left|E_{\min}^{THz} / E_{\max}^{THz}\right|^2$ is around 1:400 for all voltages. The imperfect DC field distribution and the fringe effect at the periphery of the copper plates could have contributed to the residual ellipticity. We could thus claim that in the ideal case, the DC field would generate a linearly polarized THz field parallel to the external field. The difference of 2° between the linear polarization trajectory and the *Y* axis is due to imperfect alignment between the external electric field and the *Y* axis of the THz component defined by the orientation of the wire grid. When the pump polarization was rotated by 90°, the THz polarization ellipse from the filament without external electric field rotated accordingly

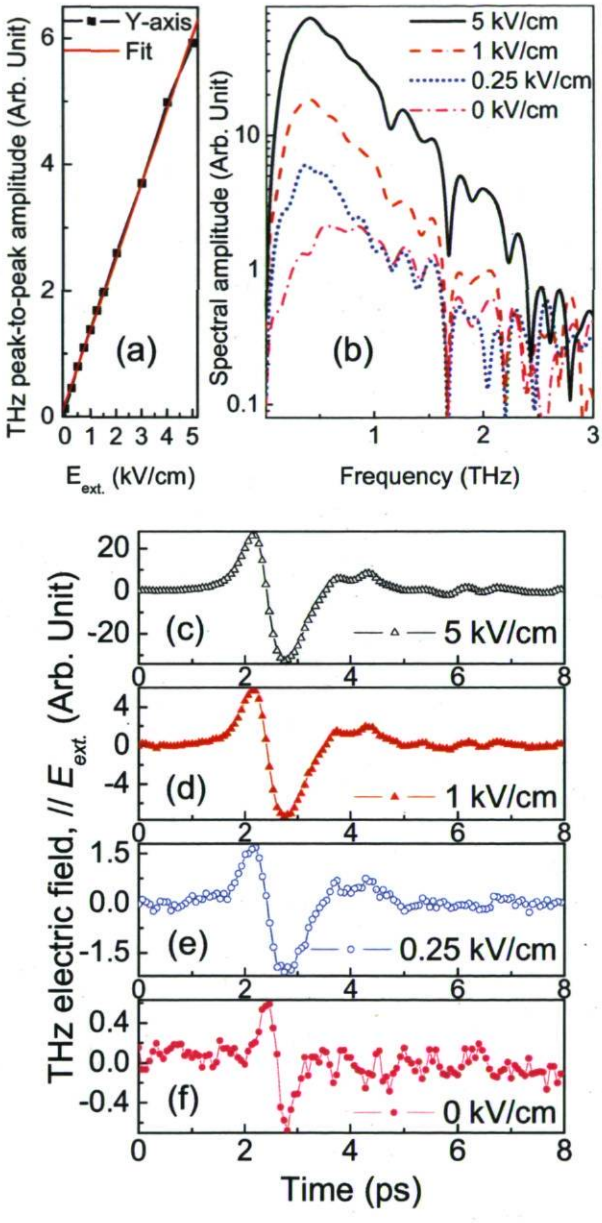

Figure 9-3: (a) Peak-to-peak amplitude of THz *Y* component as a function of external electric field. (b) THz spectral amplitudes obtained by Fourier transforms with $E_{ext.}$ of 0 kV/cm (dash-dot line), 0.25 kV/cm (dot line), 1 kV/cm (dash line) and 5 kV/cm (solid line). THz waveforms (*Y* axis) obtained with $E_{ext.}$ of (c) 5 kV/cm, (d) 1 kV/cm, (e) 0.25 kV/cm and (f) 0 kV/cm. The pump was 1.6 mJ.

[50]. However, the orientation and the profile of the linear THz polarization trajectory stayed parallel to the orientation of the external electric field (Y axis). This newly-generated linearly polarized THz source originating from the DC-biased filament has been well interpreted by Houard *et al.* in Ref. [25]. The external electric field separates the electrons and atoms in the plasma filament, which results in a transverse current responsible for THz emission with polarization parallel to the direction of the applied external electric field.

Figure 9-3(a) shows a linear dependence of the THz amplitude along the Y axis as a function of the external electric field. This relation obeys the prediction of the model in Ref. [25]: the total emitted THz energy $W \propto E_s^2$ where E_s is the external electric field. Thus the amplitude of the THz signal is proportional to the external electric field. An offset at zero bias corresponds to the THz signal obtained without DC-bias. We observed that the THz signal along the Y axis increased by 50 times with an external electric field of 5 kV/cm. Figure 9-3(b) presents the Fourier spectra of the THz emission from the filament with external electric field varying from 0 kV/cm to 5 kV/cm. The corresponding THz waveforms are shown in Fig. 9-3(c)-(f). The spectrum shifts to low frequencies in the presence of the external electric field, i.e., the temporal shape of an optical cycle is getting longer [Fig. 9-3(c)-(e)] than that without external electric field [Fig. 9-3(f)]. This corroborates that the elliptically polarized THz (from filament only) and the linearly polarized THz (induced by external electric field) are generated independently. Consequently, one can obtain the electric field of the linear source by subtracting that of the elliptical one from the total electric field. The peak frequencies of the Fourier spectra stay at 0.39 THz with the increase of the DC-bias, as shown in Fig 9-3(b). This maximum corresponds to the plasma frequency ($\omega_{pe} = \sqrt{e^2 n_e / m_e \varepsilon_0}$) which is independent of the intensity of the applied external electric field [25]. The estimated averaged plasma density ($n_e = m_e \varepsilon_0 \omega_{pe}^2 / e^2$), is around 1.9×10^{15} cm^{-3}, where the plasma frequency ω_{pe} is $2\pi\times0.39$ rad/s, the charge of the electron e is 1.6×10^{-19} C, the mass of the electron m_e is 9.11×10^{-31} kg and the permittivity of vacuum ε_0 is 8.854×10^{-12} Fm^{-1},

respectively.

Figure 9-4 shows the variation of the peak-to-peak amplitude (Y axis) of the THz emission from a DC-biased filament ($E_{ext.}$=5 kV/cm) as a function of the pump energy. A linear fitting indicates a threshold around 80 μJ which corresponds to the threshold intensity at which significant ionization occurs. Above this threshold, the amplitude increases linearly with the pump energy. Such linear increase is most probably due to the linear increase of the total plasma during the filamentation in air when the laser pulse is focused by a 50 cm focal length lens [114].

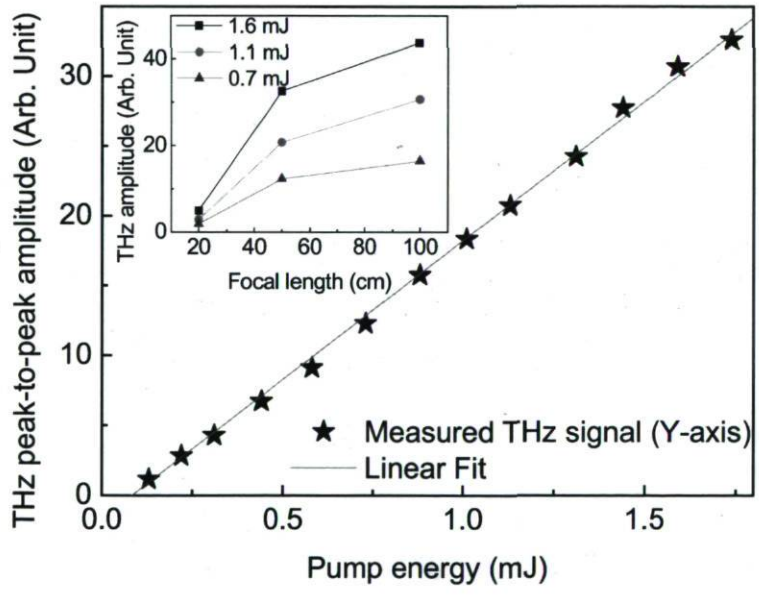

Figure 9-4: Peak-to-peak amplitude of the THz signal (Y axis) as a function of the pump energy with $E_{ext.}$=5 kV/cm: experimental data (stars) and a linear fit (line), with 50 cm focal length lens. Inset: Comparison of THz amplitudes (Y axis) from a DC-biased (5 kV/cm) filament formed by three focal length lens (20 cm, 50 cm and 100 cm) when the pump energy is 0.7 mJ (triangles), 1.1 mJ (circles) and 1.6 mJ (squares).

The peak electric field of the THz pulse can be estimated by measuring the modulation of the balanced photodiodes D_1 and D_2 in the EOS detection system [Appendix 1][115]:

$$\frac{\Delta I(\alpha,\varphi)}{I_p} = \frac{\omega n_0^3 E_{THz} \gamma_{41} L}{2c}(\cos\alpha \sin 2\varphi + 2\sin\alpha \cos 2\varphi)$$
$$\Delta I = D_1 - D_2 \quad , \qquad (9\text{-}1)$$
$$I_p = D_1 + D_2$$

where $n_0 = 2.85$ is the index of refraction of ZnTe at 800 nm, $\gamma_{41} = 4.04$ pm/V is the electro-optical coefficient of ZnTe [108, 116], $L = 0.5$ mm is the thickness of the ZnTe, ω is the angular frequency of the probe pulse, $\varphi = 0°$ is the angle between probe polarization and the (001) axis (or z axis) of the ZnTe crystal and $\alpha = 90°$ is the difference between the applied THz polarization and the (001) axis (or z axis) of the ZnTe crystal, respectively. At the pump energy of 1.7 mJ, a maximum modulation of $\Delta I / I_p = 1.02\%$ is observed. Thus, the maximum THz amplitude is estimated to be around 277 V/cm. The THz energy can be estimated from [115]:

$$W = \frac{\tau A \left| E_{THz} \right|^2}{2\eta_0}, \qquad (9\text{-}2)$$

where W is the THz energy, τ is the pulse width, A is the THz beam area at the focus measured by E-O sampling technique, E_{THz} is the THz amplitude and η_0 is the impedance of free space. Using Eq. (9-2), along with $\tau \approx 1$ ps, $A \approx \pi \times (0.06)^2$ cm^2, $\eta_0 \approx$ 376.73031 Ω and $E_{THz} \approx 277$ V/cm, the THz energy is calculated to be 1.15 pJ.

We also measured the THz amplitude (Y axis, $E_{ext.}$=5 kV/cm) as a function of focal lengths of various lenses (filament length) (inset of Fig. 9-4). At the pump energy of 1.6 mJ, the typical filament lengths are 1 cm, 4 cm and 10 cm for the lenses with focal length of 20 cm, 50 cm and 100 cm, respectively. The inset shows that an enhancement at least by a factor of 8 as the filament length increases from 1 cm to 10 cm with the same pump energy. According to the dependence of the THz spectral energy on the plasma length [25], for small emission angles (almost forwardly directed THz

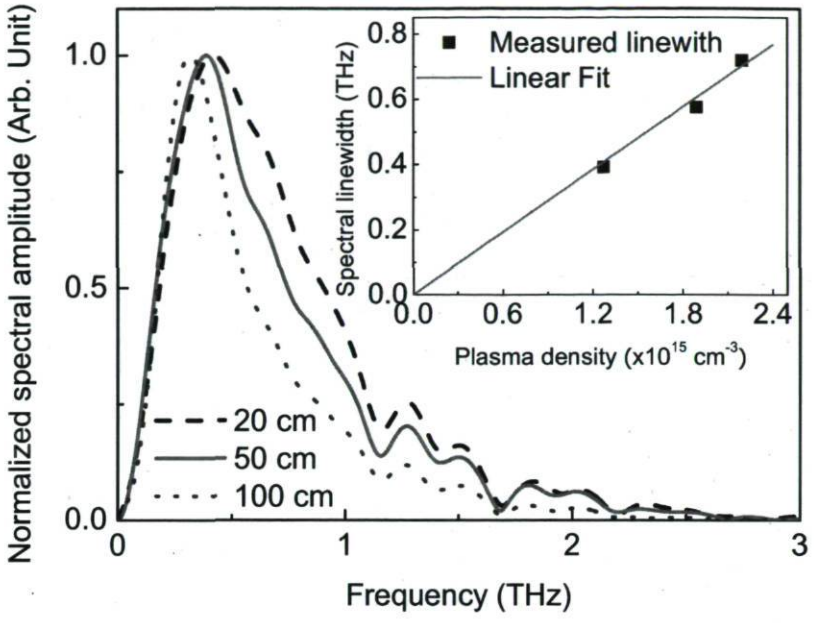

Figure 9-5: Normalized spectral amplitudes for linearly polarized THz emission from DC-biased filaments with 20 cm (dash line), 50 cm (solid line) and 100 cm (dot line) focal length lens. $E_{ext.}$=5 kV/cm. The pump is 1.6 mJ. Inset: Linear dependence between linewidth and plasma density.

radiation), THz amplitude should grow linearly with the filament length. Due to the limited length of our copper plates and collection efficiency of the parabolic mirror for long filament, the growth of the measured THz amplitude is slower than the linear one as seen in the inset of Fig. 9-4.

Figure 9-5 presents the spectral amplitudes of the (linearly polarized) THz emission from DC-biased (Y axis, $E_{ext.}$=5 kV/cm) filaments with varied focal conditions. We observed the peak frequency shifts from 0.42 THz (20 cm lens) to 0.32 THz (100 cm lens). The calculated plasma densities are 2.2×10^{15} cm^{-3} and 1.3×10^{15} cm^{-3}, respectively.

The spectral linewidths are 0.7 THz (20 cm), 0.6 THz (50 cm) and 0.4 THz (100 cm). A wider linewidth belongs to a shorter focal length lens (20 cm: dash line in Fig. 9-5) which produces a higher plasma density. The inset of Fig. 9-5 shows a linear dependence of the spectral linewidth as a function of the calculated plasma density for three focal length lenses. This matches well the theoretical model in Ref. [25] that the linewidth is proportional to the electron collision frequency, i.e., proportional to the plasma density.

We note that the plasma density derived from the spectral maxima of THz radiation is found to be lower than that obtained through 'local' fluorescence intensity measurement from the side of the filament [59]. We checked the absorption curve of the Teflon plate which is shown in Fig. 9-6 [117]. We found, below 3 THz (above 100 μm, frequency range in the Fig. 9-5), the averaged absorption is around 10%. The maximum variation from the averaged absorption is less than 7%. The absorption curve is almost flat from 0.38 THz (800 μm) to 0.75 THz (400 μm). We also checked the absorption curve of the

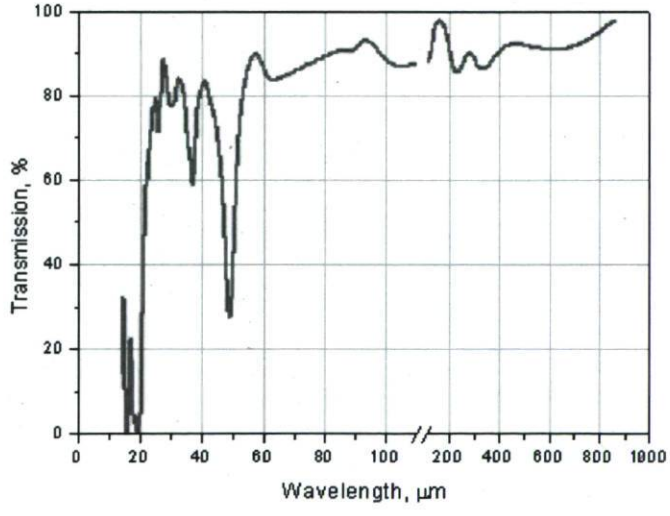

Figure 9-6: Transmission of Teflon film ~0.1 mm-thick.

ZnTe crystal in [Fig. A1-1 in Appendix 1][118]. Below 1 THz, the absorption curve is pretty flat, less than 10% absorption with a 0.5-mm-thick ZnTe. From 1 THz to 2.6 THz, the absorption is getting stronger with a maximum of 45% at 1.7 THz whereas the spectral amplitude in Fig. 9-5 is more than 1 order of magnitude lower than the peak amplitude. So the spectral amplitude above 1 THz is still much lower than the peak amplitude even the absorption is taken into account. Therefore, we believe the effect of the absorption of the ZnTe crystal and the Teflon plate can be neglected when considering the discrepancy on the plasma density. Thus the reason of the discrepancy is that the latter depends straightforwardly on the local number of electrons thus reflecting the peak density in the filament, or the density averaged over comparatively smaller detection volume [119]. In the present case, the THz emission from the whole filament was measured and represented an overall average plasma density.

9.4 Conclusion

In conclusion, we demonstrated that the total electric field of the THz emission from a DC-biased filament can be regarded as a sum of the one from an elliptically polarized THz source (generated by filament without external electric field) and the other one from a linearly polarized THz source (induced by applying an external electric field to the filament). Due to their independent origins, the two THz sources have different peak frequency. The linearly polarized THz source is polarized along the orientation of the external electric field. It can be amplified by increasing either the applied external electric field, the pump energy, or the filament length. We also proved the possibility of controlling the peak frequency and linewidth of the linearly polarized THz emission by manipulating the plasma density in the filament. This technique can be used to measure the plasma density of the filaments generated by different focusing lenses. This represents the average density of the filament plasma column. Due to strong absorption of ZnTe crystal at frequency higher than 4.5 THz [Figure A1-1 in Appendix 1], plasma density larger than 2.5×10^{17} cm^{-3} is beyond the detection range of this technique with a ZnTe crystal. Optical phonon frequency of a GaP crystal is 11 THz, higher than that of a

ZnTe crystal (5.3 THz) [99]. Thus GaP crystal has a comparatively broader transmission range. It has been proven that frequency up to 8 THz can be detected by EOS technique with a GaP crystal [99], i. e., plasma density up to $\sim 8\times10^{17}$ cm^{-3} can be measured by replacing the ZnTe crystal by a GaP crystal. However, the electro-optic coefficient of GaP crystal is lower than that of ZnTe crystal, which may make the measurements more difficult.

Chapter 10: Conclusion

In this thesis, we have investigated experimentally some nonlinear processes during the filamentation of powerful femtosecond laser pulses in air. A commercial Ti-sapphire laser system was used in these experiments.

It is experimentally proved that a filament can provide with an ionization channel (two ionizing sections: one with efficient ionization and the other weakly ionized) on the propagation axis with clamped intensity and constant diameter over a distance much longer than the Rayleigh range. During the filamentation in air, continuous self-frequency down shift was observed in the spectrum of the filament core. The spectrum shifts towards lower frequency as the filament length increases. Spectral shift of more than 130 nm was obtained with a 2-m-filament in air.

It is also experimentally shown that the refractive index of air is modified in the presence of a femtosecond laser filament due to rotational effect of the molecules in air. The refractive index in the direction with molecular alignment increases while that in the orthogonal direction decreases. As a consequence of competing with plasma defocusing effect, a filament can work as a polarization separator for a co-propagating probe pulse. Meanwhile, in the filament core, the centro-symmetry of air is broken. Thus the filament also works like a uni-axial crystal which is free from damage threshold. This unique property enriches the nonlinear processes during filamentation of femtosecond laser pulses. One example is that elliptically polarized terahertz emission was obtained in the forward direction of a one-color air-filament. Besides, in a two-color filament (fundamental and its second harmonic), the generated terahertz radiation, through four-wave mixing, was proved to be elliptically polarized when the fundamental and the second harmonic are orthogonally polarized. $\chi^{(3)}_{yxyy}$ ($\chi^{(3)}_{yxyy} = 0$ in centro-symmetric medium) and $\chi^{(3)}_{xxyy}$ terms are responsible for terahertz generation in two orthogonal directions, respectively. In this thesis, it is also clarified that the polarization of the terahertz radiation from a DC-biased air-filament is a sum of

elliptically polarized terahertz emission (from a single filament) and linearly polarized terahertz emission (induced by applying an external electric field to the filament). The first one is not affected by applying an external electric field. Only the second one can be amplified by the increase of the external electric field. A maximum terahertz amplitude of 277 V/cm (or maximum terahertz energy of 1.15 pJ) was obtained in the presence of a 5 kV/cm external electric field at an input energy of 1.7 mJ. The extraction efficiency (W_{THz} / W_{pump}) is around 7×10^{-10}.

This thesis presented some of the nonlinear processes occurring inside an air-filament. There are still quite a lot of interesting and challenging questions in the field of filamentation nonlinear optics. For example, how to enhance the intensity of the terahertz radiation from a filament, how to generate intense terahertz waves at a further distance, how to detect terahertz wave generated from a filament far away and how to realize sensitive detection of terahertz wave with more bandwidth, etc. Besides, a systematic study of terahertz generation from a one-color filament can be carried out by controlling the initial chirp, pulse duration and spectral distribution of the pump pulse. Moreover, it is expected to observe signals at other new frequencies, besides terahertz wave, through nonlinear processes inside the filament zone since the pump evolves to a white light pulse with a rich variety of spectral components.

Appendix: Electro-optic sampling detection

Electro-optic sampling (EOS) detection is a second-order nonlinear optical process in which an applied electric field (THz wave) induces a refractive index change in an electro-optic material. This refractive index change leads to a change in the optical polarization of the detection pulse which is co-propagating through the electro-optic material, proportional to the electric-field strength. The merit of the EOS method over bolometric detection is that the thermal background is well suppressed.

Electro-optic effect in ZnTe crystal

For electro-optic detection, ZnTe (Zinc telluride) crystal is often used because its refractive index in the far IR is comparable to the near-IR refractive index, resulting in relatively efficient THz detection. ZnTe is a cubic crystal with point group $\bar{4}3m$, which possesses the only nonzero coefficient of the electro-optic tensor γ_{41} [120]. The power absorption coefficient of ZnTe crystal is shown in Fig. A1-1 [118]. In Figure

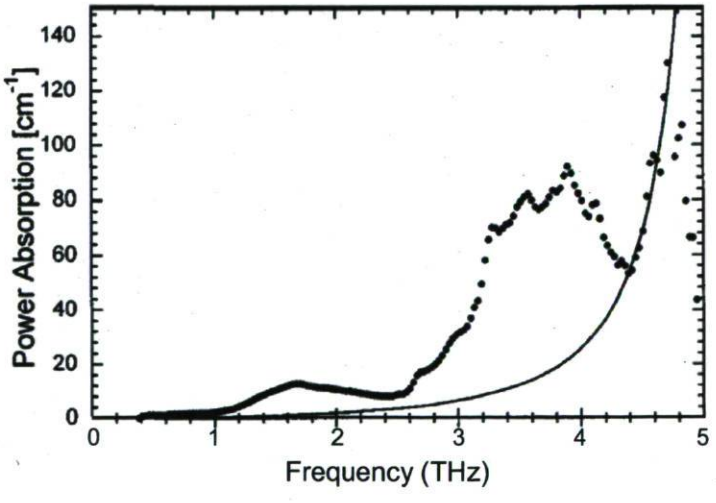

Figure A1-1: Measured (dots) and calculated (solid line) power absorption coefficient (cm^{-1}) for ZnTe crystal.

A1-2, x, y and z define the crystal coordinate, with the z axis corresponding to the (001) crystal axis, the refractive-index ellipsoid is given by [108]

$$\frac{x^2+y^2+z^2}{{n_0}^2}+\sqrt{2}\gamma_{41}E_{THz}\sin\alpha yz-\sqrt{2}\gamma_{41}E_{THz}\sin\alpha zx+2\gamma_{41}E_{THz}\cos\alpha xy=1, \qquad \text{(A1-1)}$$

where E_{THz} is the applied THz field, n_0 is the unperturbed refractive index and α is the angle between the applied THz electric field and the z axis of the ZnTe crystal, respectively. The consequence of the cross terms (yz, zx and xy) in Eq. (A1-1) is that the main axes of the refractive-index ellipsoid are not aligned with the axes of the crystal coordinate. To align the index ellipsoid with the new coordinate axes, a first transformation of a rotation of 45° around the z axis is made

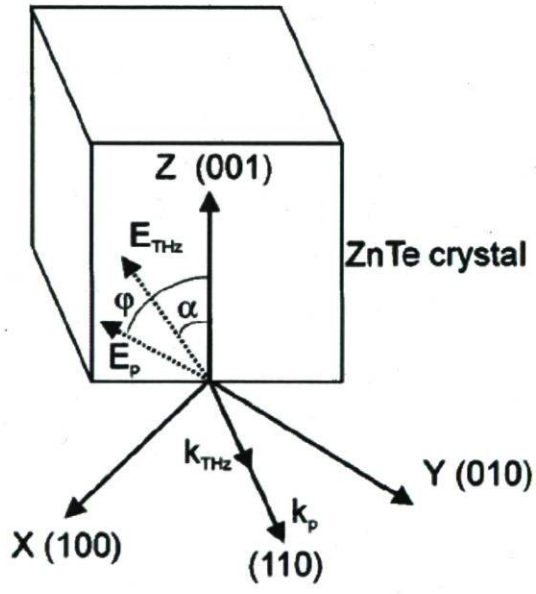

Figure A1-2: Definition of the optical axis of the ZnTe crystal. E_p and E_{THz} are the polarizations of the probe beam and the THz beam; φ is the angle between (001) axis of the ZnTe crystal and the polarization direction of the probe beam and α is the angle between (001) axis of the ZnTe crystal and the polarization direction of the THz beam; k_p and k_{THz} indicate the propagation direction of the probe beam and the THz beam.

$$\begin{aligned} x &= \frac{1}{2}\sqrt{2}x' - \frac{1}{2}\sqrt{2}y' \\ y &= \frac{1}{2}\sqrt{2}x' + \frac{1}{2}\sqrt{2}y', \\ z &= z' \end{aligned} \tag{A1-2}$$

The corresponding index ellipsoid in the coordinate (x', y', z') is

$$x'^2\left(\frac{1}{n_0^2} + \frac{E_{THz}\cos\alpha}{\sqrt{2}}\gamma_{41}\right) + y'^2\left(\frac{1}{n_0^2} - E_{THz}\gamma_{41}\cos\alpha\right) + \frac{z'^2}{n_0^2} + 2E_{THz}\gamma_{41}\sin\alpha y'z' = 1, \tag{A1-3}$$

In order to remove the remaining cross term $y'z'$ in Eq. (A1-3), a second transformation of a rotation of a angle θ around the x' axis is made

$$\begin{aligned} x' &= x'' \\ y' &= y''\cos\theta - z''\sin\theta \ , \\ z' &= y''\sin\theta + z''\cos\theta \end{aligned} \tag{A1-4}$$

Consequently, the corresponding index ellipsoid is

$$\begin{aligned} &x''^2\left(\frac{1}{n_0^2} + E_{Thz}\gamma_{41}\cos\alpha\right) \\ &+y''^2\left\{\frac{1}{n_0^2} - E_{THz}\gamma_{41}\left[\cos\alpha\sin^2\theta + \cos\left(\alpha + 2\theta\right)\right]\right\} \\ &+z''^2\left\{\frac{1}{n_0^2} - E_{THz}\gamma_{41}\left[\cos\alpha\sin^2\theta - \cos\left(\alpha + 2\theta\right)\right]\right\} = 1 \end{aligned} \ , \tag{A1-5}$$

where $2\theta = -\arctan(2\tan\alpha) - n\pi$, (A1-6)

$$\left(n - \frac{1}{2}\right)\pi \le \alpha < \left(n + \frac{1}{2}\right)\pi, \qquad n = 0,1,...$$

Eq. (A1-6) indicates that the rotation angle θ is related to the angle α, i.e., the difference between the applied THz polarization and the (001) axis of the ZnTe crystal. Using the

relation $\sqrt{1+x} \approx 1+\frac{x}{2}$ (x is a mathematical variable, not the coordinate axis). provided that x is small, the refractive indices deduced from Eq. (A1-5) for laser beam propagating along the x'' direction are

$$\begin{aligned} n_{y''}(\alpha) &\approx n_0 + \frac{n_0^3}{2} E_{THz} \gamma_{41} \left[\cos\alpha \sin^2\theta + \cos(\alpha + 2\theta)\right] \\ n_{z''}(\alpha) &\approx n_0 + \frac{n_0^3}{2} E_{THz} \gamma_{41} \left[\cos\alpha \cos^2\theta - \cos(\alpha + 2\theta)\right] \end{aligned} \quad \text{(A1-7)}$$

So, the polarization components of the probe beam in y'' and z'' directions accumulate different optical phases, resulting in an elliptically polarized probe. The phase delay between two components after passing through the ZnTe crystal is

$$\delta = \frac{\omega}{c}\left[n_{y''}(\alpha) - n_{z''}(\alpha)\right]L. \quad \text{(A1-8)}$$

Lock-in amplifier

The lock-in amplifier was invented by Princeton University physicist Robert H. Dicke who founded the company Princeton Applied Research (PAR) to market the product [121]. Lock-in amplifiers are used to detect and measure very small AC signals. Accurate measurements may be made even when the small signal is masked by noise sources many thousands of times larger. In order that signals be recovered at low signal-to-noise ratios, it is essential that a strong, clean reference signal be available at the same frequency as the signal to be measured. This is often not the case in many experiments. However, this can be fulfilled by a chopper controller which provides a modulation to the signal to be measured by setting a chopper in the beam path of the signal. Meanwhile, the chopper controller sends this modulation frequency as a reference signal to the lock-in amplifier.

Lock-in amplifiers use mixing, through a frequency mixer, to convert the signal's phase and amplitude to a DC signal. In detail, a sinusoidal function of frequency v (Signal) is multiplied by another sinusoidal function of frequency μ (Reference):

$$V = V_{sig}\sin(2\pi\nu t + \phi_{sig}) \cdot V_{ref}\sin(2\pi\mu t + \phi_{ref})$$
$$= \frac{1}{2}V_{sig}V_{ref}\cos\left[2\pi(\nu-\mu)t + (\phi_{sig} - \phi_{ref})\right] - \quad \text{(A1-9)}$$
$$\frac{1}{2}V_{sig}V_{ref}\cos\left[2\pi(\nu+\mu)t + (\phi_{sig} + \phi_{ref})\right].$$

If the signal frequency ν is not equal to the reference frequency μ, the output V will have two AC signals. After being integrated over a time much longer than the period of the two functions, the result is zero. In the case when μ is equal to ν, and the two functions are in phase, the difference frequency component will be a DC signal. The average value is equal to half of the product of the amplitudes. When the output V passing through a low pass filter, AC signals (or noise signals at frequencies far from the reference) are attenuated. Only the signal at the reference frequency will result in a true DC output and be unaffected by the low pass filter. This is the signal we want to measure.

Noise at frequencies very close to the reference frequency will result in very low frequency AC outputs. Their attenuation depends upon the low pass filter bandwidth. Lock-in amplifiers have set the low pass filter bandwidth by setting the time constant [122]. The time constant is simply $1/2\pi f$ where f is the -3 dB frequency of the filter. A 1 second time constant referred to a filter whose -3 dB point occurred at 0.16 Hz. The notion of time constant arises from the fact that the actual output is supposed to be a DC signal. In fact, when there is noise at the input, there is noise on the output. By increasing the time constant, the output becomes more steady and easier to measure reliably. However, the time constant also reflects how slow the output responds.

Schematic setup of EOS detection

Figure A1-3 shows the schematic setup for EOS detection of the electric field of THz pulses [108]. A THz beam and a probe beam (ultrashort pulse, linearly polarized) co-propagate through a ZnTe crystal. When the THz beam is absent, the probe polarization is circular after passing through a quarter-wave plate. After a polarization

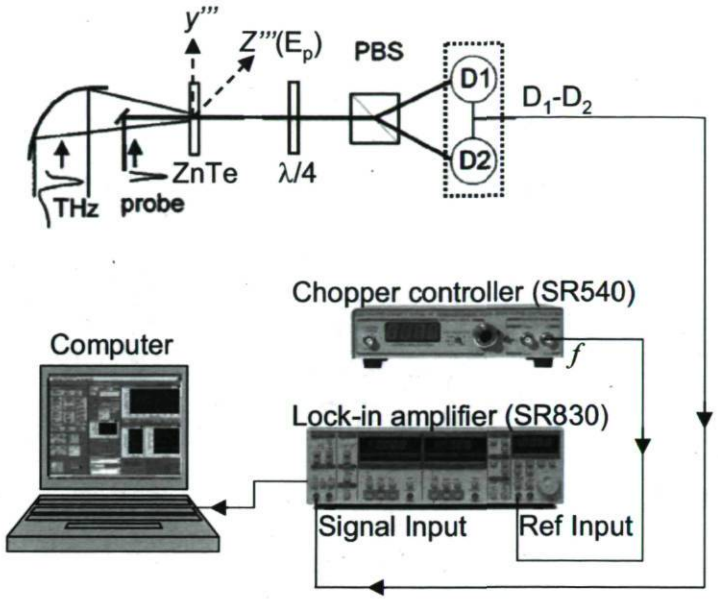

Figure A1-3: Schematic setup for EOS detection of the electric field of THz pulses.

beam splitter (PBS), the probe is evenly separated into two orthogonally polarized components, which give a zero signal to the following balanced detector (consisting of photodiodes D_1 and D_2). In the presence of a THz pulse, the refractive index change in the ZnTe crystal induced by the THz electric field affects the ellipticity of the circularly polarized probe pulse. In the coordinate (y''', z''') where the axis z''' is parallel to the linear polarization of the input probe, the probe beam is noted as $\begin{bmatrix} E_{z0'''} \\ E_{y0'''} \end{bmatrix} = \begin{bmatrix} E_p \\ 0 \end{bmatrix}$. After passing through the ZnTe crystal and the quarter-wave plate, the probe beam evolves to:

$$\begin{bmatrix} E_{z'''} \\ E_{y'''} \end{bmatrix} = \frac{\sqrt{2}}{2} \begin{bmatrix} 1 & -i \\ -i & 1 \end{bmatrix} \cos\frac{\delta}{2} \begin{bmatrix} 1 - i\tan\frac{\delta}{2}\cos 2(\varphi-\theta) & -i\tan\frac{\delta}{2}\sin 2(\varphi-\theta) \\ -i\tan\frac{\delta}{2}\sin 2(\varphi-\theta) & 1 + i\tan\frac{\delta}{2}\cos 2(\varphi-\theta) \end{bmatrix} \begin{bmatrix} E_p \\ 0 \end{bmatrix},$$

(A1-10)

where $\frac{\sqrt{2}}{2}\begin{bmatrix} 1 & -i \\ -i & 1 \end{bmatrix}$ and $\cos\frac{\delta}{2}\begin{bmatrix} 1-i\tan\frac{\delta}{2}\cos 2(\varphi-\theta) & -i\tan\frac{\delta}{2}\sin 2(\varphi-\theta) \\ -i\tan\frac{\delta}{2}\sin 2(\varphi-\theta) & 1+i\tan\frac{\delta}{2}\cos 2(\varphi-\theta) \end{bmatrix}$ are the Jones Matrix for the quarter-wave plate and the ZnTe crystal, respectively [85]. Here the ZnTe crystal is regarded as a retarder with phase delay δ which is defined in Eq. (A1-8). φ is the angle between (001) axis of the ZnTe crystal and the polarization direction of the probe beam (E_p), as shown in Fig. A1-2, and the angle θ is defined in Eq. (A1-4). Simplify Eq. (A1-10), one can obtain

$$\begin{bmatrix} E_{z'''} \\ E_{y'''} \end{bmatrix} = \frac{\sqrt{2}}{2}E_p\begin{bmatrix} \cos\frac{\delta}{2}-\sin\frac{\delta}{2}\sin 2(\varphi-\theta)-i\left(\sin\frac{\delta}{2}\right)\cos 2(\varphi-\theta) \\ -\sin\frac{\delta}{2}\cos 2(\varphi-\theta)-i\left(\cos\frac{\delta}{2}+\sin\frac{\delta}{2}\sin 2(\varphi-\theta)\right) \end{bmatrix}. \quad \text{(A1-11)}$$

Using Eq. (A1-8) and Eq. (A1-11), the intensity difference between the probe polarization components can be noted as [108]

$$\begin{aligned} &\Delta I(\alpha,\varphi) \\ &= \left|E_{y'''}\right|^2 - \left|E_{z'''}\right|^2 \\ &= {E_p}^2 \sin[2(\varphi-\theta)]\sin\left\{\frac{\omega}{c}[n_{y''}(\alpha)-n_{z''}(\alpha)]L\right\}, \\ &= I_p\frac{\omega n_0^3 E_{THz}\gamma_{41}L}{2c}(\cos\alpha\sin 2\varphi+2\sin\alpha\cos 2\varphi) \end{aligned} \quad \text{(A1-12)}$$

where L is the crystal length, $I_p=E_p^2$ is the probe intensity, c is the velocity of light in vacuum, ω is the angular frequency of the probe pulse, and φ is the angle between probe polarization and the (001) axis of the ZnTe crystal, respectively. Usually, we set φ = 0°, i. e., the orientation of the input probe pulse's polarization (E_p) is parallel to the (001) axis of the ZnTe crystal.

The intensity difference can be detected by the PBS and the balanced detector which measures the intensity difference between the two orthogonal polarization components of the probe and gives a signal that is directly proportional to the THz electric field, Eq.

(A1-12). This signal is quite small. It can be amplified by a Lock-in amplifier (Standford Research Systems, Model SR830 DSP Lock-in Amplifier) by sending the signal from the balanced detector to "Signal Input" on SR830 front panel, as indicated in Fig. A1-3. As discussed in the last section, lock-in amplifiers are used to detect very small AC signals. Thus a chopper is needed in the beam path of the THz pulses or in the beam path of the pump beam generating the THz pulses. A chopper (Standford Research Systems, Model SR540) controls the chopper frequency and sends the same frequency as a reference signal to the Lock-in amplifier, as shown in Fig. A1-3. The output signal from the lock-in amplifier can be recorded by a computer via a 24 pin IEEE-488 connector on the rear panel of the lock-in amplifier which allows a computer to control the lock-in amplifier through the IEEE-488 (GPIB) instrument bus. The pulse duration of the probe is around 50 fs and that of a THz pulse is ~2 ps. Thus, each measurement represents the amplitude of one slice of the THz pulse. By varying the delay between the THz pulse and the probe pulse, a complete THz electric field can be obtained. Figure A1-4 shows a typical complete waveform of a THz pulse obtained

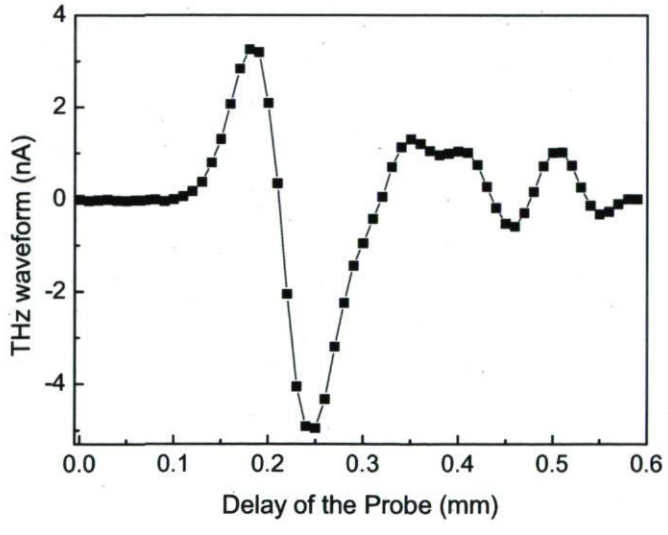

Figure A1-4: A typical complete waveform of a THz pulse obtained by scanning the delay of the Probe.

by scanning the delay of the probe pulse. Each square point in the curve was obtained at a specific delay of the probe, representing the amplitude of one slice of this THz pulse. The time constant for each square point is 100 ms. Two successive points were separated by 10 μm. The horizontal axis of Figure A1-4, delay of the probe in millimeter, can be converted to time scale by

$$t = \frac{2\times10^{-3}\times D}{c}, \tag{A1-13}$$

where c is the speed of light and D is the delay of the probe in millimeter. According to Eq. (A1-13), the pulse duration of the THz pulse in Figure A1-4 is ~2 ps.

Reference

1. M. Hercher, J. Opt. Soc. Am., 1964. **54**: p. 563.
2. D. Strickland, G.M., Opt. Commun., 1985. **56**: p. 219.
3. A. Braun, G.K., X. Liu, D. Du, J. Squier, G. Mourou, Opt. Lett., 1995. **20**: p. 73.
4. W. Liu, F.T., J.-F. Daigle, P. T. Simard, S. M. Sarifi, Y. Kamali, H. Xu, S. L. Chin, Appl. Phys. B, 2006. **85**: p. 55.
5. A. Couairon, A.M., Phys. Rep., 2007. **441**: p. 47.
6. Boyd, R.W., *Nonlinear Optics*. 2nd Edition ed. 2003, San Diego: Academic press. 356-357.
7. S. L. Chin, J. Korean Phys. Soc., 2006. **49**: p. 281.
8. A. L. Gaeta, Phys. Rev. Lett., 2000. **84**: p. 3582.
9. N. Akozbek, M.S., C.M. Bowden, S.L. Chin, Opt. Commun., 2001. **191**: p. 353.
10. A. Couairon, J.B., C. P. Hauri, W. Kornelis, F. W. Helbing, U. Keller, A. Mysyrowicz, J. Mod. Opt., 2006. **53**: p. 75.
11. C. P. Hauri, W.K., F. W. Helbing, A. Heinrich, A. Couairon, A. Mysyrowicz, J. Biegert, U. Keller, Appl. Phys. B, 2004. **79**: p. 673.
12. C. P. Hauri, A.G., P. Eckle, W. Kornelis, J. Biegert, U. Keller, Opt. Express, 2005. **13**: p. 7541.
13. X. Chen, Y.L., J. Liu, Y. Zhu, R. Li, Z. Xu, Opt. Commun., 2006. **259**: p. 331.
14. F. Theberge, N.A., W. Liu, A. Becker, S. L. Chin, Phys. Rev. Lett., 2006. **97**: p. 023904.
15. B. Prade, M.F., A. Mysyrowicz, A. Couairon, H. Buersing, B. Eberle, M. Krenz, D. Seiffer, O. Vasseur, Opt. Lett., 2006. **31**: p. 2601.
16. S. L. Chin, F.T., W. Liu, Appl. Phys. B, 2007. **86**: p. 477.
17. W. Liu, S.L.C., Phys. Rev. A, 2007. **76**: p. 013826.
18. I. G. Koprinkov, A.S., P. Wang, K. Midorikawa, Phys. Rev. Lett., 2000. **84**: p. 3847.
19. S. L. Chin, A.B., S. Petit, O. G. Kosareva, V. P. Kandidov, Journal of Nonlinear Optical Physics and Materials, 1999. **8**: p. 121-146.
20. W. Liu, S.P., A. Becker, N. Akozbek, C. M. Bowden, S. L. Chin, Opt. Commun., 2002. **202**: p. 189.
21. T. Fuji, T.H., T. Suzuki, Opt. Lett., 2007. **32**: p. 2481.
22. F. Theberge, Q.L., W. Liu, S.A. Hosseini, M. Sharifi, S.L. Chin, Appl. Phys. Lett., 2005. **87**: p. 081108.

23. L. Berge, S.S., G. Mejean, J. Kasparian, J. Yu, S. Frey, E. Salmon, J. P. Wolf, Phys. Rev. E, 2005. **71**: p. 016602.

24. C. D'Amico, A.H., M. Franco, B. Prade, A. Mysyrowicz, A. Couairon, V. T. Tikhonchuk, Phys. Rev. Lett., 2007. **98**: p. 235002.

25. A. Houard, Y.L., B. Prade, V. T. Tikhonchuk, A. Mysyrowicz, Phys. Rev. Lett., 2008. **100**: p. 255006.

26. P. Bejot, Y.P., L. Bonacina, J. Kasparian, M. Moret, J.-P. Wolf, Opt. Express, 2008. **16**: p. 7564.

27.Y. Chen, C.M., F. Theberge, M. Chateauneuf, J. Dubois and S. L. Chin, Opt. Lett., 2008. **33**: p. 2731.

28. C. Marceau, Y.C., F. Theberge, M. Chateauneuf, J. Dubois, S. L. Chin, Opt. Lett., 2009. **34**: p. 1417.

29. G. Mejean, J.K., J. Yu, S. Frey, E. Salmon, R. Ackermann, J. P. Wolf, L. Berge, S. Skupin, Appl. Phys. B, 2006. **82**: p. 341.

30. H. Xu, H.X., R. X. Li, Y. Cheng, Z. Z. Xu, S. L. Chin, Appl. Phys. Lett., 2008. **92**: p. 011111.

31. F. Theberge, N.A.z., W. Liu, J. F. Gravel, S. L. Chin, Opt. Commun., 2005. **245**: p. 399.

32. Z. Q. Hao, J.Z., Z. Zhang, T. T. Xi, Z. Y. Zheng, X. H. Yuan, Z. H. Wang, Acta Phys. Sinica, 2005. **54**: p. 3173.

33. F. Theberge, J.F., N. Akozbek, Y. Chen, A. Becker, S. L. Chin, Appl. Phys. B, 2007. **87**: p. 207.

34.J. Kasparian, R.S., D. Mondelain, S. Niedermeier, J. Yu, J. P. Wolf, Y. B. Andre, M. Franco, B. Prade, S. Tzortzakis, A. Mysyrowicz, M. Rodriguez, H. Wille, L. Woste, Opt. Lett., 2000. **25**: p. 1397.

35. L. Berge, S.S., R. Nuter, J. Kasparian, J.-P. Wolf, Rep. Prog. Phys., 2007. **70**: p. 1633.

36. T. Brabec, F.K., Rev. of Modern Phys., 2000. **72**: p. 545.

37. M. Hentschel, R.K., Ch. Spielmann, G. A. Reider, N. Milosevic, T. Brabec, P. Corkum, U. Heinzmann, M. Drescher, F. Krausz, Nature, 2001. **414**: p. 509.

38. S. Champeaux, L.B., Phys. Rev. E, 2003. **68**: p. 066603.

39. A. Couairon, M.F., A. Mysyrowicz, J. Biegert, U. Keller, Opt. Lett., 2005. **30**: p. 2657.

40. S.A Trushin, K.K., W. Fuss, E. Schmid, Opt. Lett., 2007. **32**: p. 2432.

41. A. Zair, A.G., F. Schapper, M. Holler, J. Biegert, L. Gallmann, A. Couairon, M. Franco, A. Mysyrowicz, U. Keller, Opt. Express, 2007. **15**: p. 5394.

42. L. Berge, S.S., Opt. Lett., 2008. **33**: p. 750.

43. L. Berge, S.S., Phys. Rev. Lett., 2008. **100**: p. 113902.

44. A. Mysyrowicz, A.C., U. Keller, New J. Phys., 2008. **10**: p. 025023.

45. K. R. Wilson, V.V.Y., J. Opt. Soc. Am. B, 1997. **14**: p. 444.

46. H. L. Xu, Y.K., C. Marceau, P. T. Simard, W. Liu, J. Bernhardt, G. Mejean, P. Mathieu, G. Roy, J.-R. Simard, S. L. Chin, Appl. Phys. Lett., 2007. **90**: p. 101106.

47. G. Mejean, J.K., E. Salmon, J. Yu, J. P. Wolf, R. Bourayou, R. Sauerbrey, M. Rodriguez, L. Woste, H. Lehmann, B. Stecklum, U. Laux, J. Eisloffel, A. Scholz, A. P. Hatzes, Appl. Phys. B, 2003. **77**: p. 357.

48. G. Faye, J.K., R. Sauerbrey, Appl. Phys. B, 2001. **73**: p. 157.

49. G. Mejean, J.K., J. Yu, S. Frey, E. Salmon, J. P. Wolf, Appl. Phys. B, 2004. **78**: p. 535.

50. Y. Chen, C.M., W. Liu, Z.-D. Sun, Y. Zhang, F. Theberge, M. Chateauneuf, J. Dubois, S.L. Chin, Appl. Phys. Lett., 2008. **93**: p. 231116.

51. Y. Chen, T.W., C. Marceau, F. Theberge, M. Chateauneuf, J. Dubois, O. Kosareva, S. L. Chin, Appl. Phys. Lett., 2009. **95**: p. 101101.

52. R. Y. Chiao, E.G., C. H. Townes, Phys. Rev. Lett., 1964. **13**: p. 479.

53. W. Liu, *Ultrashort pulse filamentation in transparent optical media*, in *Department of Physics*. 2006, University Laval: Quebec.

54. J. H. Marburger, Prog. Quantum Electron., 1975. **4**: p. 35.

55. M. M. T. Loy, Y.R.S., Phys. Rev. Lett., 1969. **22**: p. 994.

56. A. Brodeur, C.Y.C., F. A. Ilkov, S. L. Chin, O. G. Kosareva, V. P. Kandidov, Opt. Lett., 1997. **22**: p. 304.

57. S. L. Chin, W.L., F. Theberge, Q. Luo, S. A Hosseini, V. P. Kandidov, O. G. Kosareva, N. Akozbek, A. Becker, H. Schroeder, *Some Fundamental Concepts of Femtosecond Laser Filamentation*, in *Progress in Ultrafast Intense Laser Science III*. 2008. p. 243.

58. R.C. Weast, R.L.D., J.A. Melvin, H.B. William, *CRC Handbook of Chemistry and Physics*. 70 ed. 1990, Boca Raton, FL: CRC Press.

59. F. Theberge, W.L., P. T. Simard, A. Becker, S. L. Chin, Phys. Rev. E, 2006. **74**: p. 036406.

60. J. Kasparian, R.S., S. L. Chin, Appl. Phys. B, 2000. **71**: p. 877.

61. A. Becker, N.A., K. Vijayalakshmi, E. Oral, C. M. Bowden, S. L. Chin, Appl. Phys. B, 2001. **73**: p. 287.

62. R. W. Boyd, *Nonlinear Optics*. 2003, Academic press: San Diego. p. 356-357.

63. A. Talebpour, J.Y., S.L. Chin, Opt. Commun., 1999. **163**: p. 29.

64. O.G. Kosareva, V.P.K., A. Brodeur, C.Y. Chien, S.L. Chin, Opt. Lett., 1997. **22**: p. 1332.

65. S. Tzortzakis, B.P., M. Franco, A. Mysyrowicz, Opt. Commun., 2000. **181**: p. 123.

66.B. La Fontaine, F.V., Z. Jiang, C. Y. Chien, D. Comtois, A. Desparois, T. W. Johnston, J. -C. Kieffer, H. Pepin, and H. P. Mercure, Phys. Plasmas, 1999. **6**: p. 1615.

67. W. Liu, F.T., E. Arevalo, J. -F. Gravel, A. Becker, S. L. Chin, Opt. Lett., 2005. **30**: p. 2602.

68. S. L. Chin, S.A.H., W. Liu, Q. Luo, F. Theberge, N. Akozbek, A. Becker, V. P. Kandidov, O. G. Kosareva, H. Schroeder, Can. J. Phys., 2005. **83**: p. 863.

69. W. Liu, Q.L., F. Theberge, H. L. Xu, S. A. Hosseini, S. M. Sarifi, S. L. Chin, Appl. Phys. B, 2006. **82**: p. 373.

70. G. Mechain, A.C., Y.-B. Andre, C. D'Amico, M. Franco, B. Prade, S. Tzortzakis, A. Mysyrowicz, R. Sauerbrey, Appl. Phys. B, 2004. **79**: p. 379.

71. C. Ruiz, J.S.R., C. Mendez, V. Diaz, L. Plaja, I. Arias, L. Roso, Phys. Rev. Lett., 2005. **95**: p. 053905.

72.V. P. Kandidov, O.G.K., I. S. Golubtsov, W. Liu, A. Becker, N. Akozbek, C. M. Bowden, S. L. Chin, Appl. Phys. B, 2003. **77**: p. 149.

73. W. Liu, S.L.C., Opt. Express, 2005. **13**: p. 5750.

74. S. L. Chin, S.P., W. Liu, A. Iwasaki, M. -C. Nadeau, V. P. Kandidov, O. G. Kosareva, K. Y. Andrianov, Opt. Commun., 2002. **210**: p. 329.

75. S. Eisenmann, A.P., A. Zigler, Phys. Rev. Lett., 2007. **98**: p. 155002.

76. F. M. Mitschke, L.F.M., Opt. Lett., 1986. **11**: p. 659.

77. J. P. Gordon, Opt. Lett., 1986. **11**: p. 662.

78. X. Liu, C.X., W. H. Knox, J. K. Chandalia, B. J. Eggleton, S. G. Kosinski, R. S. Windeler, Opt. Lett., 2001. **26**: p. 358.

79. G. P. Agrawal, *Nonlinear Fiber Optics*. 2001, San Diego, Calif.: Academic.

80. E. T. J. Nibbering, G.G., M. A. Franco, B. S. Prade, A. Mysyrowicz, J. Opt. Soc. Am. B, 1997. **14**: p. 650.

81. A. C. Bernstein, J.-C.D., T. S. Luk, T. R. Nelson, A. McPherson, S. M. Cameron, Opt. Lett., 2003. **28**: p. 2354.

82. G. Mejean, J.K., E. Salmon, J. Yu, J.P. Wolf, R. Bourayou, R. Sauerbrey, M. Rodriguez, L. Woeste, H. Lehmann, B. Stecklum, U. Laux, J. Eisloeffel, A. Scholtz, A.P. Hatzes, Appl. Phys. B, 2003. **76**: p. 357.

83. J.-F. Ripoche, G.G., B. Prade, M. Franco, E. Nibbering, R. Lange, A. Mysyrowicz, Opt. Commun., 1997. **135**: p. 310.

84. N. Akozbek, A.I., A. Becker, M. Scalora, S. L. Chin, C. M. Bowden, Phys. Rev. Lett., 2002. **89**: p. 143901.

85. K. Iizuka, *Elements of Photonics*. Vol. I: In Free Space and Special Media. 2002: John Wiley & Sons.

86. R. W. Boyd, *Nonlinear Optics*. 2003, Academic press: San Diego. p. 210-213.

87. S. Varma, Y.-H.C., H. M. Milchberg, Phy. Rev. Lett., 2008. **101**: p. 205001.

88. A. Dubietis, G.T., G. Fibich, B. Ilan, Opt. Lett., 2004. **29**: p. 1126.

89. Q. Wu, X.-C.Z., Appl. Phys. Lett., 1995. **67**: p. 3523.

90. J. H. Booske, Phys. Plasmas, 2008. **15**: p. 055502.

91. P. H. Siegel, IEEE Trans. Microwave Theory Tech., 2002. **50**: p. 2644.

92. M. Bass, P.A.F., J. F. Ward, G. Weinreich, Phys. Rev. Lett., 1962. **9**: p. 446.

93. A. Nahata, A.S.W., T. F. Heinz, Appl. Phys. Lett., 1996. **69**: p. 2321.

94. Y. Zhang, Y.C., C. Marceau, W. Liu, Z.-D. Sun, S. Xu, F. Theberge, M. Chateauneuf, J. Dubois, S. L. Chin, Opt. Express, 2008. **16**: p. 15483.

95. Q. Wu, M.L., X.-C. Zhang, Appl. Phys. Lett., 1996. **68**: p. 2924.

96. J. Kasparian, J.-P.W., Opt. Express, 2008. **16**: p. 466.

97. D. J. Cook, R.M.H., Opt. Lett., 2000. **25**: p. 1210.

98. M. Kress, T.L.f., S. Eden, M. Thomson, H. G. Roskos, Opt. Lett., 2004. **29**: p. 1120.

99. T. Bartel, P.G., K. Reimann, M. Woerner, T. Elsaesser, Opt. Lett., 2005. **30**: p. 2805.

100. X. Xie, J.D., X.-C. Zhang, Phys. Rev. Lett., 2006. **96**: p. 075005.

101. K. Reimann, Rep. Prog. Phys., 2007. **70**: p. 1597.

102. K. Y. Kim, J.H.G., A. J. Taylor, G. Rodriguez, Opt. Express, 2007. **15**: p. 4577.

103. M. D. Thomson, M.K., T. Loffler, H. G. Roskos, Laser Photonics Rev., 2007. **1**: p. 349.

104. A. Houard, Y.L., B. Prade, A. Mysyrowicz, Opt. Lett., 2008. **33**: p. 1195.

105. K. Y. Kim, A.J.T., J. H. Glownia, G. Rodriguez, Nature Photonics, 2008. **2**: p. 605.

106. D. You, R.R.J., P. H. Bucksbaum, D. R. Dykaar, Opt. Lett., 1993. **18**: p. 290.

107. T. Loffler, T.H., M. D. Thomson, F. Jacob, H. G. Roskos, Opt. Express, 2005. **13**: p. 5353.

108. P. C. M. Planken, H.-K.N., H. J. Bakker, T. Wenckebach, J. Opt. Soc. Am. B, 2001. **18**: p. 313.

109. Y. Zhang, Y.C., S. Xu, H. Lian, M. Wang, W. Liu, S. L. Chin, G. Mu, Opt. Lett., 2009. **34**: p. 2841.

110. A. Houard, Y.L., A. Mysyrowicz, B. Leriche, Appl. Phys. Lett., 2007. **91**: p. 241105.

111. C. D'Amico, A.H., S. Akturk, Y. Liu, J. Le Bloas, M. Franco, B. Prade, A. Couairon, V. T. Tikhonchuk, A. Mysyrowicz, New J. Phys., 2008. **10:** p. 013015.

112. T. Loffler, F.J., H. G. Roskos, Appl. Phys. Lett., 2000. **77:** p. 453.

113. W.-F. Sun, Y.-S.Z., X.-K. Wang, Y. Zhang, Opt. Express, 2008. **16:** p. 16573.

114. Y. P. Deng, J.B.Z., Z. G. Ji, J. S. Liu, B. Shuai, R. X. Li, Z. Z. Xu, F. Th 閔 erge, S. L. Chin, Opt. Lett., 2006. **31:** p. 546.

115. F. Blanchard, L.R., H.-C. Bandulet, G. Sharma, R. Morandotti, J.-C. Kieffer, T. Ozaki, M. Reid, H. F. Tiedje, H. K. Haugen, F. A. Hegmann, Opt. Express, 2007. **15:** p. 13212.

116. Q. Wu, X.-C.Z., Appl. Phys. Lett., 1996. **68:** p. 1604.

117. http://www.tydex.ru/en/products/thz_optics/thz_materials/.

118. G. Gallot, J.Z., R. W. McGowan, T.-I Jeon, D. Grischkowsky, Appl. Phys. Lett., 1999. **74:** p. 3450.

119. O.G. Kosareva, W.L., N.A. Panov, J. Bernhardt, Z. Ji, M. Sharifi, R. Li, Z. Xu, J. Liu, Z. Wang, J. Ju, X. Lu, Y. Jiang, Y. Leng, X. Liang, V. P. Kandidov, S. L. Chin, Laser Physics, 2009. **19:** p. 1776.

120. A. Yariv, Q*uantum Electronics.* 2nd ed. 1975, New York: Wiley.

121. http://en.wikipedia.org/wiki/Lock-in_amplifier.

122. M*anual for MODEL SR830 DSP Lock-In Amplifier. M*anual.